

Fundamental aspects and recent progress on wear/scratch damage in polymer nanocomposites

Dasari, Aravind; Yu, Zhong-Zhen; Mai, Yiu-Wing

2008

Dasari, A., Yu, Z.-Z., & Mai, Y.-W. (2009). Fundamental aspects and recent progress on wear/scratch damage in polymer nanocomposites. Materials science and engineering R : reports, 63(2), 31-80.

<https://hdl.handle.net/10356/101609>

<https://doi.org/10.1016/j.mser.2008.10.001>

© 2008 Elsevier B.V. This is the author created version of a work that has been peer reviewed and accepted for publication by Materials Science and Engineering: R: Reports, Elsevier B.V.. It incorporates referee's comments but changes resulting from the publishing process, such as copyediting, structural formatting, may not be reflected in this document. The published version is available at:
[<http://dx.doi.org/10.1016/j.mser.2008.10.001>].

Downloaded on 25 Aug 2022 18:06:30 SGT

FUNDAMENTAL ASPECTS AND RECENT PROGRESS ON WEAR/SCRATCH DAMAGE IN POLYMER NANOCOMPOSITES

Aravind Dasari¹, Zhong-Zhen Yu², Yiu-Wing Mai¹

¹Centre for Advanced Materials Technology (CAMT)

School of Aerospace, Mechanical and Mechatronic Engineering (J07)

The University of Sydney, Sydney, NSW 2006, Australia

²Beijing Key Laboratory on Preparation and Processing of Novel Polymeric Materials

Department of Polymer Engineering, College of Materials Science and Engineering

Beijing University of Chemical Technology

Beijing 100029, China

Table of Contents

Abstract	4
1. Introduction	5
2. Wear Damage in Polymer Nanocomposites	10
2.1. Wear Mechanisms and Theories	12
2.1.1. Adhesive Wear	12
2.1.2. Abrasive Wear	13
2.1.3. Delamination Wear	14
2.1.4. Fatigue Wear	15
2.1.5. Transfer Wear	15
2.1.6. Other Forms of Wear Damage	16
2.2. Ti-based Compounds	18
2.3. Si-based Compounds	21
2.4. Zn-based Compounds	24
2.5. Carbon Nanotubes	26
2.6. Other Miscellaneous Fillers	29
2.7. Influence of Particle Surface Treatment on the Wear Behavior	33
2.7.1. Physical Treatment Methods	33
2.7.2. Chemical Treatment Methods	34
2.7.3. Some Examples Signifying the Influence of Surface Treatment	35
2.8. Parameters Controlling Wear Damage in Polymer Nanocomposites	38
3. Nano-Wear Damage in Polymeric Materials	40
4. Models for Different Wear Modes	44
5. Background - Nanoindentation Technique	51
5.1. Application of Nanoindentation Technique to Polymer Nanocomposites	54
6. Scratch Damage in Polymer Nanocomposites	57
6.1. Types of scratches and their characterization methods	58
6.2. Parameters effecting scratch resistance	61
6.2.1. Young's modulus	61
6.2.2. Yield and tensile strengths	63
6.2.3. Scratch hardness	63

6.3. Scratch morphology and damage mechanisms	64
7. Concluding Remarks and Future Recommendations	71
8. Acknowledgements	72
9. References	73

Tables

Figures

Abstract

It is realized that the addition of a small percentage of rigid nanoparticles to polymers significantly improves many of their mechanical properties, especially stiffness and strength. Such improvements are often attributed to the availability of large numbers of nanoparticles with huge interfacial areas compared to their macro- and micro-scale counterparts. In particular, from the tribological viewpoint, the small size of nanoparticles with homogenous dispersion in the matrix and good interfacial adhesion between nanoparticles and matrix are thought to be necessary requirements for a polymer nanocomposite. Material removal will be less since the nano-additives has similar sizes to the segments of surrounding polymer chains. Despite these positive effects due to the addition of nanoparticles, there are still some critical questions that are unanswered. Here, we review the fundamentals, recent progress and advances that have been made on the tribological aspects of polymer nanocomposites, particularly focusing on their wear (in dry sliding and unlubricated conditions) and scratch damage. The review shows that (a) it is not valid to assume that nano-fillers always improve wear/scratch (and friction) properties; and (b) material properties like modulus, hardness, fracture toughness or extent of wear rate or scratch penetration depth are not the sole indicators to compare and/or rank candidate materials. Several facets of wear/scratching or material response to the sliding processes require thorough understanding in order to determine parameters that control the surface integrity and material removal from polymer nanocomposites. This review also shows the apparent contradictions and false impressions on several material systems in many studies owing to poor characterizations of polymer nanocomposites and lack of quantitative descriptions of the observed phenomena.

Keywords: Wear; Scratch; Nanoindentation; Polymer Nanocomposites; Nanoparticles

1. Introduction

Tribology is the science that encompasses different aspects of machinery, surface engineering, friction, chemistry and lubrication between interacting surfaces in relative motion. The fundamental objective in most of these cases is to reduce material loss or damage to minimum or even zero. However, in some cases of precision engineering, it is required to have control on the extent of material removal. For example, the complex pattern shown in **Figure 1** was generated precisely using an atomic force microscope at a normal load of 15 μN and a writing (scratching) speed of 0.5 $\mu\text{m/s}$ [1]. The separation between the lines is about 50 nm. This pattern is useful for resistor trimming (to increase the path resistor) on a small scale. To achieve this type of precise patterns, it is necessary to have good control on parameters like normal load, scanning speed and tip geometry.

Most of the work on tribology to date, in particular, at the micro- and nano-scales is focused on metals and ceramics used for the nano-electronics industry and microelectro-mechanical systems (MEMS). Although polymers and polymer nanocomposites, owing to their adequate strength, lightness, versatility, ease of processing and low cost, have been widely employed to replace the traditional metals and ceramics in microelectronic packaging, coatings, aerospace, automotive, food packaging and biomedical applications, not much work is done on them in this regard. This may be due to their viscoelastic properties, which makes the processes and analysis much more complicated. Additionally, in the case of polymer nanocomposites, detailed knowledge of the role of nano-fillers during the tribological processes, and the precise relationships between structures, properties and processing are required. This article gives a comprehensive review on the fundamental aspects, recent progress and advances that have been made on the tribological response of polymer nanocomposites, especially focusing on their wear (in dry sliding and unlubricated conditions) and scratch damage.

The tribological properties of polymers are generally improved with the addition of reinforcing and/or lubricating fillers [2]. Examples of conventional lubricating fillers include graphite, poly(tetrafluoroethylene) (PTFE), molybdenum disulfide (MoS_2), and some synthetic oils; while common reinforcing fillers include glass fibers, carbon fibers, etc. The lubricating fillers function

mainly by decreasing the surface energy; but these fillers lead to a weak bond in the material, and affect the strength of the materials. On the contrary, reinforcing fillers increase the strength of polymeric materials but also increase the abrasiveness of the counterpart. This may increase the friction coefficient and counterface slider roughness, prevent the formation of a uniform protective transfer film on the slider, and lead to third body wear of the composite. Also, if they are polar, high surface energy and high shear strength increases the friction coefficient, which is undesirable. Some fillers promote the formation of a transfer film on the counterface slider [3, 4]; in some cases when conductive fillers are used, they facilitate the dissipation of frictional heat by improving the conductivity of the polymers [5].

The great interest and demand generated for these macro- and micro-composites in scientific, technological and structural applications in recent years have ultimately led to the limits of optimizing composite properties, because the properties achieved usually involve compromises [6-9]: e.g., stiffness and/or strength, important for scratch resistance (in terms of residual scratch depth), are achieved at the expense of toughness or loss of optical and rheological properties and vice-versa. To overcome these drawbacks from macro- and micro-scale reinforcements, nano-scale fillers were introduced - where the filler is less than 100 nm in at least one dimension. A wide range of morphologies can be expected for nanoparticles, such as spheres, flakes, platelets, dendritic structures, tubes, rods, coils, springs and brushes. In general, three major characteristics define and form the basis of performance of polymer nanocomposites:

(i) Nanoscopic confinement of matrix polymer chains: This characteristic feature of the nano-scale fillers is important to improve their interfacial interaction with the matrix polymer and to enhance their nucleation capability. That is, the nano-fillers restrict the mobility of the polymer chains in their vicinity and thereby influence the overall matrix rigidity (particularly with rigid fillers). An example of this phenomenon is shown in **Figure 2** for a polyamide 6/organoclay nanocomposite [10]. Crystalline lamellae are aligned perpendicular to the lateral interface (on both sides) of each clay layer and matrix, and appear closely organized to each other depending on the orientation of the clay layers. These preferentially organized layers are around 30-40 nm (on both sides) for each clay layer and it suggests that nucleation occurs at the silicate surface during crystallization of the polyamide matrix (which is also confirmed by differential scanning

calorimetry measurements). Thus, if the inter-particle distance is smaller, all the lamellae in the region are highly constrained, and consequently their plastic deformation capability is curtailed. Without a constraint releasing mechanism, the nanocomposite fails in a brittle manner with a low toughness. However, there are several studies which reported considerable improvements in the toughness of polymer nanocomposites via different mechanisms, such as increase of fracture surface area owing to crack deflections, initiation and development of a large number of micro-cracks (due to delamination in the case of layered fillers) [11-18], and mobility of the nano-fillers in a polymer during deformation [19-21]. In particular, the concept of ‘mobility’ was introduced recently based on the molecular dynamics simulations of Gersappe [19]. Experimental evidence of Shah et al. [20] on polymer/layered filler nanocomposites during tensile stretching above the glass transition temperature of the polymer also suggested that it is the mobility of nano-fillers that controls their ability to dissipate energy, which would increase the toughness of polymer nanocomposites. The ‘mobility’ concept was later applied to non-layered fillers like silica and it was shown that low particle-particle interaction, strong filler-matrix adhesion, and adequate polymer matrix mobility (usually achieved above the glass transition temperature) are required for this mechanism to occur [21]. However, it is necessary to distinguish whether it is the particle mobility *per se* or it is facilitated by the mobility of polymer chains during tensile testing; that is, during tensile deformation (especially above T_g), the polymer chains will stretch and align along the tensile direction causing the particles to rotate with the plastically deformed matrix. These results only show that the nano-fillers (unlike micron-sized fillers) are able to actively participate in the mechanical response of the matrix polymer under an applied stress field.

(ii) Nanoscale inorganic constituents and variation in properties from micro-scale fillers:

Distinct differences exist between nano- and micro-scale or bulk material properties. Many studies have reported that conductivity, optical, magnetic, and electronic properties of several inorganic nanoparticles significantly change as their size is reduced from macro-scale to micro- and nano-levels [22-24]. In some cases, it has been shown that nanoparticles are more active than their traditional counterparts since they have higher percentages of atoms on their surfaces [25]. Even biological activities (anti-microbial) were reported for some nanoparticles compared to their bulk materials or micro-scale particles [26]. Also, compared to bulk ferromagnetic materials where multiple magnetic domains exist, several small ferromagnetic particles consist of only a

single magnetic domain resulting in super-paramagnetism [27]. Further, mechanical property variations are detected in some cases, for example, carbon nanotubes are as stiff as graphite fibers, but are almost an order of magnitude stronger [6, 28].

(iii) Nanoparticle arrangement and creation of large polymer/particle interfacial area: The nano-level dispersion of fillers in the polymer matrix and huge polymer/particle interfacial areas provide an opportunity for fine tuning their surface properties, and hence a prospect for tailoring various required properties for different end applications. For example, clay platelets (made up of layers of two tetrahedrally coordinated silicon atoms fused to an edge-shared octahedral sheet of either aluminium or magnesium hydroxide) have a thickness ~ 0.94 nm and lateral dimensions from several hundreds of nanometers to microns depending on the particular layered silicate [29-33]. This provides a large surface area of ~ 750 m²/g of silicate material that can interact with the matrix. Also, the ability to fine-tune their surface chemistry through ion exchange reactions with organic and inorganic cations leads to many possibilities, more than merely dispersing the clay layers in a polymer matrix. Typical examples include chemically attaching a small amount of bromine on the ammonium cation of clay layers or modifying the clay layers by phosphonium to improve the fire performance of polymer/clay nanocomposites [34, 35].

Full exploitation of the above fundamental characteristics of nano-reinforcements in polymers facilitates the achievement of enhanced multi-functional properties in polymer nanocomposites, which are not displayed by their macro- and micro-composite counterparts.

From the tribological viewpoint, major benefits of polymer nanocomposites relative to micro-sized particle composites are: (i) material removal is expected to be less as the nano-fillers have similar size to the segments of the surrounding polymer chains; and (ii) bonding between nano-filler and matrix is expected to be better due to their large specific surface areas [25, 36-39]. In addition to directly influencing the tribological performance of the composites, nano-additives affect indirectly by changing the crystallinity, microstructure, glass transition and degradation temperatures, and other physical/mechanical properties of the polymer matrix [40]. Due to their high reactivity, it is also expected that nanoparticles influence the transfer film more proactively than the micro-particles [41].

Besides, accurate interpretation of the origin and development of complex tribological processes in polymer nanocomposites requires precise understanding and measurement of the surface and subsurface phenomena at different levels. Characterization techniques are generally categorized depending on the use of real or reciprocal space data as direct and reciprocal space methods [42]. Visualization of the atomic-scale phenomena is possible using direct space methods; while the interference and diffraction effects of the lattice planes, electrons or photons are examined with reciprocal space methods for structural characterization. Although reciprocal methods provide a means of characterization, direct imaging is only possible using direct space methods. The use of either class of methods alone cannot fully identify the damage processes or any other structural characterization required and can lead to false conclusions. For example, in a recent study, we indicated that x-ray diffraction is not a reliable tool for analyzing the complex dispersion of clay layers in ternary nanocomposites, particularly polymer/rubber/clay systems, as no characteristic basal diffraction peak of clay is found in the 2θ range 1° - 10° for all the nanocomposites, pointing to the complete exfoliation of clay [43]. However, transmission electron microscopy (TEM) results are completely different and do not support the XRD results.

Thus, a combination of space and reciprocal methods is required for accurate identification of the tribological processes and/or other structural features. Several analytical tools with high vertical, spatial and time resolutions have been used for these purposes and they include high resolution transmission electron microscopy (HR-TEM), scanning probe microscopy (SPM), field ion microscopy (FIM), x-ray absorption near-edge spectroscopy (XANES), time-of-flight secondary ion mass spectroscopy (ToF-SIMS), x-ray photoelectron spectroscopy (XPS), and Auger electron spectroscopy (AES). An illustration of the resolution of these surface analytical tools is given in **Figure 3** as viewed from time, size, and resolving power [42]. Whilst these powerful tools have increased the understanding of tribological processes in different materials, combination of all resolutions is limited in any particular tool. For example, Fourier transform infrared spectroscopy (FTIR) and Raman spectroscopy if operated at time resolutions of nano- and pico-seconds, the spatial resolution has to be compromised in these cases. Therefore, the time-axis in Figure 3 is in fact more complicated and hard to portray. Additionally, real time and *in-situ* analysis of the contact zone during a tribological process is still practically difficult with commercially available techniques.

2. Wear Damage in Polymer Nanocomposites

Wear generally originates from damage induced by rubbing bodies due to repeated applications of mechanical, impact and other kinds of forces [44-48]. Therefore, the surface loses mechanical cohesion and debris is formed that is dislodged from the contact zone. Many wear mechanisms have been proposed [3-5, 41, 45, 47-65], e.g., abrasive, adhesive, fatigue, corrosive, erosive and delamination, which show the complexity of the wear phenomena. Wear debris can also be generated by material transfer from one surface to another (i.e., transfer wear, see below). Wear of polymers is affected by many intrinsic and extrinsic factors, such as surface roughness, contact kinematics, material nature, mechanical, physical and chemical properties of interacting bodies, testing environment, etc [2-5, 25, 36-41, 44-66]. In general, depending on the molecular and internal structural organizations, polymers have lower multiple transition temperatures and thermal conductivity than metals. Hence, the energy consumed in the processes of friction and wear can lead to softening, melting, oxidation or pyrolysis on the surface of the polymer and its relevant wear debris significantly affects the wear and friction performance [67]. It is necessary to understand the interaction between two mating surfaces so as to demonstrate completely the tribological performance.

Blau [68] distinguished three different interaction levels between the rubbing surfaces depending on the accommodation of the friction-induced shear. If it was located at the interface between the bounding solid surfaces, as it would in an effectively-lubricated system, it was considered to be a *level 1* interaction. The behavior of molecular layers and interfacial films dictate the appropriate feature scale (sub-nanometers to tens of nanometers). At *level 2*, if shear was transmitted to the solids bounding the relatively-moving interface, then the properties of these solids, particularly those in the near-surface zone affected by shear requires consideration (several microns). The properties of the environment and its interactions with the mating elements should also be included. Finally, if the mating elements cannot fully accommodate frictionally imposed shear by plastic yielding so that forces will be transferred to the fixtures, then the characteristics of the constraining machine and fixtures must be included, which was considered to be *level 3*. In this case, the dimensions considered may be several orders of magnitude larger (from micrometers to centimeters) than those required for *level 2*.

Holmberg et al. [69] also classified the tribological contact mechanisms based on the interaction levels. As a function of time, the tribological processes produce changes in both geometry and material composition at the contact surface and result in energy related output effects: friction, wear, velocity, temperature, sound and dynamic behavior. **Figure 4** shows schematically the tribological contact mechanisms yielding macromechanical changes, material transfer, micro-mechanical, tribochemical and nano-physical changes occurring at the contact [69].

These observations and studies clearly suggest that for accurate prediction and understanding of the mechanisms of wear or scratch processes, it is necessary to have a thorough knowledge of the different complex interactions and/or other phenomena taking place at different levels/scales by using a combination of space and reciprocal techniques, taking into account the properties of the interacting bodies.

Besides, particularly for polymers, different wear mechanisms can be grouped mainly into two categories: cohesive and interfacial wear processes (schematically shown in **Figure 5**) [45]. In the cohesive wear processes, the frictional work is dissipated in relatively large volumes adjacent to the interface either through the interaction of surface forces and the resultant traction stresses or simply via geometric interlocking of interpenetrating contacts. The extent of this surface zone is defined by the contact geometry and contact stresses generated in the surface. Cohesive wear processes are mainly controlled by mechanical properties of the interacting bodies. Most of the mechanical wear processes can be grouped under this category, such as abrasive, fatigue and fretting. In contrast, the interfacial wear processes involve dissipation of frictional work in much thinner regions and at greater energy densities. This creates a large increase in local temperature. The chemistry of surfaces and forces emanating from them should also be considered, other than the mechanical properties of the interacting materials, to determine the extent of wear damage. Transfer wear and chemical or corrosive wear belong to interfacial wear processes.

Before discussing different aspects of wear damage in polymer nanocomposites, it would be appropriate to briefly review the different material removal mechanisms and theories.

2.1. Wear mechanisms and theories

2.1.1. Adhesive wear

Adhesive wear arises from the fracture of adhesively bonded junctions occurring because of the relative motion between mating surfaces; while formation and rupture of the junctions control the adhesion component of friction. When two surfaces slide against each other, the actual contact is between asperities of the two surfaces. Junctions are formed at these contact regions due to welding (in the case of metals), physical or chemical interactions (in case of polymers and may include van der Waals and hydrogen bonds) possibly due to heating at the interface which may be high enough to cause melting or softening of the sliding polymer surface [70]. On further sliding, if the bonding at the interface of the adhering asperities is greater than the strength of the asperities, fragments detach from the surface resulting in adhesive wear. This may also produce a film or lumps of polymer on the slider contact surface and so their adhesion to the slider and the role in influencing the friction and wear properties are important [71]. Shearing of the junctions under the applied tangential force also results in the frictional force. In general, the formation, growth and fracture of the junctions are controlled by the nature of surfaces, surface chemistry and stresses in the surface layers. An example showing adhesive wear in polypropylene with minor amounts (1.5 phr) of stearic acid when slid against a silicon nitride steel ball is given in **Figure 6a** [72].

The adhesion wear theory proposed by Archard (by modifying the semi-empirical Holm's theory [73] where it was assumed that the removal of materials to be atoms and not clusters of atoms corresponding to the surface asperities) has been widely accepted and used since the relationship (equation 1) between wear volume, normal load and hardness was consistent with experimentally observed results [74]. That is,

$$V = \frac{kNL}{H} \quad (1)$$

where V is wear volume loss (mm^3); k wear coefficient ($\text{mm}^3/\text{N.m}$); N normal load (Newtons); L sliding distance (meters); and H hardness of the wearing material.

Though conceptually simple, there are some important factors in the adhesion wear theory which need further deliberation, e.g., nature of atomic forces at the interface, interface deformation during sliding, final junction rupture under shear, etc. Whilst some of these factors have been addressed [64], such as the thermodynamic or wetting theory, which explains the adhesion via best wetting of a solid surface by a molten polymer, the chemical theory, which accounts for the formation of chemical bonds at the interface, and the weak cohesion boundary layer theory, which explains rupture of the intermediate layer between two solids, yet further understanding is required on different materials and at different length scales.

2.1.2. Abrasion wear

This is the most common type of wear, particularly in polymer composites. It can be again subdivided into two processes: two-body abrasion wear and three-body abrasion wear. Two-body abrasion occurs when hard asperities plow and cause plastic deformation or fracture of the softer ones; while three-body abrasion is known to take place when hard abrasive particles or wear debris are introduced into the sliding system either as environmental contaminants or as products of two-body abrasion. Wear debris formation in abrasive wear generally occurs by plowing, cutting and cracking mechanisms induced by the hard asperities of the counterface slider. **Figure 6b** shows a typical example of abrasive wear experienced by polyamide 6/clay (95/5) composite when slid against a silicon nitride ball [75]. In general, abrasive wear varies directly with the hardness of the materials in contact, the geometry of the abrasive particles, the load and the sliding distance. A number of expressions have been proposed for abrasive wear of polymers. For example, Rabinowicz [76] gave a simple quantitative expression for abrasive wear loss by assuming the hard asperities to be conical. That is,

$$V = \frac{NL \overline{\tan \theta}}{\pi H} \quad (2)$$

where θ is the cone angle, $\overline{\tan \theta}$ weighted average of $\tan \theta$ values and H hardness of the softer material. By considering the three stages in forming a wear particle (i.e., deformation of surfaces to an area of contact determined by the indentation hardness, relative motion between the mating surfaces opposed by the frictional force ($F = \mu N$), and disruption of material at the contact regions involving an amount of work given by the integral of the stress-strain curve in a tensile test and

taken as the product of the fracture stress and the strain to break), Ratner et al. [77] showed that the abrasive wear volume V is given by:

$$V = \frac{c\mu N}{H\varepsilon\sigma} \quad (3)$$

where μ is coefficient of friction, H indentation hardness, σ tensile strength, ε strain to break and c a proportionality constant.

Note that these equations apply generally to polymers without fillers. For polymer composites, many studies have shown that there are no fixed correlations of wear with mechanical properties. It is found that the extent of counterface modification or damage plays an equally important role. For elastomers and rubbers, abrasion wear is complex [78]. This is because the elastomers are heated by frictional energy, softened and adhered to the abrading surface. They then stretch and form abrasion ridges oriented normal to the sliding direction. An example is shown in **Figure 6c**. Debris is seen as rolled-up particles from these ridges.

2.1.3. Delamination wear

The delamination theory was first introduced in 1973 [61-63] and the processes involved in the generation of wear debris are briefly described here. When two surfaces are brought together, contact is established only at the asperities. As the contact area is small, local plastic deformation occurs under these asperities. When a tangential displacement is imposed on the asperities, a friction force follows. This combination of normal and tangential tractions results in a zone of compressive stresses below and ahead of the asperities and a zone of tensile stresses behind the asperities. Thus, the material near the surface will experience a cyclic state of loading each time an asperity passes by. Asperities of the softer surface are easily deformed and some are fractured by repeated loading. A relatively smooth surface is finally generated, either when these asperities are deformed or removed. Once the surface becomes smooth, the contact is not just asperity-to-asperity, but rather asperity-to-plane. Hence, each point along the softer surface is subjected to cyclic stresses as the asperities of the harder surface plow it. The surface traction exerted by the harder asperities on the softer surface induces plastic shear deformation that accumulates with repeated loading. Intense plastic deformation at the deformed layer nucleates voids around the inclusions. The subsurface voids elongate due to further cyclic loading and they coalesce to form

longer cracks fairly parallel to the sliding direction. When these cracks finally shear to the surface, long and thin wear sheets “delaminate” producing flake-like wear debris. A schematic of the various stages involved in the formation of delamination wear sheets is shown in **Figure 6d**. The thickness of a wear sheet is controlled by the location of subsurface crack growth, which is controlled by the normal and the tangential loads at the surface. Additionally, compared to the adhesive theory, the delamination theory predicts that microstructure affects the wear behavior and demonstrates that hardness is not the only controlling factor.

Although delamination wear is mostly observed in metals and ceramics, it has also been reported by many investigators in polymers and polymer composites [39, 57, 79-82]. In particular, this mode of wear damage is noted in the ultra-high molecular weight polyethylene (UHMWPE) components of artificial knee and hip joints due to the cyclic (frictional) loading and in simulated laboratory wear tests [79-81]. The intense plastic deformation of the polyethylene surface under cyclic loading is found to be the origin of crack nucleation and propagation. Besides UHMWPE, delamination wear is also seen in epoxy resin [39] and polytetrafluoroethylene (PTFE) [57].

2.1.4. Fatigue wear

In brief, this mode of wear damage is a result of surface fatigue, which is repeated stressing and un-stressing of the contacts eventually leading to their fatigue fracture. Its characteristic feature is accumulation of irreversible changes, which give rise to the generation and development of cracks. An example of fatigue wear in epoxy resin when slid against a silicon nitride ball is given in **Figure 6e** [72]. Fatigue wear also occurs in combination with delamination wear where subsurface cracks nucleate and coalesce due to shear deformation of the softer surface induced by traction of the harder asperities. This results in the detachment of fragments in larger sizes.

2.1.5. Transfer wear

Transfer films can form in polymer-metal, polymer-ceramic and polymer-polymer sliding contacts and are responsible for the gradual transition from transient wear to steady-state wear. While in a polymer-metal or polymer-ceramic system, transfer invariably occurs from polymer to metal or ceramic, the direction of transfer in polymer-polymer systems is not that obvious. The transfer of material occurs because of adhesion between the two materials, which during

sliding contributes to shear in the subsurface region of the contact [45]. Rhee and Ludema [83] demonstrated that the transfer film could exist in a solid state and also in a liquid state depending on the interfacial temperature. Different mechanisms for adhesion have been proposed and they include Coulomb electrostatic forces, van der Waals forces, and bonding from chemical reactions that can occur during the wear process between slider and polymer. In addition, many parameters are shown to influence the formation of transfer film and its role on subsequent wear processes: thickness and stability of transfer film, cohesion between the transfer layers, adhesion strength between transfer film and counterface slider, sliding conditions such as velocity, normal load, atmosphere, and temperature, polymer structure in terms of backbone flexibility, side chains, pendant groups, and crystallinity, surface roughness and chemical reactivity of the counterface, and presence of fillers. These factors and the interaction amongst themselves clearly indicate the complexity in understanding the role of the transfer film in affecting wear volume losses. More information and examples on transfer wear are given in **Section 3.2**.

2.1.6. Other forms of wear damage

Other forms of less common modes of material removal in polymers include chemical, fretting, erosion, corrosion, etc. Chemical wear occurs if a reaction takes place between mating surfaces or a material in itself or a material with surrounding environment. Examples include oxidation of polymers, hydrolysis of polymers and dissolution. These reactions may lead to chain scission and molecular weight degradation of the polymers [84]. Fretting is a form of wear which occurs between two contacting surfaces having relative oscillatory motion of small amplitude [85]. The wear debris produced, if it cannot escape from between the surfaces, may result in an increase in pressure and eventually leads to seizure. If the debris can escape, it results in loss of fit between the surfaces and a reduction in clamping pressure may lead to greater vibration. Erosion is caused by a gas or a liquid, which may or may not carry entrained solid particles, impinging on a surface. When the angle of impingement is small, the wear produced is closely analogous to abrasion. But when the impingement angle is normal to the surface, material is displaced by plastic flow or is dislodged by brittle failure [86, 87].

A compilation of the different wear mechanisms leading to material loss is shown in **Figure 7** (adapted from [59]). Besides, there is always an overlap of wear mechanisms in any particular wear process and the combination of different mechanisms may represent the actual phenomena.

Compared to the different forms of wear damage in polymeric materials at macro- and micro-levels discussed above, at the nano-level where the applied loads are very low (ranging from μN and down to nN), the response is expected to be very different, as there may not be significant amount of wear particle generation, and the original surface topography is more likely to remain intact for an extended period due to the low wear rate. Additionally, the friction forces are also different as the plowing factor and the inertial effect of the moving components are different, and surface forces such as adhesion and electrostatic forces are likely to play an important role [88]. Nano-wear studies using a scanning probe microscope on neat polymers have shown a pattern of alternating ridges and troughs perpendicular to the direction of the motion of the tip at the low applied loads (in the range of 6-100 nN) irrespective of the polymer system suggesting that the formation mechanism is entirely dependent on the scan parameters and relatively independent on the polymer surface morphology. It was proposed that the ridge-formation type of deformation occurs via molecular displacement and conformational changes rather than bond breakage, that is, the primary deformation processes during nano-wear involve plastic deformation and viscous yielding; while extensive breaking of C-C bonds and the movement of material from the wear region do not occur [89]. More discussions on nano-wear damage are given later.

In the following sections, we will review recent progress made in understanding wear damage in several polymer systems filled with different nanoparticles. So the section is sub-divided based on the type of fillers. Before this, it is important to mention that many studies (discussed below) claim and believe that they are dealing with polymer nanocomposites based on the original (commercially obtained) nanoparticle sizes. However, in most cases, the nanostructures are not characterized (or not shown). This has led to confusions and difficulties when comparing with or correlating to similar studies since most nanoparticles tend to agglomerate after compounding with the polymers, and in some cases, they even result in microcomposites.

2.2. Ti-based compounds

The ability of dense nano-phase TiO_2 to deform extensively at elevated temperature without cracking or fracture [90] has sparked the possibility of using TiO_2 nanoparticles in polymers. Strain-rate sensitivity values obtained by Mayo et al. [91] also indicated ductile behavior of nano-phase ceramics at room temperature. Hahn et al. [92] have reported 60% ductility in 99% dense TiO_2 at 600 °C under far-field compression loading. A similar effect has been reported by Jain and Christman [93] in a mechanically attrited nano-phase intermetallic compound. So, these nanoparticles are extensively used to reinforce and thereby improve mechanical properties of different polymers such as epoxy, poly(phthalazine ether sulfone ketone) copolymer (PPESK), polyphenylene sulfide (PPS), and so on. For example, Ng et al. [94] dispersed TiO_2 nanoparticles (average diameter ~32 nm) in epoxy and showed that at some levels of loading, the resulting nanocomposites are more ductile than the traditional micro- TiO_2 particles (average diameter ~0.24 μm) filled epoxy. Wetzel et al. [95] incorporated a combination of micro- and nano-sized particles in epoxy. The specific wear rate decreased significantly with only 4 vol % of TiO_2 nanoparticles (**Figure 8**). By adding calcium silicate micro-particles (up to 12 vol %) in the nanocomposite matrix (at 4 vol % TiO_2), the specific wear rate is further reduced.

Chang et al. [96] studied the wear performance of polyetheretherketone (PEEK) and polyetherimide (PEI) reinforced with short carbon fibres, graphite flakes, and sub-micron sized particles of TiO_2 and ZnS. The frictional coefficient and wear rate of the composites were reduced in the presence of these fillers in both polymers. Gebhard et al. [97] also revealed that polyamide 46 containing the same micro- and nano-scale fillers (short carbon fiber, graphite flakes, TiO_2 and ZnS) have better tribological properties in terms of wear rate and friction compared to the neat polyamide 46. Although integration of various functional fillers proved beneficial from the viewpoint of tribological properties, it is difficult to relate any improvements or deteriorations in the final properties of the composites to the presence of any specific filler or its size or indeed a combination of different effects. Hence, the fundamental knowledge resulting from these studies is limited and requires thorough understanding of the individual roles of the fillers on different mechanical properties of the polymer to design improved wear-resistant polymer composites.

Shao et al. [98] compared the sliding wear properties of PPESK copolymer, a high performance polymer with an equivalent molar ratio of sulfone to ketone reinforced with micro- ($\sim 75\ \mu\text{m}$) and nano- ($\sim 40\ \text{nm}$) TiO_2 particles against a mild steel ring (sliding velocity $0.43\ \text{m/s}$, load $200\ \text{N}$, duration $1.5\ \text{h}$). The frictional coefficient was decreased rapidly when nano- TiO_2 particles were added up to $1\ \text{vol}\ \%$ and further increase of TiO_2 volume fraction resulted in an increase of the friction coefficient (**Figure 9a**); the authors attributed this to the dispersion quality of the filler though they did not show the dispersion of nano- TiO_2 filler at any composition. On the contrary, the friction coefficient of micro- TiO_2 particle-filled PPESK composite was less sensitive to the filler volume fraction and is higher than that of unfilled PPESK (**Figure 9a**). In contrast to the friction coefficient, the wear rate of nano- TiO_2 /PPESK composites decreased greatly up to $1\ \text{vol}\ \%$, and thereafter the reduction in wear rate was very small (**Figure 9b**); in micro- TiO_2 filled composites, wear rates increased with increasing filler volume fractions under identical test conditions and were higher by a factor of 1.5 to 3 than that of unfilled PPESK. In addition, the authors mentioned that at $1\ \text{vol}\ \%$ filler, there was a continuous, uniform and thin transfer film which was well bonded to the contact surface of the steel ring for the nano- TiO_2 filled PPESK composites. But no film was found in micro- TiO_2 filled PPESK due to heavy abrasive wear, and there was a coarse film when slid against unfilled PPESK.

By examining the FTIR spectra of the composites and wear debris, the authors explained these results by the different bonding strength between the polymer and nanoparticles/micro-particles. In both unfilled PPESK and nano- TiO_2 /PPESK composites, by comparing their respective wear debris, the spectra showed that after wear testing, the C–O–C peak ($1240\ \text{cm}^{-1}$) became strong and the Ar–C=O ($1666\ \text{cm}^{-1}$) peak became weak, suggesting that the double bond in Ar–C=O was active and could easily react with Fe (steel ring) (**Figure 9c**). However, this being the case, the quality of the transfer films formed on the steel surfaces in contact with unfilled and nano- TiO_2 filled PPESK, differences in wear rates, and the uniform transfer of material only at $1\ \text{vol}\ \%$ of nano- TiO_2 are still questionable.

Similar conclusion was also obtained by other investigators that nano- TiO_2 was more effective in reducing the wear rate of different polymers than micro- TiO_2 [99-101]. Though it was claimed that uniform dispersion of TiO_2 is required to improve the friction and wear behavior of polymer

nanocomposites (i.e., microstructural homogeneity) under dry sliding environment, the exact mechanisms of improvement in wear resistance are not clear. Shi et al. [102], based on the wear volume losses, suggested that addition of TiO_2 whiskers are better than TiO_2 particles in PTFE despite the significant wear reduction in both composites when compared to neat PTFE. These differences were attributed to variations in the quality of the transfer films formed on the slider in neat PTFE and filled materials. As shown in **Figure 10**, unlike the transfer film of pure PTFE, the transfer films of PTFE composites are smooth and coherent. The differences in wear volume losses between whiskers- and particles-filled PTFE composites were attributed to the preferential load support of whiskers in line with the concept proposed by Lancaster [103, 104] for the wear reducing action of fibers (compared to other particles) added in the polymer, and theoretically explained by Tanaka and Kawakami [105]. However, it should be noted that in [103-105] the wear rate was only reduced when the fibers were oriented normal to the sliding direction, since it was believed that it would be relatively easy for the resin between them to be preferentially worn away if they were parallel to the direction of sliding, thus removing the support from the fibers. But in [102], it was not given if the TiO_2 whiskers were preferentially oriented in the matrix.

In another study, the effect of different fillers including TiO_2 on the wear behavior of PPS was investigated [41]. The original particles sizes of all fillers (TiO_2 , CuO , and ZnO) varied from 30 to 50 nm. Sliding wear tests were conducted on pin-on-disk machine where the counterface steel disk rotated at 1 m/s to a distance of 40 km and the polymer pin was loaded with 19.6 N. In all the materials, the transfer films were observed on the counterface steel disks; however, with CuO and TiO_2 as fillers, the transfer films were claimed to be thinner, more uniform and continuous than ZnO ; but in neat PPS, it was thick and grainy, though the coverage was good. XPS analysis of the transfer film indicated reduction of TiO_2 and CuO fillers to elemental Ti and Cu while reacting with Fe of the steel to produce Fe_2O_3 . These nascent Cu or Ti elements have greater attraction towards the steel surface because they are highly reactive. Since these elements were locked in the transfer film, they in turn provided bonding of the transfer film to the counterface in addition to mechanical bonding (interlocking). This was not the case with ZnO where no elemental Zn was detected. The identified compositions along with their binding energies in the XPS spectra of the transfer film of PPS filled with 2 vol % of different fillers are listed in **Table 1**. As the binding energies of Cu and Cu_2O are close to each other (listed as 929.8 eV in the XPS

handbook), it is difficult to identify elemental Cu apart from Cu in Cu₂O in the Cu (2p) spectrum (Table 1). However, since Fe₂O₃ was identified, the authors suggested that the reaction between the counterface Fe and the filler CuO in the composite occurred leading to the generation of elemental Cu. Because the wear tests were conducted at ambient under high contact temperatures and pressures, oxidation of Fe in the presence of environmental water vapor would be possible, which made this argument questionable. Nevertheless, these observations were directly reflected in the wear resistance of PPS composites where the wear rates of PPS decreased when TiO₂ and CuO were used but increased with ZnO. The wear rates (mm³/km) of PPS, PPS/TiO₂, PPS/CuO, and PPS/ZnO were 0.324, 0.162, 0.078, and 1.089, respectively, at 2 vol % filler. It is noted that an earlier study by Kong et al. [106] showed the effect of surface oxide layers on wear behavior: FeO and Fe₃O₄ layers cause a significant reduction in wear, but Fe₂O₃ layers promotes wear. This conclusion contradicts the abovementioned observations of Bahadur and Sunkara [41] where the additional presence of Fe₂O₃ was shown to have no effect or reducing effect on the wear volume. It was also reported that with increase in TiO₂ content to 5 vol %, the transfer film became thick and lumpy, did not cover the counterface completely (**Figure 11**), and thereby yielded a higher wear rate ~0.726 mm³/km. Because the XPS results for PPS/TiO₂ composites with 5 vol % of TiO₂ are not shown, it is difficult to make specific conclusions that can support the XPS results shown in Table 1 at lower volume percentage (2 vol %) of TiO₂.

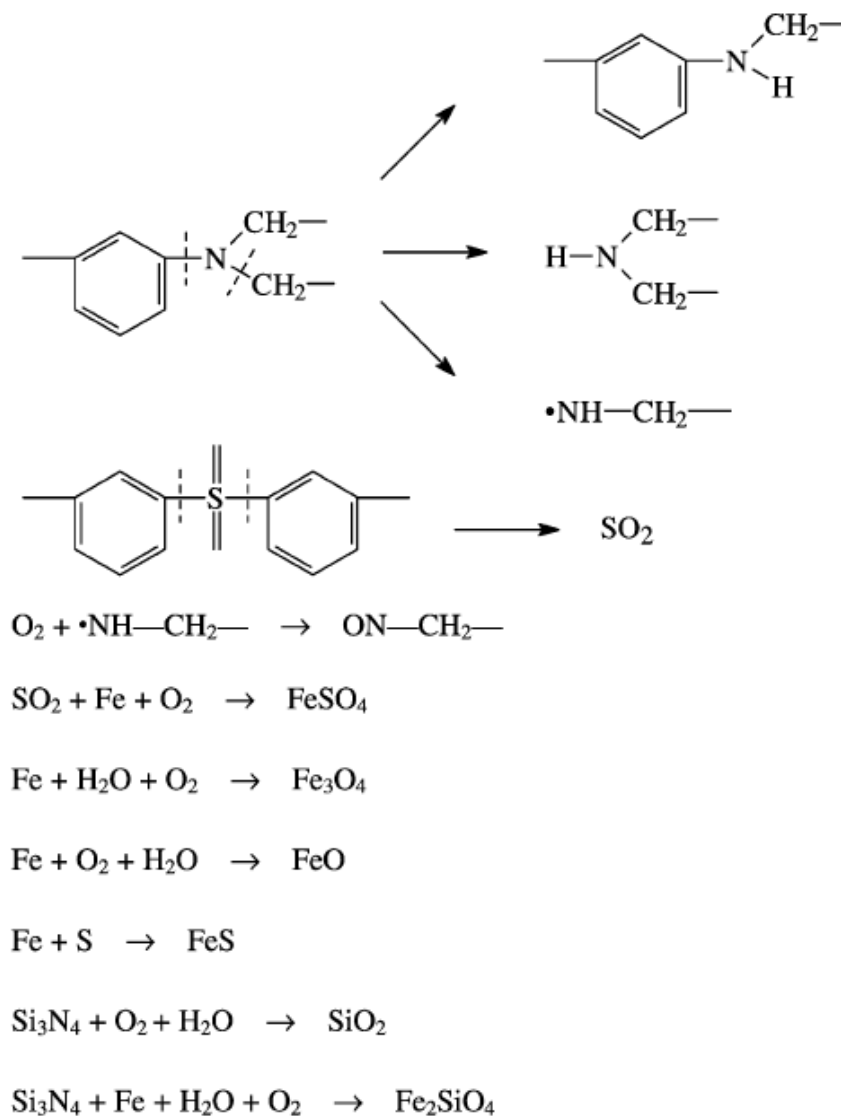
2.3. Si-based compounds

It is well known that bulk Si₃N₄ exhibits excellent capabilities of friction reduction and wear resistance against iron because of the hydrodynamic lubrication effect obtained by tribochemical wear. To obtain more beneficial effects of Si₃N₄, it has been used in many studies in the form of nano-sized particles in both thermoplastic and thermosetting polymers [107-112]. Shi et al. [107] investigated the sliding wear performance of nano-Si₃N₄/epoxy composites with different filler loading up to 2.9 vol %. Both friction coefficient and specific wear rate of unfilled epoxy were quite high when slid against a steel disk for 3 h at a sliding velocity 0.4 m/s and pressure 3 MPa. When nano-Si₃N₄ was incorporated, significant reductions in both these values were observed under identical conditions of testing even with filler content as low as 0.27 vol %. XPS analysis showed the formation of SiO₂ in the tribo-film which protected the specimen by its ability to

reduce friction. Reactions between Fe atoms of steel counterface and S atoms of epoxy caused oxidation of Fe under high contact temperature and pressure in environmental water vapor thus forming FeO and Fe₃O₄. Hence, the reductions in friction and wear volume of epoxy were partly attributed to formation of a transfer film on the steel disk consisting of SiO₂ (oxidative product of Si₃N₄), FeO and Fe₃O₄ (Fe-oxidative products). As shown in **Figure 12**, significant differences exist in the extent of wear damage; fatigue wear damage is predominant in neat epoxy, while the worn nanocomposite surface is smooth with minimum damage. The tribochemical reactions of epoxy and Si₃N₄ nanocomposites and those between the materials and counterface Fe are given in **Scheme 1**. However, it is noted that at higher contents of nano-Si₃N₄, after 1 vol %, wear rate is increased, though smaller than the neat material. This result is caused by the agglomeration of particles at higher volume fractions leading to a number of loosened clusters of particles in the tribo-system, which can be easily removed during sliding wear conditions.

Wang et al. [108, 109] observed that PEEK composites containing nano-Si₃N₄ and nano-SiO₂ particles exhibited the highest wear resistance, an improvement of about 85% in comparison to neat PEEK. Xue and Wang [112] also showed that nano-SiC was quite effective in reducing the wear rate of PEEK. When PTFE powder and nano-SiC particles were jointly incorporated into PEEK [111], the friction reduction and wear resistance capacities of the nanocomposites became worse. This was due to the chemical reaction between nano-SiC particles and PTFE during the sliding process yielding SiF_x. This deteriorated the formation of the transfer film on the slider contact surface and ultimately resulted in poor tribological properties compared to binary PEEK/SiC or PEEK/PTFE composites and neat PEEK. Also, when nano-SiC was added to PPS, the specific wear rates were higher than neat PPS; this was caused by the non-uniform transfer film on the slider (steel disk) contact surface [41]. Wang et al. [113] showed that under water lubrication, nano-SiC could greatly increase the wear resistance of PEEK. Yan et al. [114] studied the wear performance of nanocomposites of bismaleimide (BMI) with different contents of nano-SiC against a carbon steel ring. It was found that with only 6 wt % nano-SiC, reduction in specific wear loss occurred. Although the authors attributed this reduction partially to the formation of a relatively uniform transfer film on the counterface carbon steel contact surface in the presence of SiC compared to neat BMI, this cannot explain why the wear rate was higher at 8 wt % SiC. Also, hardness of the materials was considered to govern the wear performance and as

expected the hardness increased with SiC percentage. Although this increased the load-bearing capacity of BMI nanocomposites, it did not explain the reduced wear performance of BMI with 8 wt % SiC.



Scheme 1. Tribochemical reactions occurring at the interface between epoxy/Si₃N₄ nanocomposite and steel counterface during wear testing for 3 h at sliding velocity 0.4 m/s and normal pressure 3 MPa (from [107]).

Schadler et al. [110] produced silica/polyamide nanocomposite coatings using high-speed oxy-fuel thermal spray processing and found that the surface chemistry of the nano-silica affected the

final coating properties. Silica particles with a hydrophobic (methylated) surface resulted in higher scratch resistance than those with a hydrophilic (hydroxylated) surface. Though the exact mechanisms were unclear, a possible explanation was provided for this behavior based on the surface chemistry. Hydroxyl groups (OH) of hydrophilic silica will have polar interactions with amide (NH₂) groups in polyamide, while methyl groups of hydrophobic silica display van der Waals interactions with the hydrocarbon linkages of matrix chains. As the number of CH₂ groups are abundant (ten in every repeating unit) in the polyamide chain than the amide group (only one in every repeating unit), the authors suggested that this resulted in a stronger particle/matrix interactions yielding better scratch performance. However, it should be noted that the hydrogen bonding between polar molecules is 4-6 times stronger than van der Waals interactions and, in any case, stronger interactions between nanoparticles and matrix do not always yield higher scratch/wear resistance (see below).

To sum up the above investigations, it is clear that though an understanding of the tribochemical processes occurring between the counterface sliders and polymer surfaces are revealed by XPS and FTIR, many critical questions about the precise roles of nano-fillers remain unanswered. For this purpose, thorough identification of the surface and subsurface wear damage mechanisms is required. Consequently, it is necessary to combine chemical analyses tools with high resolution microscopy techniques.

2.4. Zn-based compounds

Friction and wear characteristics of PTFE filled with nano-ZnO were studied by Li et al. [115]. It was shown that the friction coefficient of nanometer ZnO/PTFE composites did not change very much from pure PTFE even with increase in filler content, but the wear volume was significantly decreased (**Table 2**). Though the reason for this behavior was attributed to the small size and non-aggregative behavior of the fillers, the size distribution and microstructures of the composites were not given, making it impossible to obtain any relationships. However, fibrous structures that existed in neat PTFE disappear due to the nanometer ZnO fillers which impede the drawing and destruction of PTFE fibrous structures during the wear process. Bahadur and Kapoor [116] studied the wear behavior of nylon 11 filled with different additives like ZnS, PbS and ZnF₂

against a steel disk at a constant sliding speed of 1 m/s, track diameter 65 mm, and a normal load 19.6 N under ambient conditions for 8 h. The specific wear rates were controlled by the tribochemical wear. Among the three fillers, only PbS was effective in reducing the wear of nylon. XPS analysis of the transfer film in nylon 11/PbS composite reveals that PbS dissociates (as Pb(4f) spectrum, **Figure 13**, peak at 138.5 eV, shows the presence of Pb₃O₄ in the transfer film), presumably as a result of the interfacial temperature rise, hence isolating the metal and sulfide ions in the transfer film. The sulfide ions reacted with the free radicals in the contact zone which were generated owing to the mechanical degradation of some nylon molecules, reducing the polymer density in the film. The lead ions diffused into the steel and thus provided a stronger bonding between the transfer film and its substrate. Since lead also acted as an agent to transport oxygen, it promoted mild oxidation of the polymer. This created strong valence bonds between the polymer film and its substrate so that the adhesive junctions were strengthened and the transfer film could not be peeled off easily during repeated sliding.

In another study with different Zn compounds, a thermosetting matrix, polyester was used [117]. The results suggested a similar conclusion that the wear behavior was controlled by the transfer film formed and its bonding to the counterface. Zn(C₁₈H₃₅O₂)₂/polyester composites exhibited a lower wear rate, while ZnO and ZnF₂ filled composites gave higher wear rates when compared to neat polyester. XPS analysis of the transferred materials on the tool steel disk during wearing of ZnO/polyester and Zn(C₁₈H₃₅O₂)₂/polyester composites are given in **Table 3**. Only the peaks corresponding to Zn(2p) and Zn(A) are discussed here for reasons of importance and clarity. For ZnO/polyester composite, the peaks at binding energy of 1021.8 eV in Zn(2p) and kinetic energy of 987.7 eV in Zn(A) correspond to Zn atoms in the ZnO compound. The binding energy of pure Zn is also 1021.8 eV but its kinetic energy should be 992.1 eV. Since there is no peak in Zn(A) at this kinetic energy, it may be concluded that pure Zn does not exist on the worn surface. For Zn(C₁₈H₃₅O₂)₂/polyester composite, the peaks at the binding energy of 1021.5 eV in Zn(2p) and the kinetic energy of 988.6 eV in Zn(A) correspond to Zn atoms in the zinc stearate compound; while the peak in Zn(2p) at 1021.8 eV and another at 991.9 eV in Zn(A) indicate the presence of pure Zn. Therefore, the results shown in **Table 3** clearly suggests the presence of pure Zn (by decomposition of zinc stearate) in the transfer film of Zn(C₁₈H₃₅O₂)₂ filled composite during sliding, while no dissociation has occurred in ZnO (and ZnF₂) filled composites. As the reduced

Zn end of the filler was highly reactive and bonded well to the steel counterface, it resulted in increased adhesion of the transfer film, which provided protection to the softer pin surface from the aggressive damage of the harder metal asperities.

2.5. Carbon nanotubes

Carbon nanotubes (CNTs) have exceptional elastic modulus, strength, electrical and thermal conductivity, and chemical and thermal stability [118, 119]. These properties have been related to the strength of the covalent carbon-carbon bond. Their aspect ratio exceeds 1000, as the length of a carbon nanotube is of the order of micrometers, while its diameter nanometers. The Young's modulus of a single-walled carbon nanotube was reported to be as high as 5 TPa. However, for multiple-walled carbon nanotubes, the measured Young's modulus was ~ 1.8 TPa and bending strength as high as 14.2 GPa [120, 121]. Thus, the tensile strength of a CNTs can be a hundred times that of steel while its density is one-sixth to one-seventh of steel [122]. Because of these properties, they have been considered as a possible reinforcing phase for polymers and it was shown that with an addition as low as 0.5% CNTs to a polymer, significant improvement in tensile modulus and strength can be achieved. In contrast, unlike other fillers, CNTs are hard to disperse, easily bundle together and entangle, leading to many defective sites in the composite materials, thus limiting the reinforcement efficiency of CNTs on polymers [123, 124]. Refer to [125, 126] for more extensive reviews on the dispersion of CNTs in polymers. The positive and negative aspects of adding CNTs to different polymer on the wear behavior are discussed below.

Cai et al. [127] in their investigation on polyimide (PI)/single-walled CNT nanocomposites have shown that they exhibit lower friction coefficients and wear volume losses than neat polyimide under dry sliding conditions against steel at a sliding velocity of 0.43 m/s, test duration 1.5 h, and normal loads in the range of 50-290 N. The differences were attributed to the quality of transfer films (**Figure 14**) in neat polyamide and nanocomposites, which led to adhesive wear damage in neat polyimide but significantly reduced scuffing and adhesion in the nanocomposites. However, the reasons for these differences in transfer films and the roles of CNT on the wear processes are unclear. Also, the wear volume losses are less compared to the neat material even at higher CNT

volume fractions. However, it should be noted that with more than 1 wt % CNT, it is hard to control the dispersion or separate the aggregated and entangled tubes in the polymer matrix.

A similar study on the friction and wear behavior of single wall carbon nanohorn (SWNH, a part of the carbon nanotube family)/polyimide (PI) composites was published recently [128]. SWNH was produced by CO₂ laser vaporization of graphite at ambient temperature [129, 130] and individual SWNH is a horn-shaped sheath composed of single-wall graphene sheet, 2-4 nm in diameter and ~50 nm long. The SWNH always aggregates to form a spherical particle (average diameter ~80-100 nm) with multiple horns (**Figure 15**). The friction and wear behaviors of the nanocomposites were tested against an austenitic stainless steel ball 9.2 mm diameter in a reciprocating friction tester. It was shown that the nanocomposites (with only 5 wt % SWNH) decreased significantly the wear and friction compared to neat PI (~2 orders of magnitude). In addition, the performance of these nanocomposites was also compared to the traditional PI/multi-wall CNT and PI/graphite nanocomposites. PI/SWNH composites outperformed PI/CNT and PI/graphite composites due to the disparities in their hardness and presence of transferred materials on the slider (stainless steel ball). Here, the hardness argument is questionable since wear not only depends on hardness (an indication of mechanical strength) of the composites, but also on many other intrinsic and extrinsic parameters, such as the dispersion state and distribution of the fillers, size distribution, mechanisms of wear debris formation, interfacial bond strength between fillers and matrix, etc. The argument of the presence of transferred materials on the slider ball is, however, reasonable if they form a thin, uniform and stable film on the counterface ball as discussed before in many studies. But comparing the specific wear rates (**Figure 16a**) and images of counterface slider balls of the four materials (**Figure 16b**) at identical test conditions does not seem to add up. The lower specific wear rates in the PI/SWNH nanocomposites are associated with non-uniform and patchy transferred materials; while the relatively higher specific wear rates in PI/graphite nanocomposites is associated with uniform transfer film. Additionally, no mechanisms of wear or the dispersion states of the composites were provided, which makes it difficult to interpret these results. Liu et al. [131] used three varieties of multi-walled CNTs (two of which were claimed to have different diameters, 20-30 nm *versus* 30-50 nm and the other is a carboxylated multi-walled CNT) in BMI and characterized their wear properties. Although they concluded that tribological properties of these nanocomposites depended on the diameter and

functionalization of CNTs, the results/evidence shown are not at all conclusive. They also noted a change in wear mechanism with the addition of CNTs from neat material and claimed this to be a result of the dispersion and improved interfacial strength between filler and matrix. Wang et al. [132] also showed similar results of reduced friction and improved wear resistance in polyacrylonitrile-methylmethacrylate/CNT copolymer nanocomposites (up to 3 wt % CNTs) prepared via an *in-situ* polymerization process and attributed them to the improved mechanical properties of the nanocomposites, particularly micro-hardness.

The effect of CNT addition on the wear behavior of UHMWPE was investigated [133] where it is shown that at small amounts of multi-walled CNT, wear was reduced quite dramatically (**Figure 17**) despite a slight increase in the friction coefficient (from ~0.05 in neat UHMWPE to 0.11 in 0.5 wt.% CNT/UHMWPE nanocomposite). Tests were performed on a ball-on-disk wear machine where the ball was made of silicon nitride (diameter ~6.35 mm) and the test conditions are: normal load = 5 N; sliding speed = 0.3 m/s; and test duration = 2 h. Also, the crystallinity did not change with addition of CNT, indicating that no significant internal structural changes occurred in UHMWPE. The improvement in wear was suggested to be caused by the variations in microstructure with the CNT content and load-bearing capacity; however, no such evidence was provided to correlate the structure-property relationships of these nanocomposites. In PTFE/multi-walled CNT nanocomposites, both friction coefficient and wear rate decreased with CNT volume fraction when slid against stainless steel under ambient conditions at 200 rpm, normal load 200 N, and test duration 2 h [122]. This was ascribed to the effective reinforcement of PTFE by CNT resulting in improved mechanical properties. This behavior was confirmed from the SEM micrographs of a cross-section of the worn surface of a PTFE and a PTFE/CNT composite (**Figure 18**). Similar to PTFE/ZnO nanocomposites just discussed, the fibrous structure observed for neat PTFE was absent in the case of PTFE/CNT composite. A crystal of PTFE has a ribbon-like structure and a smooth surface and consists of macromolecular chains. It is believed that as the outer diameter of CNTs (20-30 nm) is similar in magnitude as the dimensions of PTFE single crystals, CNTs intertwine with the crystals of PTFE so that no fibrous structure is found in the CNT/PTFE composite. Also, the PTFE crystals were drawn from the polymer surface by shear during the wear test; while CNTs effectively impede the drawing, thus improving considerably the wear resistance of the composite.

It has been reported that the self-lubrication effect of CNTs can be a mechanism of improvement in the wear performance of CNT/polymer nanocomposites. CNTs dislodged from the composites during sliding can transfer to the interface between the composite and slider and serve as spacers, thereby preventing direct contact between the two mating surfaces and slowing the wear rate and reducing the friction coefficient [123]. But to date, no convincing evidence is available on wear behavior of CNT/polymer nanocomposites to support this self-lubrication mechanism. Further, a recent study was reported on the tribological properties of UHMWPE filled with carbon nanofibers [134]. Although a slight improvement in wear resistance was noted, no in-depth analysis was given and the results are far from being understood.

From the above studies on polymer/CNT nanocomposites, it is realized that the mechanical and tribological properties seems to have been enhanced, but the understanding of the mechanisms of wear and friction are still at the early stage. Significant contributions are needed to improve the fundamental tribological knowledge of these novel functional materials.

2.6. Other miscellaneous fillers

Briscoe et al. [135] showed that adding an inorganic mixture of 5% CuO and 30% Pb₃O₄ to high-density polyethylene gave a significant reduction in wear. This was attributed to the formation of a strongly adhered polymer film on the metal counterface. Similar studies were reported by Bahadur et al. [136-138] and others [139] where they showed that wear was very much reduced by adding CuO and CuS to PTFE [138], CuS, CuF₂, CaO, PbS and AgS to nylon [137], CuO, CuS, CuF₂ and nano-sized ZrO₂ to PEEK [136, 139], and nano-scale Al₂O₃ to PPS [140]. The results of these studies confirmed that the formation of a transfer film on the counterface and its bonding are the key factors in the reduction of wear. For example, when CuS-nylon composite is rubbed against steel counterface, XPS studies revealed the presence of Cu in the transfer film of CuS/nylon composite confirming the decomposition of CuS during sliding wear [137]. This decomposition increased the adhesion between the composite transfer film and the counterface materials, thereby reducing the wear. **Figure 19** shows how the transfer film coverage changed with the addition of CuS to nylon 11 [137]. Transferred materials in the composite covered the

steel surface more uniformly and continuously compared to transfer materials of unfilled nylon where patches of materials are seen. In contrast, there are other studies, which indicated that wear increased in some polymers by adding nano-particles like BaF₂, CaF₂, (ZnF₂, ZnS, ZnO – as mentioned before), CuAc, SnS, SnF₂ and SnO [116, 141]. The reason for this behavior is shown to be the reduced adhesion of the transfer film to the counterface during sliding.

In an effort to separate the contributions of crystallinity and filler content towards the friction and wear properties, Bhimaraj et al. [142] prepared iso-crystalline PET/Al₂O₃ nanocomposites at various loading of Al₂O₃ by taking the samples to melt under pressure in the mold and cooling down at specific rates. The variation in wear rate and coefficient of friction *versus* filler content for 20% and 40% crystalline samples are shown in **Figure 20**, respectively. In 20% crystallinity samples, the friction coefficient of the nanocomposites is not significantly different from the unfilled sample; but the wear rates are lower compared to the neat polymer. In 40% crystallinity samples, although the wear rates of the filled samples are lower than the unfilled sample, the coefficients of friction are higher. It is also surprising to note that with increased crystallinity, wear rates increased; while friction coefficients are similar at identical compositions for all the samples. Thus, these differences cannot be satisfactorily explained by the crystallinity factor alone. The effects of nanoparticles, their dispersion and distribution, the tribochemical reactions occurring at the interface of the mating surfaces and so forth should also be considered.

Schwartz and Bahadur [140] studied the transfer film formation during wear and its counterface bond strength in PPS/Al₂O₃ nanocomposites. Large reduction in steady state wear was observed for PPS/Al₂O₃ nanocomposites compared to neat PPS up to 2 vol % of Al₂O₃ when slid against a tool steel disk at a sliding speed of 1 m/s under a nominal contact pressure of 0.65 MPa. These results were attributed to the formation of a uniform transfer film on the slider contact surface in the PPS/Al₂O₃ nanocomposites and reduced the aggressive damage of the harder steel asperities on the polymer pin. They also measured the tangential shear stress required to peel the transfer films from the counterface steel disk to compare the transfer film bond strengths by using a laboratory designed setup (**Figure 21a**). The setup consists of a thin, square copper tab (3.2 x 3.2 mm²), which was soldered to a copper strip; the free end of the strip was connected to a strain gauge load cell prior to loading. The tab was attached to a transfer film region with a quick-

setting cyanoacrylate adhesive. For this purpose, the disk surface was wetted with isopropyl alcohol which acted as a catalyst and a thin layer of the adhesive was applied to the tab. The curing time for the adhesive was 5 min. The counterface disk with the tab attached was rigidly held in a tensile testing machine and the tab was pulled down parallel to the plane of the disk at a crosshead speed of 0.42 mm/s and the maximum load was recorded. This provided a measure of the force needed to peel off the transfer film from the disk. The area of transfer film removed was then measured. In **Figure 21b**, the bond strengths for peeling the transfer films from the sliders after sliding on neat PPS and PPS/ Al_2O_3 nanocomposite were given. The reason for the increased bond strength in the nanocomposites was attributed to the mechanical interlocking of the transfer film in the counterface asperities and not any chemical interactions or tribochemical reactions. However, this does not explain the poor mechanical interlocking in neat PPS. Also, it was mentioned that as the shear strength of the adhesive was much larger than that of the transfer film bond strength, the measured value of the shear force would not be affected by the adhesive strength. But the use of alcohol to wet the surface and of the adhesive itself or the penetration of adhesive molecules during curing into the transfer film may affect the structure or bond strength of the transfer film with the disk and hence affect the results. In the case of non-uniform film formation, this method is very doubtful if it will give reliable results.

Lai et al. [143] showed that there was no significant change in friction coefficient, but the wear rate of PTFE composite was orders of magnitude less than that of pure PTFE. Acid treated nano-attapulgite was superior to untreated nano-attapulgite in enhancing the wear resistance of PTFE although the reasons were not clear. Moreover, the wear resistance of the composite increased monotonically with increasing treated attapulgite concentration.

In addition to the use of conventional fillers based on Cu, Pb, Zn and Si compounds for reducing the wear of polymers, unconventional compounds such as NiS, AgS, PbTe, and PbSe were also used. Zhao and Bahadur [3, 144] reported that the sliding wear of PPS was decreased by addition of AgS or NiS filler and increased with PbSe or PbTe. Graphite was also used because of its beneficial lubricating effect. It has a layer structure in which the atoms are arranged in a unit cell within each layer (hexagonal carbon sheets) and these layers are held together by weak van der Waals interactions. It is the motion of these carbon sheets, which are relatively free to slip over

each other (and also can be easily broken by shear forces under sliding conditions), that provides the graphite with its lubricity [145]. In a wear study of PPS with MoS₂ filler, a transfer film was observed on the counterface and better wear resistance was achieved in comparison to neat PPS [146]. MoS₂ decomposed to Mo and S during wear tests and MoO₃ and FeSO₄ compounds were formed. The presence of FeSO₄ in the transfer film indicated the tribochemical reaction between S and Fe in the counterface, which was believed to have promoted adhesion between the transfer film and the counterface and contributed to reduction in wear rate.

Apart from the abovementioned nanocomposites with several types of nano-fillers, even though nano-clay reinforced polymers have been widely used for different structural and technological applications, however, unfortunately, very few studies were dedicated to the wear behavior of these materials. We have recently studied the role of clay on the sliding wear characteristics of nylon 6 nanocomposites processed via different routes [75]. It is concluded that inhomogeneous distribution and dispersion of particles can result in extensive material loss due to disintegration and crumbling of the particle agglomerates. Subsurface cross-sectional TEM micrographs taken beneath the wear track (normal load of 5 N, sliding distance 400 m, against a Si₃N₄ ball of size ~6.3 mm) in this material show that voids are initiated either from within the intra-galleries or due to interfacial debonding at weak interfaces and also from inside these large clay aggregates where delamination also occurs (**Figures 22a and 22b**). It is thought that this subsurface damage will extend and detach to form wear debris caused by repeated sliding of the hard counterface asperities on the soft composite surface, thus resulting in abrasive damage in the form of intense plowing on the wear tracks. Moreover, it is shown that exfoliation or homogenous dispersion of nanoparticles alone is insufficient to improve the wear resistance; interfacial interactions of clay layers to matrix and exfoliated morphology are critical. Without very good bonding between clay layers and matrix, interfacial debonding occurs in addition to intra-gallery delaminations of the clay layers producing many voids within the plastic zone underneath the hard slider (**Figure 22c**), ultimately leading to excessive wear volume losses.

Thus, it is important to understand the effects of microstructural homogeneity and/or interfacial interactions in polymer nanocomposites for better appreciation of their tribological properties. This is clearly lacking in most of the studies discussed in this section. Below, a brief review of

the efforts made to improve the dispersion and interfacial interaction of the nanoparticles in polymers is given. The pros and cons of using different surface treatment methods on the wear behavior are also discussed.

2.7. Influence of particle surface treatment on the wear behavior

Although in-depth understanding of the wear damage mechanisms is yet to be clearly identified, the addition of nanoparticles has definitely enhanced the wear behavior of polymers. However, with decreasing size of particles, their specific surface area becomes larger, and the probability of particles to agglomerate increases leading to a number of loosened clusters of particles when added to the polymers. Creating high shear forces during processing of polymer nanocomposites was considered as an option to break up the strongly bonded aggregates of nanoparticles by using twin-screw extruders (mainly for thermoplastics) with different screw configurations and bead mills (for thermosets) where the collision and shear action of the ceramic balls were used to obtain higher shear forces [97]. Despite the importance of an applied external shear stress to achieve a finely dispersed structure, it is noted that if the matrix polymer does not have sufficient compatibility with the nanoparticles, stress alone cannot give fine dispersion of the nanoparticles. Also, as the inter-particle interaction is strong, the shear force achieved in conventional blending operations may often fail to separate the agglomerates into individual nanoparticles [147]. This is certainly not beneficial for tribological properties and can result in extensive material loss. The ideal condition for enhancement of mechanical, physical and other properties of polymer nanocomposites can be recognized if all the nano-sized particles are dispersed uniformly in the matrix and with good bonding (physical or chemical) to the polymer. To achieve this, many different approaches have been utilized, including both physical and chemical methods such as surface treatment of nanoparticles, use of coupling agents and compatibilizers, grafting agents, and so forth.

2.7.1. Physical treatment methods

Physical treatment methods mainly include either covering the surface of the filler with a low molecular weight surfactant, or encapsulating the inorganic filler particles with preformed or *in-situ* formed polymers. The usage of a surfactant will result in preferential adsorption of its polar

group on the high energy surface of the fillers. Consequently, secondary forces like hydrogen or electrostatic or van der Waals will result between filler particles and the modifier [148]. Besides this, encapsulating the particles with a preformed polymer includes usage of a macromolecular dispersant (hyper-dispersant), which essentially consists of two components: (i) a functional group like -OH, -NH₂, -COOH, -SO³⁻, -PO₄²⁻, and (ii) a solvable macromolecular chain, like polyolefin, polyester, polyacrylate, polyether, etc. The functional group anchors the dispersants to the particle surface via hydroxyl and electrostatic bonds, while the macromolecular chain helps dispersion in different media of low and high polarity. The hyper-dispersants have several advantages over conventional surfactants, since they can anchor strongly to the particle surface and are hard to desorb, and long polymeric chains interfere more effectively thus preventing re-agglomeration of particles. Indeed, they can only encapsulate the nanoparticle agglomerates but cannot diffuse into the agglomerates because of their long molecular profile. To overcome these problems, *in-situ* formed polymers (by either solution or emulsion polymerization) are used and expected to cover the particles more uniformly.

2.7.2. Chemical treatment methods

In relation to the physical treatment methods, chemical treatment methods are more effective and provide stronger interactions between matrix and nanoparticles via the modifier. Addition of a coupling agent is one of the most popular chemical methods. A number of coupling agents like silane, titanate and zirconia are used for this purpose. However, as these can only react with the exterior nanoparticles, the agglomerated nanoparticles would maintain their friable structure in the composites, which is undesirable. Therefore, for this purpose, recently, grafting treatment of nanoparticles was used to further improve the dispersion and bonding between the nanoparticles and matrix [25, 39, 149-153]. The low molecular weight of the monomers helps to penetrate into the agglomerated nanoparticles, filling the interstitial volume, and separating the nanoparticles further. In addition, it is believed that the surface of nanoparticles would become 'hydrocarbon' due to an increased hydrophobicity resulting from the grafting polymers [110]. This is beneficial for filler/matrix miscibility and hence enhances filler/matrix adhesion by chain entanglement and/or chemical bonding between the grafting polymers and matrix polymer. Besides, they can also react with the activated sites inside and outside the agglomerates. For example, an amino-silane coupling agent was used to improve the dispersion and bonding of alumina nanoparticles

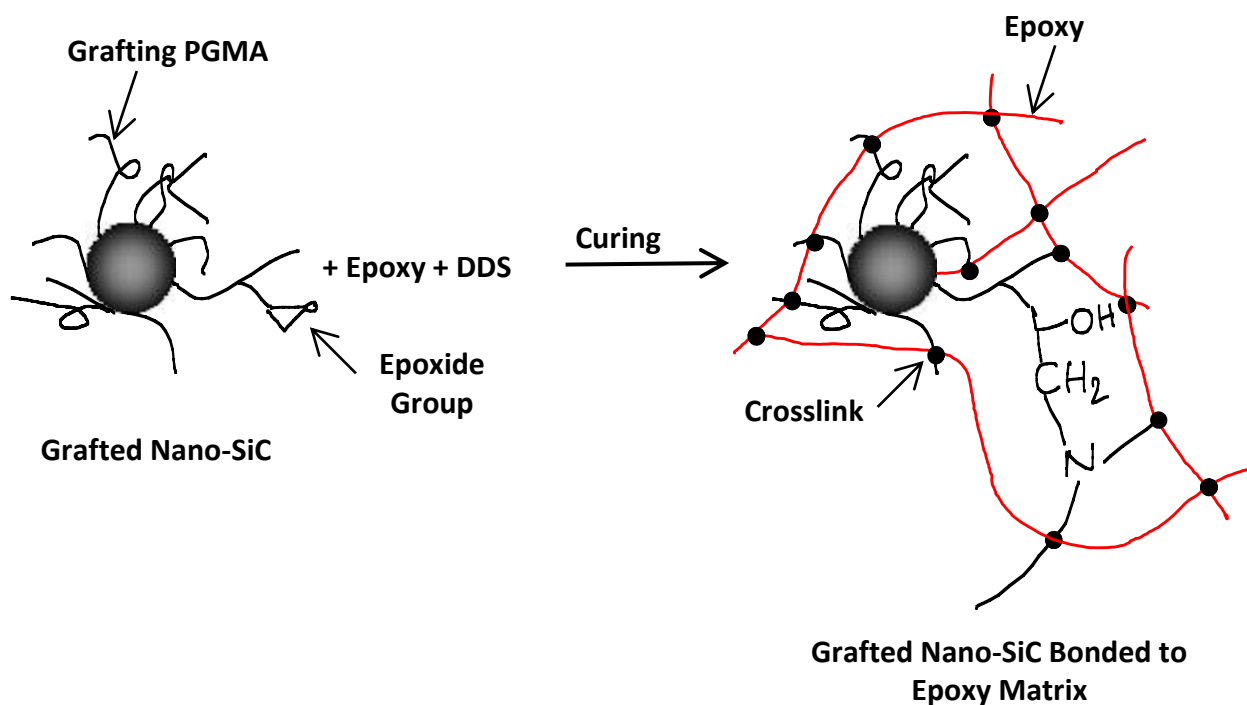
to epoxy [150]. The functional group ethoxyl of the coupling agent reacts with hydroxyl groups on the filler surface, while amino groups can react with epoxy groups. Many grafting techniques, such as chemical, irradiation and mechanical grafting are used to achieve this purpose. It has also been proven that irradiation grafting is superior to chemical grafting to improve the homogeneity of the grafting as under high energy irradiation, nanoparticles surfaces are equally activated both outside and inside the agglomerates.

2.7.3. Some examples signifying the influence of surface treatment of particles on wear

Improved sliding wear performance of epoxy nanocomposites filled with SiO₂, SiC and Al₂O₃ particles was obtained when the grafting method was applied to modify the nanoparticles by covalently bonding polyacrylamide (PAAM) or poly-glycidyl methacrylate (PGMA) directly onto the particles [39, 149, 150, 154]. PAAM and PGMA were selected because it was expected that their epoxide groups would take part in the curing reaction of epoxy forming 3-D networks throughout the composite resulting in a structure of PAAM-g-SiO₂/epoxy or PAAM-g-Al₂O₃/epoxy or PGMA-g-SiC/epoxy nanocomposites (**Scheme 2**). The main effects of the grafting polymers are to strengthen the loosened nanoparticle agglomerates and increase particle/matrix (grafted nanoparticles and matrix) interfacial adhesion through covalent bonding.

However, as the total amount of PAAM or PGMA in SiO₂-g-PAAM/epoxy nanocomposites or PGMA-g-SiC/epoxy nanocomposites was rather small, the possible reaction between PAAM and epoxy during curing was hard to be detected by infrared spectroscopy. Therefore, to confirm this reaction and the formation of 3-D networks, a model system consisting of PAAM homopolymer and epoxy (1/2 by weight) excluding other curing agents was chosen, where it was thermally treated following the same curing sequence as that applied for SiO₂-g-PAAM/epoxy or PGMA-g-SiC/epoxy nanocomposites [39]. The infrared spectra of PAAM and PAAM/epoxy showed considerable differences (**Figure 23**). In the PAAM spectra, the C=O peak at 1665 cm⁻¹, the NH₂ peak at 1616 cm⁻¹ and the CN peak at 1454 cm⁻¹ correspond to the primary amide; in PAAM/epoxy blends, the spectrum profile has been changed as a result of the transformation of partial primary amide groups and band overlap due to the incorporation of epoxy. Since the CNH peaks are at 1530-1550 cm⁻¹, a characteristic peak of secondary amide was not apparent, and instead the carbonyl peak appeared at 1656 cm⁻¹. It was deduced that this carbonyl peak in association

with the low wave number shift (compared with the carbonyl peak position of the primary amide) represents the existence of tertiary amide connected with the donor group, which supported the reaction between PAAM and epoxy during curing.



Scheme 2. Formation of three-dimensional networks, PGMA grafted nano-SiC and chemically bonded with epoxy resin through the reaction between epoxide groups and curing agent, DDS (4, 4-diamino-diphenylsulfone) (adapted from Ref. 152).

Unlubricated sliding wear tests of these materials (SiO₂-g-PAAM/epoxy or PGMA-g-SiC/epoxy nanocomposites) demonstrated that the frictional coefficient and the specific wear rate of nanocomposites are lower than those of unfilled epoxy and ungrafted nano-filler/epoxy composites [39, 40, 154-156]. SEM micrographs (**Figure 24**) clearly reveal these differences. Severe wear damage is seen on the unfilled epoxy associated with the detachment of bulk materials (**Figure 24a**). It is also obvious from the worn surface of neat epoxy that the main wear mechanism is fatigue, which is consistent with previous studies although in some cases combined fatigue and delamination does occur [39, 40, 155, 156]. Nevertheless, in the presence of nanoparticles, wear mode depends on how well the applied stress can be transferred between matrix and fillers. The worn surfaces of the composites filled with untreated SiC are characterized by scuffing (**Figure**

24b); while for the SiO₂-g-PAAM/epoxy nanocomposites, the worn surfaces are quite smooth and only a fine scar was observed (**Figure 24c**). The authors also mentioned that the fine wear debris dislodged from PGMA-g-SiC/epoxy nanocomposites acted as a lubricant in reducing the wear. However, no supporting information was provided.

The same authors also prepared polystyrene (PS) grafted nano-alumina, PAAM grafted nano-alumina, and PAAM grafted nano-silicon carbide epoxy composites and produced similar results of improved wear performance than non-grafted Al₂O₃ or SiC reinforced composites (PS was selected as its solubility parameter is similar to that of epoxy, and hence, good compatibility is expected between the treated nanoparticles and matrix) [149, 150]. In brief, with the usage of treated nanoparticles, the mechanism for the improvement in wear resistance was ascribed to the matrix enhancement rather than the nanoparticles themselves. The key effects of the grafting polymers are to strengthen the loosened nanoparticle agglomerates and increase the filler/matrix interfacial adhesion. We recently studied the sliding wear of silica/epoxy nanocomposites where the nanoparticles were synthesized using a sol-gel process [72]. Nanoparticles prepared *in-situ* in this way have a very fine particle size (~25 nm), homogenously dispersed at all loadings studied (up to 8 wt %) and are expected to have good interfacial interaction with the matrix. A typical TEM micrograph showing the uniform and fine dispersion of 6 wt % nanoparticles in an epoxy matrix is shown in **Figure 25a**. Despite these advantages, sliding wear tests on these materials indicated that nano-silica in epoxy did not reduce friction and specific wear rates when compared to neat epoxy for all nano-silica loading under the same testing conditions. All materials showed fatigue wear damage irrespective of silica loading.

The process leading to the formation of wear particles began on the surface with the evolution of cracks underneath a sliding spherical indenter. This type of cracks has been explained by contact mechanics for materials like glassy polymers [156, 157]. When a sphere indents on a plane, a compressive stress field is developed adjacent to and beneath the area of contact and surrounded by a tensile stress field. Tensile stresses are greatest at the surface and reach a maximum at the contact boundary between the sphere and the plane. The simultaneous application of a tangential force decreases the tensile stress at the front of the sliding sphere and increases it at the rear. If the surface is brittle and the indenter hard enough, a series of parallel curved cracks concave to

the sliding direction of the indenter are produced. Representative SEM micrographs of the worn tracks of neat epoxy and silica/epoxy at 6 wt % silica slid against a silicon nitride ball at a sliding speed of 0.1 m/s to a sliding distance of 500 m and a normal load of 1 N are given in **Figures 25b to 25e** at different magnifications. At higher loads, repeated stressing and un-stressing eventually produce extensive surface damage and generation of wear debris. TEM analysis on cross-sections beneath the wear track was also conducted to identify any subsurface damage due to the nanoparticles, that is, debonding between silica and epoxy that might have contributed to the increase in specific wear rate. However, no such damage processes were observed in all nanocomposites even at the high load of 8 N, probably a direct result of the strong interfacial bond between nanoparticles and matrix due to the *in situ* fabrication process.

2.8. Parameters controlling wear damage in polymer nanocomposites

From the discussions on wear damage in various polymer nanocomposites in previous sections, it appears that results and conclusions vary widely from study to study with only subtle changes in testing conditions, material/filler or even characterization techniques. The coupling of inherent tribological complexities with the poorly characterized nanocomposites and their mechanical properties make interpretation of experimental results even more difficult. It is unfortunate that despite the attribution of improvements in wear resistance of some polymer nanocomposites to their mechanical properties, only very few studies have listed or characterized the basic material properties and the microstructures/nanostructures of the composites.

Nonetheless, after comparing various studies and analyzing the results, it seems that the presence of nanoparticles by themselves or the improved material mechanical properties do not always lead to improvements in wear performance. A list of the mechanical properties of some polymer nanocomposite systems is given in **Table 4** from which it is evident that there is no direct dependence of wear rate on any one mechanical property.

One important factor mentioned for improvement in wear behavior of polymer nanocomposites is the tribochemical reactions between the fillers and the slider counterface which give uniform and stable transferred materials that are adhered to the counterface. Hence, it was proposed that

the Gibbs free energy change (ΔG) criterion be used to select fillers for wear reduction [3]. Gibbs free energy change (ΔG) provides a thermodynamic basis to determine whether or not a chemical reaction is possible. If ΔG for chemical reaction between filler and counterface metal is negative, a reaction is feasible. Conversely, if ΔG is positive for the contemplated chemical reaction, this is not feasible. Therefore, a good filler candidate for wear reduction is one for which the Gibbs free energy change for chemical reaction between the filler and the counterface metal is negative. The above hypothesis was tested on fillers for which XPS transfer film analysis results were available in the literature. The analysis related to this test is presented in **Table 5**. It should be added that a negative ΔG does not guarantee that the postulated chemical reaction will definitely occur. It simply indicates that such a reaction is feasible because the kinetics of reaction is also important. If the reaction is too slow, it may not occur practically. It is also conceivable that some fillers do not react chemically with the slider can still reduce wear since the conditions may be favorable to produce wear debris that promotes the development of a transfer film by its entrapment in the crevices of the surface asperities.

Further, in some cases of polar polymers such as polyamides and polymethylmethacrylate (PMMA), it was shown that wear was controlled by the formation and interaction of free radicals generated during the sliding process [158]. Lancaster [104] stated that the fillers reduced wear by modifying the counterface slider surface (polished and made smooth) and also by supporting the applied load. In a few cases, it is noted that the wear debris generated acts like a lubricant or third-body in reducing the wear rate by a rolling action.

In summary, although positive effects on wear properties with the addition of nanoparticles are seen in many studies, it should be remembered that these beneficial properties are realized under those particular testing conditions. If some testing conditions are changed or a different polymer or slider combination or some other contents of nanoparticles are used, the wear results may be very different. Further, in all the studies reported in the literature, the role of unbound (excessive) surfactant, which is often used to improve the dispersion of nanoparticles in a polymer matrix, during the wearing process (which may act as a lubricant) is unclear.

3. Nano-Wear Damage in Polymeric Materials

With increasing use of polymer-based nanocomposites in the nanotechnology industries where the applied loads are very low (ranging from μN and down to nN), it is important to have some fundamental understanding of their *nano-wear* damage mechanisms. However, there are few, if any, studies on this topic. Therefore, in this section, we will focus on the nano-wear of polymers and, in a few cases, polymer composites in order to provide some guidance for future studies on nano-wear of polymer nanocomposites. Also, despite numerous reports on the wear damage of polymer nanocomposites, no explicit correlations between material parameters and wear damage are available, which can accurately predict the service life-time relationship of these materials for different end applications. This situation is even worse in the *nano-wear* regime. So, in the next section, some aspects of wear modelling are presented to shed light on polymer nanocomposites.

Compared to wear damage at macro- and micro-levels, at the nano-level where the applied loads are very low, the response is different, as there may not be significant amount of wear particle generation and the original surface topography is more likely to remain intact for an extended period owing to the low wear rate. Under light loads, nano-wear is greatly influenced by the properties of the sliding surfaces rather than the bulk materials. Nevertheless, even in these conditions, adhesive wear was shown to operate. In a study on the atomistic mechanisms of contact formation between an atomically sharp nickel tip and a flat gold surface, molecular dynamic (MD) simulations showed wetting of the nickel tip by gold atoms (**Figure 26**) [159]. Additionally, atomic-level abrasive wear was also shown using MD simulations by scraping of a metal surface with diamond tip [160]. Ripple wear, a viscoelastic process where material is displaced from its original position, was observed in nano-wear conditions. However, here, it remains within the continuum of its environment [161]. Cutting wear was also observed even when the contact load between sliding surfaces is not large. Zhao and Bhushan [162] have shown that cutting abrasion occurs with normal loads of 40 to 80 μN using a diamond pyramidal tip on single crystal silicon. The debris produced was similar in morphology to metal-cutting debris (curly and stringy); but still no micro-cracks were noticed within the wear mark or on its edges.

Under nano-wear conditions, the frictional forces are likely to be dissimilar as the plowing due to wear particles and the inertial effect of the moving components are different, and affected by the surface forces such as adhesion and electrostatic forces [88, 163-166]. It has been reported that for inorganic materials, e.g., muscovite mica and highly oriented polygraphite, the friction coefficients at nanoscale as measured by a scanning force microscope are quite low compared to those at macroscale. This is attributed to the absence of a plowing contribution at the nanoscale [166]. These drastic changes under nano-wear conditions pose many fundamental questions on the molecular origins of conventional macroscopic behavior. To this extent, some studies have addressed the breakdown of continuum equations when the length scales approach atomic dimensions. Landman et al. [167] studied the stress distribution near a nanoscale contact and compared to that based on continuum elasticity. They found that for tips with a diameter of about 10 atoms, a strong qualitative correspondence existed between observed stresses and continuum calculations. However, the prediction of infinite stresses at the edge of contact cannot be correct by continuum theory.

As shown before, in a few instances, scanning probe and/or friction force microscopes are not only used for high resolution characterization of surface topography of materials, but are utilized increasingly for tribological studies (including surface roughness, scratch/wear, adhesion, friction, indentation, material transfer detection, boundary lubrication and nanofabrication/nano machining) of many surfaces including biological, at scales, ranging from atomic and molecular to microscale. Refer to [1, 42, 162, 164, 168-175] for some of the reviews on nanotribology of biological materials, carbon- and Si-based materials. Apart from these applications, it is also noted that over the past two decades, SPMs are increasingly used to measure currents, elasticity, magnetism, charges, forces and time-dependent processes (x , y , z , t -dimensions of a surface). Recently, the introduction of 'High Speed AFM' (HS-AFM) significantly changed the capability of collecting images, and by using this technique, a whole image can be captured in less than 20 ms and thus allow understanding of many speedy processes [176]. More significantly, AFM is configured as a Kelvin probe microscope and used to create surface potential maps with lateral resolutions around 50 nm and voltage resolution in the microvolt scale [177-180]. These surface potential maps are an important and useful means to characterize wear; a surface potential change is detectable even when there is minimum or no surface damage.

For nano-tribological applications, the tip and the AFM set-up are different from normal mode AFM. In a normal mode AFM or SFM, a sharp probe at the end of a cantilever bends in response to the force between the tip and the sample as it moves over the surface of a sample in a raster scan [169]. The tip would ideally consist of only one atom, which is brought in the vicinity of the sample surface. But, generally, the radius of curvature of most commercially available tips range between 20-80 nm. Nevertheless, improved fabrication processes have made it possible to produce tips with a radius of curvature of 2 nm, but at an expensive price. Generally, a very sharp diamond tip is used for these micro/nanotribology purposes and the AFM must have a heavy load mechanism for the tip and operate in a force mode. A force curve is produced, which is a plot of the tip deflection as a function of the vertical motion of the scanner. By analysis of the force-distance curve (**Figure 27**) [181] using a calibrated AFM tip, accurate quantitative information about the forces required to compress a polymer or pull a chain apart can be estimated. For stiffness measurements on polymers the indentation volume and the tip volume are also required. The selection of spring constant of the cantilever probe also plays an important role for identifying the small differences in response. Efforts are also made to determine the effect of both polymer and tip surface chemistry on adhesion hysteresis, and thus on the chemical component of friction on polymers by doing force curve measurements on polymer surfaces.

Since the introduction and development of these advanced characterization and testing tools, many studies have been reported on the nano-wear behavior of different materials, particularly metallic materials. Only limited work has been done on polymers, especially thin films that are used in the optical, optoelectronic and semiconductor industries to evaluate the wear and scratch resistance at very low loads for applications like MEMS, nanofabrication and nanopatterning. They include polystyrene, PMMA, gelatin, polyacetylene, polycarbonate (PC), PET, and random copolymers of styrene and benzocyclobutene (PS-BCB) [182-187]. However, no such study has been reported on polymer nanocomposites which are normally used for automotive and structural applications that seldom involve nanoscale wear and scratch.

Studies on neat polymers have reported the pattern formation of alternating ridges and troughs perpendicular to the direction of motion of the tip at low applied loads (in the range of nN to μ N)

irrespective of the polymer system suggesting that the mechanism of their formation is entirely dependent on the scan parameters and relatively independent on the polymer itself or polymer surface morphology [183-188]. The dimensions and spacing of these ridges were determined by the testing parameters. For example, with increasing load, ridge spacing and its height increased; with increasing scan line density, the extent of disruption of the material was also increased; and with decreasing scan angle, the ridge spacing increased. AFM micrographs for biaxially oriented PET film are shown in **Figure 28a** indicating the effects of applied load on the ridge (or bundle) density [185], and in **Figure 28b**, the scan angle and load on the ridge density and direction. In **Figure 28c**, the influence of scan line density on the extent of deformation on uniaxially oriented PET film after repeated scanning is displayed [184]. In contrast, in metallic materials/ceramics, these ridges and troughs cannot be observed. For example, a typical wear mark generated at a normal load of 40 μN for one scan cycle and imaged using AFM at 300 nN load is shown in **Figure 29a** and the inverted map of the same wear mark is given in **Figure 29b**, which clearly shows that material has been removed quite uniformly from the worn region [162].

In another study, Leung and Goh [182] tried to exploit the forces between AFM tip and polymer surface molecules to create nano-scale structures. They deposited a thin layer of amorphous PS ($\sim 1\ \mu\text{m}$ thick) on a mica substrate and then observed the time evolution of PS surface created by continuously scanning the surface while maintaining a constant force with an AFM (Nanoscope II, Digital Instruments) over a period of 5 minutes (**Figure 30**). The tip used for this purpose was made up of Si_3N_4 , operated at forces $\sim 100\ \text{nN}$ and speed $17\ \mu\text{m/s}$. As evident from **Figure 30a**, the surface was initially smooth and homogeneous within $1\ \text{nm}$; after 2 minutes scanning, the roughness was increased and structures $\sim 50\ \text{nm}$ in width were formed (**Figure 30b**); upon further scanning, these structures increased in width and thickness (**Figure 30c**) and resulted in the formation of distinct and oriented bundles normal to the scan direction with time. Very recently, Berger et al. [189] analyzed the effect of the physical architecture of polymer thin films on the degree and mode of nano-wear damage using an AFM. They found that cross-link density is the dominant material parameter controlling the extent and mode of wear damage. It was observed that cross-linking stabilizes the polymer film, preventing the formation of bundles (also called rippling) and reducing wear. For example, for non cross-linked polycarbonate, alternating ridges

and trough similar to the abovementioned studies were observed [190]. But for a cross-linked polycarbonate, ridges were not observed even for applied forces of 30-50 nN (**Figure 31**).

Nevertheless, there are still debates on the phenomenon of ridge formation. Meyers et al. [191] explained this behavior by comparing to the Schallamach waves [192], which are observed at a macroscopic level when sliding a rubber sphere in perfect contact with a rigid counter body, or vice versa. Waves were formed in the contact region and attributed to the inability of the rubber surface to sustain high shear forces [192, 193]. In another explanation, it was proposed that the ridge type of deformation occurs via molecular displacement and conformational changes rather than bond breakage, i.e., the primary deformation processes during nano-wear involve plastic deformation and viscous yielding; while extensive breaking of C-C bonds and the movement of material from the wear region do not occur [89, 185]. In summary, the mechanisms of nano-wear require further in-depth study and understanding. It would be interesting to see if ridges can form in polymer nanocomposites in the presence of a particle whose dimensions are comparable to or even less than the scale of deformation and AFM tip size.

4. Models for Different Wear Modes

The exact relationships between wear resistance, mechanical properties and physical/chemical characteristics of polymeric materials require test data be supplemented by analytical models and computer simulations since they provide additional insights on the role and significance of these individual factors. From semi-empirical models to recent molecular dynamic simulations, many attempts have been made to predict different wear modes and/or different stages of the wear process both qualitatively and quantitatively [66, 74, 76, 77, 194-215]. However, modeling wear damage is very complicated since many parameters must be properly included, e.g., contact geometry, topography, mechanical properties of mating surfaces, environmental (temperature, relative humidity, operating environment) and testing (load, speed, sliding distance, size and shape of counterface slider) conditions, type of debris, formation and stability of surface layers, etc. This process becomes more complex when nanocomposite materials are considered because the state of dispersion, reactivity of nanoparticles with slider, extent of mechanical and thermal degradations, size and angularity, etc may also influence the mode and extent of wear damage.

Several semi-empirical equations were proposed to estimate the wear volume of materials as a function of either the operating variables, such as load/pressure, speed, sliding distance/duration, or include properties such as counterface hardness, asperity height, shear strength of the polymer, and so forth. Some of these include Archard's adhesion model (equation 1) [74], Rabinowicz abrasion model (equation 2) [76], Ratner-Lancaster modified model for abrasion (equation 3) [77], or Khrushchov and Babichev model for two phase composites [203] to predict abrasion wear, Bitter [194] and Finnie [196] models for erosion (equations 4 and 5, respectively), etc. Although these wear models are introduced based on conventional materials like metals, they are successfully applied and in some cases slightly modified to suit polymers and their composites [60, 216-232]. For example, Clark and Wong [230] extended the Bitter model for erosion of brittle materials to polymers and composites. Tilly and Sage [231] showed that various polymers follow the same velocity dependence of erosion as metals, a power law of $V^{2.3}$. By considering the Finnie [196] and Bitter [194] erosion models, Tilly [232] has also introduced a model of the erosion process to investigate the influence of velocity, impact angle, particle size and weight of impacted abrasive for nylon, carbon fiber-reinforced nylon, epoxy, polypropylene and glass fiber-reinforced polymer. Lhymn and Wapner [233] derived an equation to explain the effect of particle size and particle velocity on the erosion rate in polymer composites by utilizing the concept of crack growth. Friedrich [234] used a simple correlation between material parameters (ratio of hardness and fracture energy) and erosive wear rate of polymers (a high value yielded a lower erosion resistance). The demand to use or develop new wear models for polymer-based materials is due to their increasing usage in transportation industries where the prediction of their durability is a prime consideration.

Bitter's model makes the hypothesis that the loss of material is the sum of material loss due to plastic deformation V_d (during impact, if the material elastic limit is exceeded, the surface layer is destroyed and fragments of it will be removed) and material loss due to cutting V_c (the particle strikes the body machining away material from the surface). Bitter assumed that deformation and cutting erosion occur simultaneously and their effects can be superimposed. He also introduced the concept of threshold velocity, v_{el} (calculated from Hertzian's contact theory using equation 4c) where a particle cannot erode the work-piece if its velocity is less than v_{el} . Thus, we have,

$$V_d = \begin{cases} \frac{M[\nu \sin \alpha - \nu_{el}]^2}{2\lambda_b}, & \nu \sin(\alpha) > \nu_{el} \\ 0, & \nu \sin(\alpha) < \nu_{el} \end{cases} \quad (4a)$$

$$V_c = \begin{cases} \frac{2MC'[\nu \sin \alpha - \nu_{el}]^2}{\sqrt{\nu \sin \alpha}} \left[\nu \cos \alpha - \frac{C'[\nu \sin \alpha - \nu_{el}]^2}{\sqrt{\nu \sin \alpha}} \phi_c \right], & \alpha \leq \alpha_0 \\ M \left\{ \frac{\nu^2 \cos^2 \alpha - K_1[\nu \sin \alpha - \nu_{el}]^{3/2}}{2\phi_c} \right\}, & \alpha \geq \alpha_0 \end{cases} \quad (4b)$$

$$\nu_{el} = \frac{1.54\sigma_y^{5/2}}{\sqrt{\rho_p}} \left[\frac{1-\nu_p^2}{E_p} + \frac{1-\nu_t^2}{E_t} \right] \quad (4c)$$

$$C' = \frac{0.288}{\sigma_y} \sqrt[4]{\frac{\rho_p}{\sigma_y}} \quad (4d)$$

$$K_1 = 0.82\sigma_y^2 \sqrt[4]{\frac{\sigma_y}{\rho_p}} \left[\frac{1-\nu_p^2}{E_p} + \frac{1-\nu_t^2}{E_t} \right] \quad (4e)$$

Here, α is attack angle, λ_b deformation wear factor (obtained experimentally), ν particle velocity, σ_y elastic load limit, ρ_p particle density, ν_p and ν_t are Poission ratios, and E_p and E_t are modulus of elasticity of particle and work-piece, ϕ_c material-dependent wear factor obtained experimentally, M is total mass of abrasive particles, and C' , K_1 are constants obtained from equations 4d and 4e.

In Finnie's model, (equation 5 below) it was assumed that a hard particle with velocity ν impacts a surface at an angle α . The material surface is assumed to be rigid plastic. V is the total wear volume of target material removed by multiple particles having a total mass M ; u ratio of vertical to horizontal force components, and Ψ ratio of the depth of contact to the depth of the cut; f flow stress of the eroded work-piece material; and constant c is used to compensate for the particles that do not follow the ideal model (some particles may impact with each other or fracture during erosion). That is, V is given by:

$$V = \begin{cases} c \frac{Mv^2}{\psi f k} \left[\sin(2\alpha) - \frac{6}{u} \sin^2(\alpha) \right], \tan \alpha \leq \frac{u}{6} \\ c \frac{Mv^2}{\psi f u} \left[\frac{u \cos^2(\alpha)}{6} \right], \tan \alpha > \frac{u}{6} \end{cases} \quad (5)$$

Further, Viswanath and Bellow [66] developed a dimensionless empirical equation to calculate the wear volume of polymers during sliding on a horizontal pin-on-disk machine (equation 6) where the volume of polymer material worn was expressed in terms of the operating conditions, properties of the polymer, and counterface roughness by expanding the work of Kar and Bahadur [202]. Dimensional analysis is generally based on the hypothesis that the solution of a problem can be represented by a dimensionally homogeneous equation in terms of the specified variables. Thus,

$$V = xN^p S^q T^r z^s E^{-3+p+r+s} \gamma^{3-2p-q-s} (C_p / K)^{r-q} \quad (6)$$

where the exponents p , q , r and s are obtained experimentally, x is a proportionality dimensionless wear coefficient, the ratio (C_p/K) is a factor controlling the thermal contribution in which C_p is the specific heat and K thermal conductivity, z counterface roughness controlling the contact area, E elastic modulus, N normal load, V wear volume, S sliding speed, T test duration, and γ surface energy.

Even recently, artificial neural network (ANN) approach has been introduced to predict the wear of polymers and composites [235-239]. Conventionally, ANN is a computational system that simulates the microstructure (neurons) of biological nervous systems. It is largely based on the interconnections between neurons, which are non-linear functions. Each input to a neuron has a weight factor of the function that determines the strength of the interconnection and thus the contribution of that interconnection to the following neurons. A database containing various testing details and material characteristics was used to train and test the neural network; this is used finally to predict the wear properties according to new input data. Clearly, the training data (and their number) that are developed by considering material compositions and testing details has a large influence on the prediction accuracy. This is a major disadvantage of this method.

Whilst all these equations/models are quite helpful to estimate the wear rate/volume of polymers in simple cases where only one wear mechanism takes place, wear normally is very complicated as explained above and there is always an overlap of two or three mechanisms depending on the testing conditions and materials used. This means that these simple functions do not always cover all the prevailing mechanisms that can occur during the sliding process. In fact, Meng and Ludema [214] have identified and analyzed nearly 200 ‘wear equations’ that are found in the literature involving a vast spectrum of material properties and operating conditions and they also listed more than 100 different variables and constants encountered in these equations. Despite their best efforts, there is still no sure way to predict with confidence, the tribological performance of a loaded pair of surfaces, whether dry or lubricated, even if all of their physical and chemical properties have been independently established. This is particularly true when a third body is present at the interface which may reduce the wear though not entirely eliminating it. To have a good prediction of the wear damage, it is important to consider all the physical and mechanical parameters for both the mating materials, testing environment, testing parameters, type, shape and size of debris, asperity size and density, and interaction between the different parameters.

As contact between two surfaces occurs at discrete contact spots or asperities where all the forces responsible for friction and wear are generated, several attempts were made to model the effect of surface roughness on the contact stresses during sliding. Comprehensive theories and models of surface roughness effects on friction and wear, such as Greenwood-Williamson (G-W) model [199], Majumdar-Bhushan (M-B) model [204], and Cantor set contact models [208, 240-242] have been proposed, which show the importance of understanding contact stresses and surface roughness. Since interfacial forces are found to be asperity size dependent, it is important to determine the size distribution of the contact spots and knowledge of their spatial distribution that illustrate the dynamics and force interactions between neighbouring spots. The G-W model is based on the assumption that all the asperities have the same radius of curvature. However, for surfaces with multiple length scales, the G-W model is inapplicable. To overcome the difficulties of the constant-radius assumption of the G-W model, Majumdar and Bhushan [204] proposed a fractal model of elastic and plastic contact between rough surfaces. The M-B model allows for asperity curvature to vary with size. Since some surfaces are fractal in certain length regimes and

non-fractal in others, a generalized theory of contact mechanics has been established based on the roughness characterization technique, which is in close agreement with experimental results. Contact models (based on Cantor sets) are also developed on fractal characterization of surfaces aiming to quantify the multi-scale nature of surface asperities with scale-invariant fractal parameters [208, 240-242]. Following these studies on contact of rough surfaces, other models were proposed using computational powers, such as Ren and Lee [206] who used large-scale numerical simulations to model the contact of 3-D rough surfaces, Sui [207] who gave solutions to rough contact problems based on Newton-Raphson procedure, etc.

Finite element (FE) analysis is also used to understand the contact and stress states produced by a steel ball sliding on the surface of a normally oriented fiber-reinforced polymer composite [197, 198]. For modeling, the fibers are assumed transversely anisotropic, the steel counterface and matrix isotropic, the fiber-matrix interface perfect and all fibers are in a hexagonal arrangement. Based on FE analysis, it is suggested that surface failure of matrix material is caused by the high shear stresses, the rear edges of the fibers located in the contact area can be cracked under high normal stresses, local debonding of a fiber is believed to be one of the starting steps of the wear process; and upon repeated sliding, the stresses will become even higher, producing more failure events in the near region of the contact area. Experiments confirm these results in that during scratching of these materials, with increasing load, matrix shearing, fiber/matrix debonding, followed by fiber cracking are observed (**Figure 32**). However, to simulate the wear processes accurately, the wear mechanisms and their changes must be known *a priori* during the simulation process. One way is to use the wear maps [47, 213] obtained experimentally; but it is impossible to develop wear maps for all materials under different contacts in different operating conditions. One of the better efforts is to combine an established wear equation with the FE method [209]. Here, the stress fields at the interface between the two contacting bodies are first determined by using a FE program; then, a known wear equation is implemented to estimate the wear at each node under the conditions of the obtained FE solution; this was again incorporated into the FE model in the form of changes in nodal heights or positions of the mesh. This process continues based on updated geometry of the contacting region, creating a loop, which implies a dynamic type of simulation. This approach has been used to simulate the wear profile and its evolution with sliding cycles for a polymer in contact with a metallic spinning disc [209]. However, in this

study, they did not consider frictional heating at the interface of the polymer-metal contact and it was also assumed that wear was proportional to contact pressure and sliding distance for a given sliding speed. Even though these authors have shown that the simulation results agree well with experimental results obtained under the same testing conditions, it may not always be true for all other materials and other testing conditions based on the specific assumptions made.

More recently, to provide better appreciation of the underpinning physics for the observed tribological phenomena, molecular simulation methods, such as molecular mechanics (MM) based on MD simulations, were used to study wear and cutting mechanisms, friction properties and indentation of different material systems, particularly for metallic materials [210-212]. For polymer nanocomposites, a few studies reported on calculating the binding energies between the components (polymer, surfactant and clay platelet) of polymer/organoclay nanocomposites based on polyamide 66, polyamide 6 and poly(butylene terephthalate-co-thiodiethylene terephthalate) copolyester [243-246], identifying the basal spacing of montmorillonite platelets in the presence of surface modifiers in a polymer [247, 248], atomic scale structure of intercalation of polymer between two clay platelets [249, 250], barrier properties of polymer/clay nanocomposites [243], structure of polymer/CNT system [251], and interactions between two spherical nanoparticles in a polymer matrix [252], etc. MD simulations can no doubt fill the gap between theoretical and experimental results on the mechanical behavior of different material systems. However, poor choice of simulation conditions may lead to meaningless results and so a thorough understanding of the strengths and weaknesses of MD simulations is also crucial for successful implementation of this method. For more information, reference is made to a recent review [253] on multiscale modeling and simulation of polymer nanocomposites.

For illustration, we refer to a MD simulation study that is intended to understand the interactions between the AFM probe tip and the self-assembled monolayer (SAM) on a metal surface during nano-wear so that high-quality and ultra-fine patterns can be scribed [215]. 850 molecules of single-chain alkanethiol ($\text{CH}_3(\text{CH}_2)_n\text{SH}$) were used to model the SAM and the AFM tip was modeled with up to 506 rigid silicon or carbon atoms. The substrate comprised five layers of fcc metal atoms such as Au or Ag, with each layer consisting of a maximum of 2,601 atoms. The simulation results revealed that the organothiol molecules were displaced and dragged by the

probe tip during scribing rather than removing or picking the molecules from the substrate (**Figure 33**). A bundle of SAM chains could be displaced along with the tip due to strong van der Waals interactions between the chains. It was also found that with increasing scribing speed the pattern width also increased and severe damage to the SAM molecules occurred around the tip. However, lack of in-depth experimental understanding of molecular interactions amongst the different components that control the wear damage in polymer nanocomposites has seriously limited the applicability of these techniques.

For nanotribological applications, the mechanical properties of the surface layers determine the performance of materials. Hence, conventional test methods, which focus on the bulk properties, are inappropriate for assessment of surface properties. For this reason, depth-sensing instruments (DSI) are widely used recently to characterize mechanical properties of materials (bulk and thin films) at the surface. Several review articles [254-262] and a book [263] are already available on this technique and dedicated towards its usage and applications to various materials. Thus, in the following section, it is briefly examined with particular relevance to polymer nanocomposites.

5. Background - Nanoindentation Technique

Instruments based on sensing the penetration depth at very low loads of up to nano-Newton have been developed in a number of research laboratories including that of Nishibori and Kinoshita [264], Pethica [265], Tsukamoto et al. [266], Oliver [267], Weiler [268], and CSIRO Division of Applied Physics, Australia [269]. The mechanical properties that are conveniently determined by using these techniques are hardness, elastic modulus, yield stress, and fracture toughness. Even bending experiments were performed using nanoindenter to gain insight on elastic deformation, yield and breaking of suspended beams [179]. The conventional way of hardness determination from the indentation techniques requires computation of residual indented contact area, which is often measured using the imaging techniques. This type of technique, if used for measuring the contact area of nanoindentations, the errors in measurements will be large. Additionally, this type of techniques can provide only the plastic response of the material tested and is not useful to understand the elastic and viscoelastic/plastic properties of the materials.

Thus, the well-known approach of compliance methodology has been introduced, which utilizes the force-displacement curve to determine the mechanical properties. A schematic of a loading-unloading curve for a viscoelastic-plastic material is shown in **Figure 34** [261]. The elastic, visco-elastic and plastic properties of the material are obtained from the unloading segment of the curve. In Figure 34, h_{\max} is maximum displacement of the indenter corresponding to the applied maximum load (P_{\max}) during indentation, h_r is residual displacement after removing the indenter and h_c is the intercept of the tangent line drawn from the first part of the unloading curve, which describes the elastic deformation effects [270-272]. The slope of this line represents the contact stiffness, S , evaluated at maximum displacement and h_c is considered as the actual value of the material displacement, which occurs mainly, but not exclusively, in a plastic fashion. The plastic work done in the viscoelastic-plastic case is represented by the area A1. Area A2 corresponds to the elastic work recovered during the unloading segment. In the case of a purely plastic material, the unloading curve is a straight line and $h_r = h_{\max}$ ($A2 = 0$).

However, the compliance method (of Oliver and Pharr) to derive these properties relies on the analysis of the unloading segment of the load-displacement response assuming it is elastic, even if the contact is elastoplastic. For most materials like metals and ceramics, estimation of hardness and elastic modulus using this approach gives accurate data, but for polymers because of their time- and rate-dependent behavior under load, this generally leads to an inappropriate evaluation of properties. In addition, the hardness determined from the nanoindentation measurements using the Oliver-Pharr methodology tends to be overestimated due to the Indentation Size Effect (ISE) [273, 274]. It means that the hardness at small depths is much higher than at large depths making the interpretation of nano-hardness difficult. Several mechanisms have been proposed to explain ISE, which includes the effects of friction between indenter and sample [275], presence of work-hardened surface layer [276], oxides, chemical contamination [277], etc. However, substantial understanding of these phenomena is required. Furthermore, pile-up and sink-in observed during nanoindentation are still under constant debate. Also, the reliability of the results obtained from depth-sensing instruments depends on many factors like temperature and humidity of the testing surrounding, specimen surface roughness, indenter tip curvature, etc.

Usually, there are three ways to accommodate the time-dependent effect: (a) application of an oscillatory displacement or force whereby the transfer function between load and displacement provides a means of calculating the storage and loss moduli, (b) increasing the unloading rate, and (c) a most common method of holding the indenter at maximum load for a period of time. If the dwell time (holding period) is absent, the sample will continue to deform viscoplastically during unloading. In some extreme cases of time-dependent behavior (when the unloading rate is low or the hold period is too short), the indenter displacement may continue to increase for a short time during the initial stage of unloading, appearing as a ‘nose’ (that is, indenter continues to sink into the specimen even though the load is decreasing) and thus affecting the calculation of contact stiffness and modulus [278]. To eliminate this bowing problem or nose, a considerable amount of hold period (usually 10-60 s) is used. However, since the severity of viscoelasticity depends on peak load, holding duration before unloading, and the unloading rate [279, 280], selection of appropriate holding duration and unloading rate are always doubtful. An alternative solution to eliminate creep effects in the post-experiment (data processing stage) was proposed by Tang and Ngan [281]. A Maxwell 2-element model was used to model the creep displacement at maximum load in a conventional load-displacement response and determine an equivalent expression for the contact stiffness that included the creep rate expressed as displacement over time. Oyen and Cook [282] proposed an approach to include elasticity, viscosity and plasticity in terms of modeling elements that represent a quadratic character of the contact equations rather than the intrinsic properties of the specimen material.

Moreover, plasticity during the holding period can also affect interpretation of the data. But most of the analyses/models mentioned before assume that plasticity occurs during the loading period, while viscoelastic processes happen during the holding periods. As both processes are involved, the viscoelastic response could not be determined directly from the holding period. To overcome this problem, Ovaert et al. [283] assumed a viscoelastic-plastic law following Bardenhagen et al. [284] and simulated the experimental indentation curves using mechanics models and through an iterative process elastic, plastic and viscoelastic parameters are adjusted. Seltzer and Mai [285] also proposed a simple method to extract the viscoelastic response from the total viscoelastic-plastic response during the holding period. This methodology developed as an inverse problem is particularly valid for materials with low modulus to yield stress ratio, where the plastic zone

under the indenter tip is large even at low indentation depths. The procedure essentially involves performing indentations with a spherical indenter at different creep loads and extrapolating these data to yield the pure viscoelastic (non-plastic) response.

Further improvement in nanoindentation test is obtained by a continuous stiffness measurement technique (CSM) [286], which is accomplished by imposing a small sinusoidally varying signal on top of a direct current signal that drives the motion of an indenter. The displacement response of the indenter at the excitation frequency and phase angle are measured continuously as a function of depth. Analyzing the in-phase and out-of-phase portions of the response allows for the measurement of contact stiffness at any point along the loading curve and not just at the point of unloading as in the conventional analysis. This means that with the usage of CSM technique, there will be no need for discrete unloading cycles for continuous measurement of mechanical properties. The CSM technique is also less sensitive to thermal drift since it is operated at frequencies larger than 40 Hz. A schematic of the CSM loading cycle is given in **Figure 35**.

5.1. Application of nanoindentation technique to polymer nanocomposites

The nanoindentation technique has been applied to probe the mechanical properties of several polymeric materials like PVC, PMMA, PET, poly(ethylene oxide) (PEO), poly(acrylic acid) (PAC), nylon 6, nylon 66, and so forth [271, 287-294]. The results showed that the mechanical properties obtained for different polymers are generally influenced by the testing procedure, penetration depths, and holding time utilized. More scatter of the data was particularly evidenced at penetration depths where the strain rates were extremely high and the physical imperfections of the indenters were of the order of magnitude of the penetrations. So far, limited work has been published using this technique to characterize the nanomechanical behavior of polymer nanocomposites. Some of them include PEO/clay [295], nylon 66/clay [296, 297], nylon 12/clay [298], epoxy/CNT [299], nylon 6/CNT [300], nylon 6/clay [301], polyester/clay [302], polystyrene/clay [179], and photopolymer/SiO₂ [303] nanocomposites. It has been shown that, in general, with increasing filler loading, the resistance to indentation of these nanocomposites gradually increases. Examples of this behavior are given in **Figure 36** for nylon 66/clay [296]

and nylon 6/multi-walled CNT nanocomposites [300]. Here, the penetration depths represent the contributions from both elastic and plastic displacements.

In addition, both hardness and elastic modulus are improved with increasing filler content with respect to indentation depth. Examples of this behavior are shown in **Figure 37** for nylon 66/clay [296] and nylon 6/multi-walled CNT [300] nanocomposites. Clearly, dramatic increases in hardness and elastic modulus are seen in all cases before 200 nm. This is attributed to ISE that may arise due to several reasons mentioned before in addition to blunting of the tip at the apex of the indenter leading to overestimates of properties at the near-surface, inaccurate determination of indentation area function at low depths, etc. Whilst the elastic modulus values obtained from nanoindentations are qualitatively comparable to those obtained from conventional tensile testing and dynamic mechanical analysis (DMA), they differ in absolute values. Possible origins for this discrepancy are: (i) different loading directions, (ii) frequency used for measurements, and (iii) differences in local and bulk crystallinity and cross-linking. Elastic modulus measured in a tensile test for injection and compression molded specimens differs from the direction in which it is measured during nanoindentation on respective samples. It is also known that the viscoelastic properties of polymers are dependent on test frequency. Generally, the higher is the frequency used, the higher the modulus obtained. In DMA measurements, low frequency (~ 1 Hz) is usually adopted. However, for indentation tests, much higher frequencies are used (usually ~ 35 -45 Hz). The other critical factor is the local crystallinity and cross-linking (important in nanoindentation) *versus* bulk crystallinity and cross-linking (important in tensile testing) of a polymer. These factors are especially important for polymer nanocomposites as the presence of nanoparticles is expected to affect polymer chain mobility and kinetics in their near vicinity and local chemistry at the interface, thereby yielding different properties from the bulk. Hence, it is expected that the measured mechanical properties have some numerical differences depending on the test method used.

Apart from measuring elastic modulus and hardness using nanoindentations, it is also important to mention the sensing of creep behavior of materials and its effect on other estimated properties. Since hardness is defined as the resistance to permanent deformation and is derived from the contact depth at maximum load, it is generally affected by the creep deformation which occurs

during the dwell time at maximum load. As mentioned before, if there is no dwell time, the polymer sample continues to deform visco-plastically during unloading and significantly distort the unloading curve leading to inaccurate values of the measured properties. In any case, both positive and negative influence of fillers on the creep resistance of polymers has been reported. Nai et al. [301] and Pinnaraia et al. [304] showed that the addition of clay improved the creep resistance of polymers. In contrast, Beake et al. [295] and Shen et al. [296] reported that adding clay particles to polymers made them more susceptible to creep. For example, **Figure 38** shows that the creep resistance of polyamide 66/clay nanocomposites is poorer than neat polyamide 66. However, these are only preliminary data and the role of nanoparticles on creep behavior is not reported. In fact, to date, few studies have focused even on the beneficial ‘bulk’ creep properties of polymer nanocomposites. Despite the absence of definitive evidences to explain the beneficial effects on the bulk creep properties of polymers by incorporation of nanoparticles, plausible reasons have been provided [305-308] and they include: (a) good interfacial strength between nanoparticles and matrix, (b) nanoparticles acting as restriction sites in retarding the mobility of polymer chains, and in a few cases (c) high aspect ratio of the nanoparticles.

Palacio and Bhushan [179] used nanoindentations to characterize the nanomechanical properties of polymer micro-beam structures used in bio-MEMS. Double anchored polymer micro-beams were fabricated using a soft lithography-based micro-molding process in which a poly(dimethyl siloxane) (PDMS) mold was filled with polymer (polystyrene and polystyrene/clay) solution and then the resulting structures were transferred to a pre-fabricated substrate. The substrate was a silicon wafer with a layer of SU8-25 negative tone photo-resist patterned by photolithography to create 25 μm wide channels for suspending the beams. Apart from measuring elastic modulus and hardness of the micro-beams, they conducted bending experiments to obtain yield and break strength data in the normal direction (listed in **Table 6**) on the suspended beams using a nano-indenter fitted with a conical diamond tip (coated with PMMA) of 1 μm radius of curvature and a 60° included angle. Evident from the SEM micrograph (**Figure 39**), the unfilled polystyrene beam deformed in a ductile manner when tested with an applied load of 3 mN. In the presence of clay, the beam exhibited minimal yielding followed by breakage in a brittle manner.

To summarize, though there are several other factors that may also need to be considered during nanoindentation (e.g., surface roughness, adhesion effects between tip and sample, loading rate, etc) to estimate and understand the nanomechanical properties of polymer nanocomposites, nonetheless, this technique offers the potential to deal with highly directional mechanical tests, use of extremely light loads and small displacements, extracting data on viscoelastic and viscoplastic effects, ability to separate mechanical behaviors of different material constituents, and capability of sensing creep in a short time.

6. Scratch Damage in Polymer Nanocomposites

Scratching is an alternative to conventional wear testing to evaluate the tribological properties of polymers. In the scratch test, a hard indenter is pressed onto the material under load and moves relative to the material; and scratch resistance is given by its ability to withstand mechanically induced surface damage under those conditions. Unlike an indentation process where the normal load is uniformly distributed beneath the indenter, scratching involves a high-friction induced sliding process. The indenter is fully supported by the specimen in the front and only partially by recovered material in the rear-half. The extent of recovery again depends on the stress-relaxation characteristics of the material in the contact zone. The scratch process is also divided into two stages where the first stage involves indenting the specimen until a specified load (which is a dynamic process) and then the second stage involves the sliding of the indenter on the sample surface (which is a quasi-static process) [309]. Different types of testing methods are developed over the last few decades to measure the resistance to scratching in polymers and these include: Ford five-finger test, Taber scratch tester, Pencil hardness, needle test, single pass pendulum sclerometer, Rover test, Chrysler crocking, instrumented indentation test, DIN abrasion, and recently, depth sensing instruments capable of scratching at nano-level on different materials. Wong et al. [310] have reviewed currently available scratch testing techniques for polymers and noted that a scratch test employing a linear load increase method provides sufficient repeatability of the test data. Scratch performance of polymers is determined by the material properties, test environment, and the stress field due to the scratching process (see below).

6.1. Types of scratches and their characterization methods

Polymers are highly sensitive to scratches and exhibit varying modes of deformation (ironing, ductile plowing, ductile/brittle machining, tearing, cracking, cutting, fragmentation, etc) even within a narrow range of contact variables like slider geometry (that determines the extent of the imposed strain), applied normal load, slider velocity, interfacial lubrication and test temperature; hence limiting their applications in automotive industry and superior performance optical devices [309, 311-322]. Ironing, generally results in the formation of smooth featureless grooves due to plastic or viscoelastic/viscoplastic deformation; while the plowing regime contributes to wave-like patterns, cracking, plastic drawing, and bamboo-like features. Cutting produces ribbons of material ahead of the scratching tip; while machining and/or fragmentation produces fragmented debris from the substrate and are generally associated with brittle failure. Besides, as mentioned before, there is always an overlap of different mechanisms in any particular contact process and the combination of the above mechanisms may represent the actual phenomena. This in turn confirms the complexity of scratch damage in polymers. **Figure 40** is a schematic of the most common types of material damage during scratching for (a) ductile, (b) ductile and brittle, (c) brittle and (d) elastomeric responses [313]. In addition, the surface tension of polymers has also been shown to play a role in influencing the scratch resistance. Brostow et al. [323] related surface tension, residual scratch depth, penetration depth, static and dynamic friction for epoxy when fluoropolymer was added. They demonstrated that increasing the surface tension, friction, penetration and residual depths were also increased.

To rationalize these various effects, Briscoe et al. [313, 324-326] have proposed the idea of using scratching maps for different polymers. The maps were drawn based on SEM examination of the qualitative nature of the damage caused on the scratched surfaces. For example, **Figure 41** shows a scratch damage map for polyethylene for different cone angles and loads at a constant scratch velocity of 0.0026 mm/s [326]. Evidently, this is a good way of easily identifying some broad deformation behavior of polymers such as ductile, brittle or elasto-plastic for some defined range of experimental parameters. The methods of constructing the scratch maps and the accuracy of boundaries are subjective and based upon qualitative judgment. Also, the selection of the type of prevailing deformation mechanisms is subjective. Thus, they can only be used as a guide and do

not accurately represent the extent of quantitative scratching damage. It is also impossible to develop scratch maps for all materials for different contacts in different operating environments.

Additional to the electron and surface probe microscopes for characterization of surface damage during scratching, several other methods are also developed so as to assess the scratch visibility in polymers. Light scattering from scratches (stress-whitening) is generally ascribed to structural inhomogeneity caused by deformation under the scratch, such as shear deformation zones, crazes and brittle cracks. In simple words, stress-whitening is observed if the dimension of an entity is greater than the wavelength of visible light. Hence, this optical reflectivity data may be used to identify and quantify damage during any surface interaction. Kody and Martin [327] developed a method using reflected polarized light microscopy to characterize quantitatively scattered light from scratches in polypropylene blends. Similar methods aimed at determining the perception of scratch visibility using an optical imaging system to quantify the visibility of a scratch on a polymer surface in terms of gray level has been established [328-330]. Also, as the magnitude of the optical contrasts are controlled by the illumination and viewing angles, angle-resolved light scattering measurements were used to probe the distribution of light from the sample and the scratches [330, 331]. However, all these characterizations and analyses are mostly done on neat polymers or polymer micro-composites. Very few studies are reported on the scratch damage of polymer nanocomposites despite the fact that they are widely used in the automobile industries in recent times.

Furthermore, these optical reflectivity methods cannot be used alone and must be supported by microscopy techniques. This is mainly due to the differences in the optical reflectivity characteristics of brittle and ductile scratch damage features. Generally, brittle cracks on the surface induce more serious optical damage to the material compared to ductile plastic deformation [327-330, 332]. Therefore, brittle scratch features make the surface more uneven and fragmented owing to the presence of cracks (or even fractures). This causes a rather pronounced scattering effect of light from the surface. For this purpose, Briscoe et al. [332] used a laser profilometer for measuring the optical reflectivity of the scratched polymer surfaces to obtain the relative extent of damage. Then, a statistical analysis was carried out and a parameter, ξ , was derived by taking into account the cumulative variation of the scatter effect of scratched

surfaces on the local reflectivity. By using this method, they showed that even within the ductile regime without major topographical changes the value of ξ varied significantly (**Figure 42**).

More recently, focused ion beam (FIB) microscopy is increasingly used for postmortem analyses of tribological response of a material [333-338]. Unlike most available surface characterization techniques, FIB can provide valuable information on the subsurface damage beneath the scratch/wear groove or nanoindentation site, which is necessary to correlate with the frictional response and identify the role of nanoparticles during deformation. In this technique, a beam of Ga^+ ions is used to both drill away and image the surface of a sample to examine cross-sections from an area of the sample with spatial resolution of <100 nm. For example, FIB micrograph of an indented surface and cross-sectional view of a 150 mN indent on a diamond-like carbon thin film which was coated on a stainless steel substrate is shown in **Figure 43** [335]. The concentric ring cracks observed on the surface were seen to propagate downward at an acute angle. In addition, radial and lateral cracking were also noticed initiating from the coating/substrate interface. Moreover, site-specific sections for TEM can be produced using FIB and a dual beam FIB/SEM system can analyze a 3-D microstructure by taking sequential sets of 2-D images and produce 3-D maps of the surface and subsurface structures [337, 338].

Nevertheless, the major disadvantage of this technique is the usage of ion beam for continuous milling, which is fine with ceramics and metals. For polymers, since they are beam sensitive, the beam damage experienced in the process of milling is significant and limits the applicability of this technique. This is particularly true when sections are prepared for TEM analyses using FIB technique. In contrast, by using conventional microtoming methods, the preparation of ultra-thin sections for TEM analyses from beneath the scratch/wear grooves is possible; but is a tedious process and requires extremely careful specimen preparation.

Furthermore, there are not many efforts on mathematical modeling to describe the stress fields induced by different slider geometries due to the complexities involved in the scratch damage processes, particularly for polymeric materials. Consequently, no explicit relationship between material parameters and scratch processes are available. For metals, several analytical and 3-D FE models have been suggested for plowing, adhesion and apparent coefficients of friction with

different indenter geometry [339-341]. For polymeric materials, the large elastic recovery makes the analysis and modeling difficult. In addition, accounting for the dynamic effects of the moving indenter along with the contact stresses and strains between indenter and surface is important. In the case of a cone-shaped indenter, a model is proposed for the volume of matter (V_{rem}) removed by plasticity below [342]:

$$\frac{V_{rem}}{l} = \frac{N \tan(\pi/2 - \theta/2)}{\pi H} \quad (7)$$

where H is hardness, N is normal applied load, θ apex angle of the tip, and l path length traversed by the tip. Therefore, the material volume removed during scratching (from equation 7) is dependent only on one material parameter, that is, hardness (assuming other testing conditions are constant). This is obviously too simple for characterizing the complex scratching process of polymers and their composites. This model is also based on the assumption that all matter in the path of a moving tip is removed from the surface. The partial recovery of highly viscoelastic and viscoplastic materials is not considered whereby some of the materials are not completely removed, but are rather pushed in front of the tip and to the sides of the groove and lie within the continuum of the scratch zone. This is particularly true for scratch/wear damage at nanoscales.

6.2. Parameters effecting scratch resistance

6.2.1. Young's modulus

Xiang et al. [309] investigated the mechanics of the scratch process based on the scratch model of Hamilton and Goodman [343] where the scratch process was assumed to be a superposition of indentation and sliding processes. A semi-spherical normal pressure was applied to simulate the spherical slider, and a proportionally distributed shear stress was applied to the specimen surface. They used a commercial FE package, ABAQUS[®], to simulate the elasto-plastic scratch damage behavior on polypropylene surface by a semispherical stainless steel indenter [344]. To establish, track and maintain contact between surfaces, the contact-pair (master-slave) algorithm for finite sliding in the FE package was used. von Mises shear yield criterion with isotropic hardening was utilized to describe the evolution of plastic flow. By examining the maximum principal stresses in the finite elements around the indenter tip, they also showed the damage mechanisms suffered by the scratched material.

Based on the model, they discussed how elastic modulus, yield stress and tensile strength affect the scratch damage resistance. For example, **Figure 44a** shows the effect of Young's modulus on the contact zone size and scratch residual depth having a high sensitivity as the modulus values fall below 1 GPa. In contrast, for polymers whose moduli are larger than 1 GPa, the effect on the contact zone size is much more gradual. In **Figure 44b**, it can be seen that when the size of the indenter changes, the transition in the scratch depth *versus* modulus curve moves to the right as the slider becomes sharper. These results imply that the polymer modulus should exceed 1 GPa to avoid severe scratch damage.

However, in our most recent study on scratch damage behavior of polyamide 6/organoclay nanocomposites having different extents of exfoliation of clay [345], it was shown that the proposed variations of contact zone size (and scratch depth) with Young's modulus were not always correct and a change in applied normal load (changing the scratch damage mechanism) changes the balance of this relationship. For a spherical slider with radius R , the contact zone size, a , can be calculated by:

$$d = R - \sqrt{R^2 - a^2} \quad (8)$$

where d is the scratch residual depth.

The effect of elastic modulus on the contact zone size calculated from equation 8 and scratch depths are given in **Figures 45a and 45b**, respectively. As the elastic moduli of all materials are >1 GPa (neat PA6, $A0 \sim 2.45 \pm 0.06$ GPa; PA 6/organoclay (90/10) nanocomposites (A1 and A2), A1 $\sim 4.53 \pm 0.04$ GPa is more exfoliated than A2 $\sim 4.12 \pm 0.05$ GPa), it is thought that changes in elastic modulus do not significantly affect the contact zone sizes and residual depths. However, from **Figure 45**, it is shown that the sensitivity of contact zone size and scratch depth with Young's modulus depends on the applied normal load. At lower applied loads, especially at 15 mN, variations of contact zone size and scratch residual depth with elastic modulus in nanocomposites compared to neat polymer are small (<10%) and similar to the observations reported in [309, 344]. However, at higher loads, e.g., 60 mN, considerable differences are noted (>25%) between neat PA 6 and its nanocomposites, suggesting that the proposed variations with modulus are not always correct.

6.2.2. Yield and tensile strengths

Xiang et al. [309] compared the yield zone sizes on both surface and subsurface for materials with different yield stresses obtained based on the von Mises yield criterion, and showed that, as expected, polymers with higher yield stresses are subjected to smaller plastic flow by scratching. Also, if the maximum tensile stress on the surface exceeds the tensile strength and if the tensile strength is less than the polymer yield stress, cracks are formed on the scratch surface. In general, it may be concluded that a certain level of rigidity in polymers is needed to obtain a small scratch depth if the polymer is prone to plastic flow induced damage; while polymers with high rigidity promote the formation of surface cracks and crazes. These observations are particularly important with polymer composites (see later).

6.2.3. Scratch hardness

Analogous to indentation hardness, Williams [319] defined the term scratch hardness (H_s) as the normal load N on the indenter over the projected load bearing area, equation 9, for a spherical indenter of size R . Many studies on scratch damage of polymers have used this parameter as a measure to quantify scratch resistance.

$$H_s = \frac{4N}{\pi R^2} \quad (9)$$

Briscoe et al. [313] argued that the viscoelastic recovery of polymers does not affect scratch width significantly and so it is reasonable to use the residual scratch width after testing to obtain the scratch hardness. Qualitatively, the trend of scratch hardness values followed a specific order in most of the studies signifying the importance of rigidity. However, similar to the traditional hardness methods, there are disadvantages of using the scratch hardness parameter as the exact scratch width and corresponding contact areas, particularly for nanoscratching conditions, cannot be exactly quantified. By plotting the normal load W against the projected area A (which is $\pi x^2/4$, x being the scratch width) gives a straight line whose slope is related to scratch hardness. **Figure 45c** shows such plots for neat polyamide 6 (A0) and its nanocomposites (A1 and A2) discussed above and their scratch hardness values were calculated and shown in **Table 7** along with some other systems selected from the published papers. Quantitatively, they seem to be smaller when compared to conventional hardness values (normally >100 MPa); but qualitatively, they follow the same trend. Further, it is important to note that even a couple of microns change in scratch

width (which is hard to measure exactly for polymers) results in considerable changes in scratch hardness as the slope changes quite dramatically. In a few studies, parameters like tangential hardness, dynamic hardness and specific grooving energy were also proposed to study scratch resistance of a material [311, 314, 318].

Hence, it is evident that scratch hardness and other mechanical properties can only be used as first estimates of the performance of a material and does not really provide a clear picture of the integrity and applicability of a material as discussed later.

6.3. Scratch morphology and damage mechanisms

In a study to identify the scratch resistance of nano-scale alumina filled gelatin composite films, Li et al. [346] used AFM to characterize the scratch morphology, depth and width of the scratch tracks. A stainless steel needle stylus was used for scratching and the tip of the stylus had a cone shape with a radius of curvature of about 15 μm and an angle of 27° . The angle between the sample surface and stylus was set to 45° and scratching done at 20 mm/s under a load of 200 mN. Examinations revealed that the resistance to scratching was greatly improved with the addition of as-received nanoparticle Al_2O_3 . The scratch depth decreased by almost a factor of 10, scratch width reduced from more than 25 μm to $\sim 18 \mu\text{m}$. The scratch track of the unfilled gelatin film exhibited extensive cracking and tearing (**Figure 46a**). Cracks generally occurred when the tensile stress behind the moving indenter exceeded the strength of the material. By adding 1 wt % as-received alumina nanoparticles, the scratch damage changed to ductile plowing with no cracks inside the scratch track (**Figure 46b**). When refined nano-alumina particles (from centrifugal sedimentation and selectively removing larger size particles) were added to gelatin film, further reductions in scratch width and depth were obtained. However, as shown in **Figure 46c**, despite no clear tearing/cracking in the scratch track, it seems that the sample surface was pierced by the indenter and dragged along producing considerable damage on either side of the track.

In other studies, it has also been shown that micro- and nano-scale fillers can reduce the scratch depth in both thermoplastic and thermoset composites by 50 % when compared to their unfilled counterparts [94, 347]. In another work, it is shown that the scratch tracks in neat polybutene

exhibited severe cracking when scratched with a stainless steel Hoffman's stylus with a contact arc of diameter 6.95 mm at 60 N [348]. When clay is added to the matrix, no cracks are seen in the intercalated nanocomposite. Instead, ironing, a less severe form of damage, is observed. In yet another study on the scratch resistance of polymer coatings incorporated with nanostructured tungsten carbide particles, Wang and Lim [349] showed that the scratch resistance of polymer coatings is strongly dependent on their hardness (which in turn also depends on the proportion of nanostructured tungsten carbide particles embedded in the coatings). Also, severe cracking is seen on the scratch tracks of the neat polymer coating with even fragments of material removed during the damage process. However, in reinforced polymer coating, the scratch track is even not clearly visible. In all these studies [346, 348, 349], when scratched, cracking is often found in low modulus polymers (unfilled polymers), while ductile plowing/ironing is observed in high modulus nanocomposites. This is surprising because based on the Hamilton and Goodman model [343], higher tensile stresses (behind the slider) on the surface of higher modulus polymers during scratching should promote surface cracking and/or debonding between phases of multi-phase polymers. Additionally, although the reinforcement of polybutene with clay particles [348] and polymer film/coating with nano-alumina [346] or tungsten carbide [349] particles clearly reduced the susceptibility to scratch damage and scratch penetration depth, the exact role of the nanoparticles on the damage behavior is not understood.

Wong et al. [320] used a progressive scratching load method on polypropylene-based systems to understand the surface damage transitions like the ductile to brittle or mar¹ to scratch and stress-whitening and relate them back to the changes in coefficient of friction. For example, **Figure 47** shows a scanned image of the scratch track where the load was progressively increased from 5 to 50 N. When this image is superimposed onto the friction force profile, strong correlation between the onset of stress whitening and change in friction force was evident. In another study, the effect of adding 10 wt % nano-CaCO₃ particles to polypropylene on its scratch resistance was studied [350]. It is shown that the incorporation of calcium carbonate particles increases scratch resistance of the polymer. The scratch subsurface features evaluated with bright field and cross polarized optical micrographs reveal the formation of shear bands in neat polypropylene (**Figure**

¹ mar damage can be treated as a less severe form of scratch damage where only small topographical changes are noted with no transfer of material to another area; but it causes a change in the ability of reflected light at the surface, that is, changes the gloss characteristics of the surface.

48a and 48b). When nanoparticles are added (**Figures 48c and 48d**), although the birefringence is seen (**Figure 48d**), it is claimed that the damage zone size is reduced. However, the scratch width seems to be similar in both cases and the surface features of the scratch reveal large scale damage including tears and cracks in both materials with or without fillers. In a study on scratch damage in ethylene-propylene (EP) copolymer [351], it is shown that when wollastonite fillers are added, the nanocomposite elastic modulus is increased (from 1.1 GPa to 2.3 GPa) and the residual scratch depth decreased (from 160 to 120 μm). Besides these advantages, SEM micrographs of scratched surfaces have shown major differences between neat polymer and composite suggesting poor surface integrity of the latter. **Figure 49a** shows the scratch damaged region of neat EP copolymer revealing the parabolic and repetitive pattern of scratch tracks with enhanced plastic flow; while in wollastonite-filled EP copolymer (**Figures 49b and 49c**), large voids are formed due to debonding/detachment of mineral particles from the matrix (caused by weak interfacial interaction between particle and matrix) at identical test conditions. Comparing Figures 49a-c, it is evident that the visual damage is also higher in the reinforced material with higher rigidity and suggests that for evaluating the scratch resistance/performance of a material, parameters like ‘scratch residual depth’ and ‘rigidity/toughness’ are not always the best and they can very often lead to false impressions about the scratching performance of the material.

Driven by recent advances in miniaturization of polymeric components for nano-technological applications, the applied load on these components is considerably lower in order to achieve certain purposes like nanofabrication or nanomachining and nanopatterning [168], which like mechanical scratching, require material surfaces to be deformed in the nano-scale and materials deliberately removed. There are many techniques available for nanofabrication/nanopatterning, ranging from milling techniques to non-traditional photolithographic and chemical methods. However, the major drawback of these methods is that it is difficult to control the morphology of the final nanostructures produced. Mechanical scratching has provided several advantages over others, for example, better control of applied normal load, scan size and speed, dry fabrication, and absence of chemical etchant or electrical field [170]. Hence, research on the nanoscratching technique can help develop mechanical scratching into a promising nanofabrication process or it can be used as a tool to identify material performance for nanotechnology applications.

The nanoscratch technique has been extensively used to evaluate the scratch, wear and frictional characteristics of polymers [352-355], polymer micro-composites [356, 357], thin films [358, 359], magnetic coatings and electronic materials [359, 360], and to a very much lesser extent on polymer nanocomposites [361, 362]. For the neat polymers, nano-scale surface damage has been correlated with material characteristics of epoxies, polymethylmethacrylate, and polycarbonate [355]. The results obtained suggested that under identical testing conditions, the surface damage is material specific. More importantly, mechanical properties of the polymers (e.g., ductility and modulus) were found to affect the surface damage observed and the deformation mechanisms involved when the polymers were scratched at the nano-scale. Under the same normal scratching load, shallower grooves were formed on higher modulus polymers; and the polymer plastically deformed if higher surface ductility was present. **Figures 50a and 50b** show SEM micrographs of polymethylmethacrylate (Young's modulus ~3.2 GPa) and polycarbonate (Young's modulus ~2.3 GPa), respectively, scratched by an indenter of radius 80 nm under identical test conditions [355]. Polymethylmethacrylate has lower scratch penetration depth than polycarbonate. But the latter has a smooth scratch groove that is characteristic of plastic deformation; while the former shows a damage surface with materials being peeled off at the rear of the indenter as the indenter scratched the surface. Hence, it may be concluded that when dealing with polymers and polymer composites, elastic modulus is not the only factor that should be considered in nanoscratching. It is instead necessary to have an in-depth understanding of all microstructural parameters and their response to scratching, relations of penetration depth with deformation and damage, significance of dispersion of particles and their interaction with matrix, and so forth.

For polyacetylene film, nanoscratching with an SFM tip produced a persistently periodic pattern perpendicular to the sliding direction under low applied loads [363]. The authors theoretically explained the pattern formation by a crack-opening mechanism. As the applied load was increased, this pattern gradually disappeared, and then the scratch mark became observable. When macro-tribology and nano-tribology are compared, wear and wear debris are observed for glassy polymer materials under macro-tribological conditions. In nano-tribological conditions, a periodic pattern at low loads and a scratch mark at high loads were found [363, 364]. It was also reported that at the nanometre scale, the friction coefficient depended on the sliding velocity for several polymeric materials. This behavior was explained on the basis of surface viscoelastic

properties instead of bulk viscoelastic properties [364]. In the case of polymer micro-composites, the nanoscratch experiment was also used to estimate the interfacial properties of the individual filler and matrix [356, 357].

Relatively, very few studies have focused on nanoscratch damage in polymer nanocomposites even though many of which are intended for use as optically transparent coatings. In an attempt to further enhance the luminescence and electroluminescence properties of poly(*p*-phenylene vinylene) (PPV) and its derivative poly(2-methoxy-5-(2'-ethylhexyloxy)-*p*-phenylene vinylene) (MEHPPV), they are integrated with porous silicon, that is, polymer/silicon nanocomposites were synthesized by filling the nanopores in a 7-10 μm thick porous silicon film with conjugated polymers [362]. To identify the deformation resistance of these materials, nanoscratch tests were performed using different normal loads from 20 to 41 μN with a diamond indenter (radius ~ 50 nm). As expected, original Si(100) exhibited greater resistance to nanoscratching as evident from the residual nanoscratch depths at all loads compared to other materials (**Table 8**); while porous silicon (PS) was more susceptible to scratching. Though both PPV- and MEHPPV-filled porous silicon materials exhibited relatively lower nanoscratch residual depths with respect to PS, they are still much higher and cannot match the original Si(100). Additionally, comparing the elastic modulus, hardness and fracture toughness values of PS and filled PS materials (Table 8), the variations in their nanoscratch depths cannot be properly explained. Further, reasons for the large differences in elastic modulus and hardness of PPV- and MEHPPV-filled PS materials are also not known. Yuan et al. [365] compared the scratch damage in binary polypropylene/clay and polyethylene/clay nanocomposites at two different loading conditions (a high load ~ 10 N and a low load ~ 1 mN). In brief, at high load, as expected, the scratch grooves of all materials are dominated by tearing and pulling of the matrix materials along the sliding direction although the intensity of tearing was less in clay reinforced (4 wt% loading) materials [365-367]. At low load, except for neat polypropylene, in all other materials as observed under a SEM, scratch grooves are smooth with no significant damage features [365]. In neat polypropylene, a repetitive pattern of scratch tracks was seen. It was concluded that the extent of scratch damage is governed by material properties such as % crystallinity, elastic modulus and yield strength. Nevertheless, it is important to note that indenters with different geometry were used to scratch at high and low loads. At low load, a three-sided pyramidal Berkovich indenter (made from diamond) with a

nominal radius of 20 nm was used at a sliding speed $\sim 1 \mu\text{m/s}$; but a Hoffman stylus (made of hardened steel) having a contact arc of 6.95 mm (and sliding speed 10 mm/s) was employed for scratching at high load. This clearly affected the mode of scratch damage and made comparisons difficult. Besides this factor, similar to the above study [362], correlation of different properties of these materials with average residual scratch depth (**Table 9**) do not lead to any definitive conclusion. It is also surprising to note that in the polypropylene system, adding 4 wt% of clay does not alter % crystallinity; but in the polyethylene system, it increases from 40 to 56%.

In a recent study on the nanoscratching of polyamide 66/clay nanocomposites (load = 1 mN; sliding speed = $1 \mu\text{m/s}$, and a Berkovich diamond indenter), we have also shown that the resistance to scratch penetration increases in the presence of finely dispersed clay layers even at a low weight percentage (5 wt %) [361]. Apart from the scratch resistance, generally, as is well known, to achieve large improvements even in stiffness and strength, nanoclay should be fully dispersed into individual layers throughout the polymer matrix to maximize the availability of reinforcing elements, their aspect ratio and interfacial contact with matrix [368, 369]. However, brittle cracks were observed on the surface in the wake of the moving indenter during nanoscratching of polyamide 66/clay nanocomposite (**Figure 51a**) even though the penetration was small ($210 \pm 7 \text{ nm}$ compared to $310 \pm 8 \text{ nm}$ for neat polyamide 66). TEM (cross-section beneath the scratch track) investigations showed the presence of submicron and nanocracks associated with clay layers up to 500 nm below the track (**Figure 51b**). The shear-stress dominant region of the scratch subsurface generated by internal sliding friction can easily cause debonding between phases or cracking. Because of the weak electrostatic interactions between the clay interlayers, intra-gallery delaminations of clay platelets occurred, and nanocracks were formed between the clay layers under the prevalent stress conditions. So, to reduce the brittle effects of clay nanolayers, when a third component (15 wt % of soft elastomeric dispersed phase, styrene-ethylene/butylene-styrene triblock copolymer grafted with 1.84 wt % of maleic anhydride (SEBS-g-MA)) was added, the scratch damage behavior was very different. When binary polyamide/clay nanocomposite was first prepared and then blended with SEBS-g-MA later, most of the clay layers were present in the polyamide 66 matrix with good dispersion and distribution. However, when clay was blended with rubber first and then mixed with polyamide 66, intercalated clay layers were mostly present in the SEBS-g-MA phase and little in the matrix. Post-mortem TEM

analysis of cross-sections beneath the scratch tracks revealed that in the first sequence, designated here as S1 (where the least amount of clay was present in the rubber), rubber particles close to the scratch track experienced severe stretching, and in a few cases, led to rubber/matrix debonding or rubber cavitation (**Figures 52a & 52b**), while the exfoliated clay in nylon matrix enhanced its resistance to scratch deformation supported by the lower scratch depth (240 ± 8 nm). In the second system S2, absence of clay in the matrix made it easier to deform plastically under the indenter with the largest scratch depth (365 ± 11 nm). While the rubber particles being stiffened by the intercalated clay were less able to deform or cavitate, however, debonding of clay from the rubber particles was observed indicating the weak bonding strength between intercalated clay and rubber (**Figures 52c & 52d**).

Furthermore, in our most recent study on binary polyamide 6/organoclay nanocomposites, it was shown that even the orientation and extent of exfoliation of clay layers are important parameters influencing the magnitude of scratch damage [345]. Residual depths are lower for scratches performed on the cross-sections (normal to the flow direction) of the nanocomposites compared to those on the surface (parallel to the flow direction); and greater scratch penetration resistance was noted for the nanocomposite with higher exfoliation extent of organoclay. This suggests the importance of proper physical and spatial characterization of nanocomposites. That is, while orientation and dispersion of clay layers are independent structural features, they must be simultaneously considered in determining the effective structural reinforcement in polymer/clay nanocomposites; otherwise, the results can be misleading if only dispersion or orientation of the structures is considered.

TEM images taken from the cross-section beneath the scratch track also revealed the formation of submicron to nanocracks that are associated with the clay layers similar to [361] though the extent of damage is more severe as higher loads (60 mN) are used (**Figure 53b**). Cracks initiated and grew downwards from the contact edges. More interestingly, clay layers are reoriented from nearly parallel to the sliding direction before scratching (**Figure 53a**) to an angle with the contact zone (**Figure 53b**). This is possible under large loads as the scratch grooves are formed beneath the indenter and so the clay platelets must also rotate with the plastically deformed matrix polymer. This again supports the argument on the ‘mobility’ of nano-fillers in Section 1 that the

nano-fillers can actively participate in the mechanical response of the matrix polymer under an applied stress field. However, this is unlike in microcomposites, such as carbon fiber/polymer, where extensive cracking of fibers is observed but no rotation of fibers in the subsurface can be found [197, 198].

7. Concluding Remarks and Future Work

Based on an extensive review of published literature, it appears that results and conclusions vary widely from study to study with only subtle changes of testing conditions, material/filler or even characterization techniques. The coupling of inherent tribological complexities with poorly characterized nanocomposites made interpretation of experimental results even more difficult. As evident in most of the studies, improved wear/scratch properties with the incorporation of nanoparticles in a polymeric matrix were attributed to the nanoparticles themselves or the mechanical properties like modulus and hardness or to the formation of transfer films. But after comparing various studies and analyzing the results, it seems that the presence of nanoparticles by themselves or the material mechanical properties do not always lead to improvements in wear/scratch properties. Hence, an in-depth understanding of all microstructural parameters and their response to tribological behavior must be properly evaluated. Even the transfer films are poorly characterized and only qualitative terms like ‘uniform’ or ‘coherent’ or ‘continuous’ were mostly used to describe them. In the majority of studies, very little attention was devoted to the shape, structure or type of wear debris.

It is therefore necessary to understand, depending on where and under what conditions the nanocomposites might be used, (a) the chemistry and chemical reactions that may occur between the two mating surfaces; (b) the influence of the by-products that may result from these reactions or during the wearing process; (c) the role of these reactions in promoting/stabilizing the film on the counterface; (d) possible inclusion of minor traces of foreign materials which may help achieve the above conditions, but it is important that these foreign materials do not cause degradations of other physical and mechanical properties that are required for the intended applications; and (e) quantitative understanding of nanoparticle dispersion, filler/matrix interface interactions, and transfer film properties.

The mechanisms of removal of materials during the wearing process should be studied in details as there has been little attention on the deformation and subsequent morphology of surface and subsurface materials within the wear/scratch tracks. However, this basic knowledge is critical to understand and control material damage and material removal. Moreover, there are few efforts to model the contact and stress fields induced by different slider geometries due to the complexities involved in wear/scratch damage, particularly for polymer nanocomposites at nano-scale. Thus, no explicit relationships between material parameters and scratch damage are available to date. It is hence necessary firstly to experimentally fully understand the material damage processes and material removal mechanisms, which are required to develop proper mechanics models for the design of scratch/wear-resistant polymers with nano-additives.

It is also worth noting that the tremendous interfacial areas and other beneficial properties of nanoparticles are important for many physical and mechanical properties of polymers. But their presence in polymers affects several other facets of these materials compared to neat polymers. For example, crystallization kinetics of polymer/clay nanocomposites differ from neat polymers since clay layers can act as heterogeneous nucleation agents and are capable of changing the crystalline form of polymer, rate of crystallization and percentage crystallinity. These changes in the crystallization kinetics can have a significant effect on the ultimate properties. Therefore, to better understand the influence of nanoparticles on polymer performance, many of these indirect effects should be accurately described and/or identified.

8. Acknowledgements

We would like to thank the Australian Research Council (ARC) for the continuing support of the project on '*Polymer Nanocomposites*'. We also acknowledge the contributions of all members of the Polymer Nanocomposites Group in the CAMT at Sydney University for useful discussions and constructive comments.

References

- [1] B. Bhushan, *Wear* 251 (2001) 1105.
- [2] J. Song and G. W. Ehresntein, in "Advances in Composite Tribology", edited by K. Friedrich (Elsevier Science Publishers B.V., Amsterdam, 1993) p. 19.
- [3] Q. Zhao and S. Bahadur, *Wear* 229 (1999) 660.
- [4] S. Bahadur, *Wear* 245 (2000) 92.
- [5] T. E. Fischer, *Annual Review of Materials Science* 18 (1988) 303.
- [6] L. S. Schadler, in "Nanocomposite Science and Technology", edited by P. M. Ajayan, L. S. Schadler and P. V. Braun (Wiley-VCH Verlag GmbH & Co. KGaA, Weinheim, 2003) p. 77.
- [7] R. A. Vaia and R. Krishnamoorti, *Polymer nanocomposites: synthesis, characterization, and modeling* (American Chemical Society, Washington D.C., 2002).
- [8] A. Sviridenok, M. Ihnatouski and T. Kovalevskaya, in 2nd Vienna International Conference on Micro- and Nano-Technology (Vienna, 2007) p. 73.
- [9] Z.-Z. Yu, A. Dasari and Y.-W. Mai, in "Processing and properties of polymer nanocomposites", edited by S. G. Advani (World Scientific Publishers, Singapore, 2006) p. 307.
- [10] A. Dasari, Z.-Z. Yu and Y.-W. Mai, *Macromolecules* 40 (2007) 123.
- [11] T. X. Liu, W. C. Tjiu, Y. J. Tong, C. B. He, S. S. Goh and T. S. Chung, *Journal of Applied Polymer Science* 94 (2004) 1236.
- [12] B. Qi, Q. X. Zhang, M. Bannister and Y.-W. Mai, *Composite Structures* 75 (2006) 514.
- [13] D. Shah, P. Maiti, E. Gunn, D. F. Schmidt, D. D. Jiang, C. A. Batt and E. R. Giannelis, *Advanced Materials* 16 (2004) 1173.
- [14] K. Wang, L. Chen, J. S. Wu, M. L. Toh, C. B. He and A. F. Yee, *Macromolecules* 38 (2005) 788.
- [15] A. S. Zerda and A. J. Lesser, *Journal of Polymer Science Part B-Polymer Physics* 39 (2001) 1137.
- [16] A. Dasari, S. H. Lim, Z.-Z. Yu and Y.-W. Mai, *Australian Journal of Chemistry* 60 (2007) 496.
- [17] X. H. Liu and Q. J. Wu, *Macromolecular Materials and Engineering* 287 (2002) 180.

- [18] X. H. Liu, Q. J. Wu, L. A. Berglund, J. Q. Fan and Z. N. Qi, *Polymer* 42 (2001) 8235.
- [19] D. Gersappe, *Physical Review Letters* 89 (2002) 058301.
- [20] D. Shah, P. Maiti, D. D. Jiang, C. A. Batt and E. P. Giannelis, *Advanced Materials* 17 (2005) 525.
- [21] T. H. Zhou, W. H. Ruan, M. Z. Rong, M. Q. Zhang and Y. L. Mai, *Advanced Materials* 19 (2007) 2667.
- [22] H. Chander, *Materials Science & Engineering R - Reports* 49 (2005) 113.
- [23] V. Balzani, *Small* 1 (2005) 278.
- [24] V. L. Colvin, *Nature Biotechnology* 21 (2003) 1166.
- [25] B. Wetzel, F. Hauptert and M. Q. Zhang, *Composites Science and Technology* 63 (2003) 2055.
- [26] C. Aymonier, U. Schlotterbeck, L. Antonietti, P. Zacharias, R. Thomann, J. C. Tiller and S. Mecking, *Chemical Communications* (2002) 3018.
- [27] X. C. Sun, *Molecular Physics* 100 (2002) 3059.
- [28] D. Qian, G. J. Wagner, W.-K. Liu, M.-F. Yu and R. S. Ruoff, *Applied Mechanics Reviews* 55 (2002) 495.
- [29] S. C. Tjong, *Materials Science & Engineering R - Reports* 53 (2006) 73.
- [30] S. C. Tjong, in "Nanocrystalline materials: their synthesis-structure-property relationships and applications", edited by S. C. Tjong (Elsevier, United Kingdom, 2006) p. 311.
- [31] M. Alexandre and P. Dubois, *Materials Science & Engineering R - Reports* 28 (2000) 1.
- [32] S. S. Ray and M. Okamoto, *Progress in Polymer Science* 28 (2003) 1539.
- [33] R. Krishnamoorti, R. A. Vaia and E. P. Giannelis, *Chemistry of Materials* 8 (1996) 1728.
- [34] G. Chigwada, P. Jash, D. D. Jiang and C. A. Wilkie, *Polymer Degradation and Stability* 88 (2005) 382.
- [35] B. Schartel, U. Knoll, A. Hartwig and D. Putz, *Polymers for Advanced Technologies* 17 (2006) 281.
- [36] L. Chang, Z. Zhang, C. Breidt and K. Friedrich, *Wear* 258 (2005) 141.
- [37] T. Kietzke, D. Neher, K. Landfester, R. Montenegro, R. Guntner and U. Scherf, *Nature Materials* 2 (2003) 408.
- [38] X. S. Xing and R. K. Y. Li, *Wear* 256 (2004) 21.
- [39] M. Q. Zhang, M. Z. Rong, S. L. Yu, B. Wetzel and K. Friedrich, *Wear* 253 (2002) 1086.

- [40] K. Friedrich, in "Advances in Composite Tribology", edited by K. Friedrich (Elsevier Science Publishers B.V., Amsterdam, 1993) p. 209.
- [41] S. Bahadur and C. Sunkara, *Wear* 258 (2005) 1411.
- [42] N. Ohmae, J. M. Martin and S. Mori, *Micro and Nanotribology* (ASME Press, New York, 2005).
- [43] A. Dasari, Z.-Z. Yu and Y.-W. Mai, *Polymer* 46 (2005) 5986.
- [44] A. E. Anderson, *Friction Lubrication, and Wear Technology* (ASM International, 1992).
- [45] B. J. Briscoe and S. K. Sinha, *Proceedings of the Institution of Mechanical Engineers, Part J: Journal of Engineering Tribology* 216 (2002) 401.
- [46] S. J. Kim, M. H. Cho, R. H. Basch, J. W. Fash and H. Jang, *Tribology Letters* 17 (2004) 655.
- [47] S. C. Lim and M. F. Ashby, *Acta Metallurgica* 35 (1987) 1.
- [48] R. S. Sayles, *Tribology International* 29 (1996) 639.
- [49] B. Briscoe, *Tribology International* 14 (1981) 231.
- [50] M. Godet, *Wear* 100 (1984) 437.
- [51] H. Bohm, S. Betz and A. Ball, *Tribology International* 23 (1990) 399.
- [52] S. W. Zhang and R. Y. He, *Journal of Materials Science* 39 (2004) 5625.
- [53] M. Garcia, M. de Rooij, L. Winnubst, W. E. van Zyl and H. Verweij, *Journal of Applied Polymer Science* 92 (2004) 1855.
- [54] S. M. Aharoni, *Wear* 25 (1973) 309.
- [55] H. Czichos, D. Klaffke, E. Santner and M. Woydt, *Wear* 190 (1995) 155.
- [56] S. W. Zhang, *Tribology International* 31 (1998) 49.
- [57] W. G. Sawyer, K. D. Freudenberg, P. Bhimaraj and L. S. Schadler, *Wear* 254 (2003) 573.
- [58] F. P. Bowden and D. Tabor, *Friction and lubrication of solids, Part I* (Clarendon Press, Oxford, 1950).
- [59] H. Czichos, *Meccanica* 36 (2001) 605.
- [60] C. Lhymn, *Wear* 114 (1987) 223.
- [61] N. P. Suh, *Wear* 44 (1977) 1.
- [62] S. Jahanmir, N. P. Suh and Abrahams.Ep, *Wear* 28 (1974) 235.
- [63] N. P. Suh, *Wear* 25 (1973) 111.
- [64] L. Lavielle, *Wear* 151 (1991) 63.

- [65] D. R. Williams, in "Advances in Composite Tribology", edited by K. Friedrich (Elsevier Science Publishers B.V., Amsterdam, 1993) p. 723.
- [66] N. Viswanath and D. G. Bellow, *Wear* 181 (1995) 42.
- [67] M. Q. Zhang, Z. P. Lu and K. Friedrich, *Tribology International* 30 (1997) 103.
- [68] P. J. Blau, *Tribology Transactions* 34 (1991) 335.
- [69] K. Holmberg, A. Laukkanen, H. Ronkainen and K. Wallin, *Tribology International* 38 (2005) 1035.
- [70] B. J. Briscoe, B. H. Stuart, S. Sebastian and P. J. Tweeddale, *Wear* 162 (1993) 407.
- [71] V. A. Bely, A. I. Sviridenok, M. I. Petrokovets and V. G. Savkin, *Friction and wear in polymer-based materials* (Pergamon Press, Oxford, 1982).
- [72] A. Dasari, On toughening and wear/scratch damage in polymer nanocomposites, <http://hdl.handle.net/2123/1911>, (The University of Sydney, Sydney, 2007).
- [73] R. Holm, in "Electrical Contacts", edited by H. Gerbers (Stockholm, 1946).
- [74] J. F. Archard, *Journal of Applied Physics* 24 (1953) 981.
- [75] A. Dasari, Z.-Z. Yu, Y.-W. Mai, G. H. Hu and J. L. Varlet, *Composites Science and Technology* 65 (2005) 2314.
- [76] E. Rabinowicz, *Friction and Wear of Materials* (John Wiley & Sons Ltd, 1965).
- [77] S. N. Ratner, I. I. Farberoua, O. V. Radyukeich and E. G. Lure, *Soviet Plastics* 7 (1964) 37.
- [78] W. A. Glaeser, in "Solid lubrication: fundamentals and applications", edited by K. Miyoshi (CRC Press, 2001).
- [79] N. P. Suh, M. Mosleh and J. Arinez, *Wear* 214 (1998) 231.
- [80] G. W. Blunn, P. S. Walker, A. Joshi and K. Hardinge, *Clinical Orthopaedics and Related Research* (1991) 253.
- [81] N. J. A. Tulp, *Acta Orthopaedica Scandinavica* 63 (1992) 263.
- [82] R. C. L. da Silva, C. H. da Silva and J. T. N. Medeiros, *Wear* 263 (2007) 974.
- [83] S. H. Rhee and K. C. Ludema, *Wear* 46 (1978) 231.
- [84] B. J. Briscoe, *Scripta Metallurgica Et Materialia* 24 (1990) 839.
- [85] P. A. Higham, F. H. Stott and B. Bethune, *Wear* 47 (1978) 71.
- [86] M. S. ElTobgy, E. Ng and M. A. Elbestawi, *International Journal of Machine Tools & Manufacture* 45 (2005) 1337.

- [87] I. Finnie, *Wear* 186 (1995) 1.
- [88] J. N. Israelachvili, *Intermolecular and Surface Forces* (Academic Press, London, 1985).
- [89] F. Dinelli, G. J. Leggett and P. H. Shipway, *Nanotechnology* 16 (2005) 675.
- [90] M. Guermazi, H. J. Hofler, H. Hahn and R. S. Averback, *Journal of the American Ceramic Society* 74 (1991) 2672.
- [91] M. J. Mayo, R. W. Siegel, A. Narayanasamy and W. D. Nix, *Journal of Materials Research* 5 (1990) 1073.
- [92] H. Hahn and R. S. Averback, *Nanostructured Materials* 1 (1992) 95.
- [93] M. Jain and T. Christman, *Acta Metallurgica et Materialia* 42 (1994) 1901.
- [94] C. B. Ng, L. S. Schadler and R. W. Siegel, *Nanostructured Materials* 12 (1999) 507.
- [95] B. Wetzol, F. Hauptert, K. Friedrich, M. Q. Zhang and M. Z. Rong, *Polymer Engineering and Science* 42 (2002) 1919.
- [96] L. Chang, Z. Zhang, L. Ye and K. Friedrich, *Tribology International* 40 (2007) 1170.
- [97] A. Gebhard, M. Englert, B. Bittmann, F. Hauptert and A. K. Schlarb, in *2nd Vienna International Conference on Micro- and Nano-Technology* (Vienna, 2007) p. 41.
- [98] X. Shao, W. M. Liu and Q. J. Xue, *Journal of Applied Polymer Science* 92 (2004) 906.
- [99] M. Z. Rong, M. Q. Zhang, H. Liu and H. M. Zeng, *Industrial Lubrication and Tribology* 53 (2001) 72.
- [100] K. Kumar and K. Kumar, *High Temperature Materials and Processes* 17 (1998) 271.
- [101] M. Q. Zhang, M. Z. Rong, S. L. Yu, B. Wetzol and K. Friedrich, *Macromolecular Materials and Engineering* 287 (2002) 111.
- [102] Y. J. Shi, X. Feng, H. Y. Wang, C. Liu and X. H. Lu, *Tribology International* 40 (2007) 1195.
- [103] J. K. Lancaster, *Journal of Physics D-Applied Physics* 1 (1968) 549.
- [104] J. K. Lancaster, *Tribology* 5 (1972) 249.
- [105] K. Tanaka and S. Kawakami, *Wear* 79 (1982) 221.
- [106] H. S. Kong, E. S. Yoon and O. K. Kwon, *Wear* 181 (1995) 325.
- [107] G. Shi, M. Q. Zhang, M. Z. Rong, B. Wetzol and K. Friedrich, *Wear* 254 (2003) 784.
- [108] Q. H. Wang, J. F. Xu, W. C. Shen and W. M. Liu, *Wear* 196 (1996) 82.
- [109] Q. H. Wang, J. F. Xu, W. C. Shen and Q. J. Xue, *Wear* 209 (1997) 316.

- [110] L. S. Schadler, K. O. Laul, R. W. Smith and E. Petrovicova, *Journal of Thermal Spray Technology* 6 (1997) 475.
- [111] Q. H. Wang, Q. J. Xue, W. M. Liu and J. M. Chen, *Wear* 243 (2000) 140.
- [112] Q. J. Xue and Q. H. Wang, *Wear* 213 (1997) 54.
- [113] Q. H. Wang, Q. J. Xue, W. M. Liu and J. M. Chen, *Journal of Applied Polymer Science* 78 (2000) 609.
- [114] H. X. Yan, R. C. Ning, G. Z. Liang and X. Y. Ma, *Journal of Applied Polymer Science* 95 (2005) 1246.
- [115] F. Li, K.-a. Hu, J.-l. Li and B.-y. Zhao, *Wear* 249 (2001) 877.
- [116] S. Bahadur and A. Kapoor, *Wear* 155 (1992) 49.
- [117] S. Bahadur, L. Zhang and J. W. Anderegg, *Wear* 203 (1997) 464.
- [118] T. W. Ebbesen and P. M. Ajayan, *Nature* 358 (1992) 220.
- [119] R. S. Ruoff and D. C. Lorents, *Carbon* 33 (1995) 925.
- [120] M. M. J. Treacy, T. W. Ebbesen and J. M. Gibson, *Nature* 381 (1996) 678.
- [121] E. W. Wong, P. E. Sheehan and C. M. Lieber, *Science* 277 (1997) 1971.
- [122] W. X. Chen, F. Li, G. Han, J. B. Xia, L. Y. Wang, J. P. Tu and Z. D. Xu, *Tribology Letters* 15 (2003) 275.
- [123] D. Qian, E. C. Dickey, R. Andrews and T. Rantell, *Applied Physics Letters* 76 (2000) 2868.
- [124] R. Andrews, D. Jacques, A. M. Rao, T. Rantell, F. Derbyshire, Y. Chen, J. Chen and R. C. Haddon, *Applied Physics Letters* 75 (1999) 1329.
- [125] X. L. Xie, Y.-W. Mai and X. P. Zhou, *Materials Science & Engineering R - Reports* 49 (2005) 89.
- [126] E. T. Thostenson, Z. F. Ren and T. W. Chou, *Composites Science and Technology* 61 (2001) 1899.
- [127] H. Cai, F. Y. Yan and Q. J. Xue, *Materials Science and Engineering A - Structural Materials Properties Microstructure and Processing* 364 (2004) 94.
- [128] A. Tanaka, K. Umeda, M. Yudasaka, M. Suzuki, T. Ohana, M. Yumura and S. Iijima, *Tribology Letters* 19 (2005) 135.
- [129] S. Iijima, M. Yudasaka, R. Yamada, S. Bandow, K. Suenaga, F. Kokai and K. Takahashi, *Chemical Physics Letters* 309 (1999) 165.

- [130] D. Kasuya, M. Yudasaka, K. Takahashi, F. Kokai and S. Iijima, *Journal of Physical Chemistry B* 106 (2002) 4947.
- [131] L. N. Liu, A. J. Gu, Z. P. Fang, L. F. Tong and Z. B. Xu, *Composites Part A - Applied Science and Manufacturing* 38 (2007) 1957.
- [132] C. Wang, B. Dong, G.-Y. Gao, M.-W. Xu and H.-L. Li, *Materials Science and Engineering: A* In Press (2008).
- [133] Y. S. Zoo, J. W. An, D. P. Lim and D. S. Lim, *Tribology Letters* 16 (2004) 305.
- [134] M. C. Galetz, T. Blass, H. Ruckdaschel, J. K. W. Sandler, V. Altstadt and U. Glatzel, *Journal of Applied Polymer Science* 104 (2007) 4173.
- [135] B. J. Briscoe, A. K. Pogosian and D. Tabor, *Wear* 27 (1974) 19.
- [136] S. Bahadur and D. L. Gong, *Wear* 154 (1992) 151.
- [137] S. Bahadur and D. L. Gong, *Wear* 162 (1993) 397.
- [138] S. Bahadur and D. Tabor, *Wear* 98 (1984) 1.
- [139] Q. Wang, Q. Xue, H. Liu, W. Shen and J. Xu, *Wear* 198 (1996) 216.
- [140] C. J. Schwartz and S. Bahadur, *Wear* 237 (2000) 261.
- [141] S. Bahadur, D. L. Gong and J. W. Anderegg, *Wear* 154 (1992) 207.
- [142] P. Bhimaraj, D. L. Burris, J. Action, W. G. Sawyer, C. G. Toney, R. W. Siegel and L. S. Schadler, *Wear* 258 (2005) 1437.
- [143] S. Q. Lai, T. S. Li, X. J. Liu and R. G. Lv, *Macromolecular Materials and Engineering* 289 (2004) 916.
- [144] Q. Zhao and S. Bahadur, *Wear* 217 (1998) 62.
- [145] Z. Zhang, C. Breidt, L. Chang, F. Hauptert and K. Friedrich, *Composites Part A - Applied Science and Manufacturing* 35 (2004) 1385.
- [146] M. H. Cho, S. Bahadur and A. K. Pogosian, *Wear* 258 (2005) 1825.
- [147] M. Z. Rong, M. Q. Zhang and W. H. Ruan, *Materials Science and Technology* 22 (2006) 787.
- [148] M. Q. Zhang, Z. Zhang and K. Friedrich, in "Polymer Nanocomposites", edited by Y.-W. Mai and Z.-Z. Yu (Woodhead Publishing Ltd., Cambridge, 2006) p. 540.
- [149] Q. L. Ji, M. Q. Zhang, M. Z. Rong, B. Wetzel and K. Friedrich, *Journal of Materials Science* 39 (2004) 6487.

- [150] M. Z. Rong, M. Q. Zhang, G. Shi, Q. L. Ji, B. Wetzal and K. Friedrich, *Tribology International* 36 (2003) 697.
- [151] M. Z. Rong, M. Q. Zhang, Y. X. Zheng, H. M. Zeng and K. Friedrich, *Polymer* 42 (2001) 3301.
- [152] M. Z. Rong, M. Q. Zhang, Y. X. Zheng, H. M. Zeng, R. Walter and K. Friedrich, *Journal of Materials Science Letters* 19 (2000) 1159.
- [153] M. Z. Rong, M. Q. Zhang, Y. X. Zheng, H. M. Zeng, R. Walter and K. Friedrich, *Polymer* 42 (2001) 167.
- [154] Y. Luo, M. Z. Rong and M. Q. Zhang, *Polymers and Polymer Composites* 13 (2005) 245.
- [155] R. Bassani, G. Levita, M. Meozzi and G. Palla, *Wear* 247 (2001) 125.
- [156] J. M. Durand, M. Vardavoulias and M. Jeandin, *Wear* 181 (1995) 833.
- [157] B. Bethune, *Journal of Materials Science* 11 (1976) 199.
- [158] A. I. Sviridyo, V. A. Bely, V. A. Smurugov and V. G. Savkin, *Wear* 25 (1973) 301.
- [159] U. Landman, W. D. Luedtke, N. A. Burnham and R. J. Colton, *Science* 248 (1990) 454.
- [160] J. Belak and I. F. Stowers, in "Fundamentals of Friction: Macroscopic and Microscopic Processes", edited by I. L. Singer and H. M. Pollock (Kluwer Academic Publishers, Dordrecht 1992) p. 511.
- [161] B. Gotsmann and U. Durig, *Langmuir* 20 (2004) 1495.
- [162] X. Z. Zhao and B. Bhushan, *Wear* 223 (1998) 66.
- [163] N. A. Burnham and A. J. Kulik, in "Handbook of Micro/Nanotribology", edited by B. Bhushan (CRC Press, Boca Raton, 1998) p. 247.
- [164] B. Bhushan, J. N. Israelachvili and U. Landman, *Nature* 374 (1995) 607.
- [165] J. Krim, *Surface Science* 500 (2002) 741.
- [166] E. Liu, B. Blanpain, J. P. Celis and J. R. Roos, *Journal of Applied Physics* 84 (1998) 4859.
- [167] U. Landman, W. D. Luedtke and J. P. Gao, *Langmuir* 12 (1996) 4514.
- [168] B. Bhushan, in "Handbook of Micro/Nanotribology", edited by B. Bhushan (CRC Press, Boca Raton, 1998) p. 335.
- [169] B. Bhushan, *Proceedings of the Institution of Mechanical Engineers Part J-Journal of Engineering Tribology* 212 (1998) 1.
- [170] B. Bhushan, *Wear* 229 (1999) 465.

- [171] M. Nosonovsky and B. Bhushan, *Materials Science & Engineering R - Reports* 58 (2007) 162.
- [172] D. S. Grierson and R. W. Carpick, *Nano Today* 2 (2007) 12.
- [173] S. H. Kim, D. B. Asay and M. T. Dugger, *Nano Today* 2 (2007) 22.
- [174] I. C. Gebeshuber, *Nano Today* 2 (2007) 30.
- [175] J. Krim, *Nano Today* 2 (2007) 38.
- [176] A. D. L. Humphris, M. J. Miles and J. K. Hobbs, *Applied Physics Letters* 86 (2005).
- [177] D. DeVecchio and B. Bhushan, *Review of Scientific Instruments* 69 (1998) 3618.
- [178] Y. Martin, D. W. Abraham and H. K. Wickramasinghe, *Applied Physics Letters* 52 (1988) 1103.
- [179] M. Palacio, B. Bhushan, N. Ferrell and D. Hansford, *Sensors and Actuators A - Physical* 135 (2007) 637.
- [180] J. M. R. Weaver and D. W. Abraham, *Journal of Vacuum Science and Technology B* 9 (1991) 1559.
- [181] S. Thalhammer and W. M. Heckl, *Cancer Genomics and Proteomics* 1 (2004) 59.
- [182] O. M. Leung and M. C. Goh, *Science* 255 (1992) 64.
- [183] D. D. Woodland and W. N. Unertl, *Wear* 203 (1997) 685.
- [184] B. D. Beake, P. H. Shipway and G. J. Leggett, *Wear* 256 (2004) 118.
- [185] B. D. Beake, G. J. Leggett and P. H. Shipway, *Polymer* 42 (2001) 7025.
- [186] G. J. Vancso, T. D. Allston, I. Chun, L. S. Johansson, G. B. Liu and P. F. Smith, *International Journal of Polymer Analysis and Characterization* 3 (1996) 89.
- [187] S. A. C. Gould, D. A. Schiraldi and M. L. Occelli, *Journal of Applied Polymer Science* 65 (1997) 1237.
- [188] B. Gotsmann, U. T. Duerig, S. Sills, J. Frommer and C. J. Hawker, *Nano Letters* 6 (2006) 296.
- [189] R. Berger, Y. Cheng, R. Forch, B. Gotsmann, J. S. Gutmann, T. Pakula, U. Rietzler, W. Scharrtl, M. Schmidt, A. Strack, J. Windeln and H. J. Butt, *Langmuir* 23 (2007) 3150.
- [190] R. Kaneko and E. Hamada, *Wear* 162 (1993) 370.
- [191] G. F. Meyers, B. M. Dekoven and J. T. Seitz, *Langmuir* 8 (1992) 2330.
- [192] A. Schallamach, *Wear* 17 (1971) 301.

- [193] A. A. Koudine and M. Barquins, *Journal of Adhesion Science and Technology* 10 (1996) 951.
- [194] J. G. A. Bitter, *Wear* 6 (1963) 5.
- [195] J. M. Challen and P. L. B. Oxley, *Wear* 53 (1979) 229.
- [196] I. Finnie, *Wear* 3 (1960) 87.
- [197] T. Goda, K. Varadi, K. Friedrich and H. Giertzsch, *Journal of Materials Science* 37 (2002) 1575.
- [198] K. Friedrich, K. Váradi, T. Goda and H. Giertzsch, *Journal of Materials Science* 37 (2002) 3497.
- [199] J. A. Greenwood and J. B. P. Williamson, *Proceedings of the Royal Society of London: Series A - Mathematical Physical and Engineering Sciences* 295 (1966) 300.
- [200] H. Hertz, *Journal für die Reine und Angewandte Mathematik* 92 (1882) 156.
- [201] K. L. Johnson, *Contact Mechanics* (Cambridge University Press, Cambridge, 1985).
- [202] M. K. Kar and S. Bahadur, *Wear* 30 (1974) 337.
- [203] M. M. Khrushov and M. A. Babichev, *Friction and Wear in Machines* 12 (1958) 5.
- [204] A. Majumdar and B. Bhushan, *Journal of Tribology-Transactions of the ASME* 113 (1991) 1.
- [205] M. A. Masen, M. B. de Rooij and D. J. Schipper, *Wear* 258 (2005) 339.
- [206] N. Ren and S. C. Lee, *Journal of Tribology-Transactions of the ASME* 115 (1993) 597.
- [207] P. C. Sui, *Tribology Transactions* 40 (1997) 243.
- [208] T. L. Warren and D. Krajcinovic, *Wear* 196 (1996) 1.
- [209] H. Benabdallah and D. Olender, *Wear* 261 (2006) 1213.
- [210] L. Fang, Q. Cen, K. Sun, W. Liu, X. Zhang and Z. Huang, *Wear* 258 (2005) 265.
- [211] T. H. Fang and C. I. Weng, *Nanotechnology* 11 (2000) 148.
- [212] J. A. Harrison, S. J. Stuart and B. W. Brenner, in "*Handbook of Micro/Nanotribology*", edited by B. Bhushan (CRC Press, Boca Raton, 1998) p. 525.
- [213] S. C. Lim, *Tribology International* 31 (1998) 87.
- [214] H. C. Meng and K. C. Ludema, *Wear* 181-183 (1995) 443.
- [215] I. H. Sung and D. E. Kim, *Applied Physics A - Materials Science & Processing* 81 (2005) 109.
- [216] S. K. Rhee, *Wear* 16 (1970) 431.

- [217] D. G. Bellow and N. S. Viswanath, *Wear* 162-164 (1993) 1048.
- [218] B. J. Briscoe, M. J. Pickles, K. S. Julian and M. J. Adams, *Wear* 203-204 (1997) 88.
- [219] A. E. Hollander and J. K. Lancaster, *Wear* 25 (1973) 155.
- [220] J. K. Lancaster, *Wear* 141 (1990) 159.
- [221] J. Larsen-Basse and A. Tadjvar, *Wear* 122 (1988) 135.
- [222] C. S. Ramesh, S. K. Seshadri and K. J. L. Iyer, *Wear* 156 (1992) 205.
- [223] B. K. Yen and C. K. H. Dharan, *Wear* 195 (1996) 123.
- [224] Z. Zalisz, P. H. Vroegop and R. Bosma, *Wear* 121 (1988) 71.
- [225] H. Q. Zhang, K. Sadeghipour and G. Baran, *Wear* 224 (1999) 141.
- [226] S. K. Sinha, W. L. M. Chong and S.-C. Lim, *Wear* 262 (2007) 1038.
- [227] M. Cirino, K. Friedrich and R. B. Pipes, *Composites* 19 (1988) 383.
- [228] A. Yabuki, K. Sugita, M. Matsumura, M. Hirashima and M. Tsunaga, *Wear* 240 (2000) 52.
- [229] A. A. Cenna, S. Allen, N. W. Page and P. Dastoor, *Wear* 254 (2003) 581.
- [230] H. M. Clark and K. K. Wong, *Wear* 186-187 (1995) 454.
- [231] G. P. Tilly and W. Sage, *Wear* 16 (1970) 447.
- [232] G. P. Tilly, *Wear* 23 (1973) 87.
- [233] C. Lhymn and P. Wapner, *Wear* 119 (1987) 1.
- [234] K. Friedrich, *Journal of Materials Science* 21 (1986) 3317.
- [235] Z. Zhang, N. M. Barkoula, J. Karger-Kocsis and K. Friedrich, *Wear* 255 (2003) 708.
- [236] Z. Y. Jiang, Z. Zhang and K. Friedrich, *Composites Science and Technology* 67 (2007) 168.
- [237] Z. Zhang and K. Friedrich, *Composites Science and Technology* 63 (2003) 2029.
- [238] Z. Zhang, K. Friedrich and K. Velten, *Wear* 252 (2002) 668.
- [239] K. Velten, R. Reinicke and K. Friedrich, *Tribology International* 33 (2000) 731.
- [240] G. Liu, Q. J. Wang and C. Lin, *Tribology Transactions* 42 (1999) 581.
- [241] T. L. Warren, A. Majumdar and D. Krajcinovic, *Journal of Applied Mechanics-Transactions of the Asme* 63 (1996) 47.
- [242] T. L. Warren and D. Krajcinovic, *International Journal of Solids and Structures* 32 (1995) 2907.
- [243] M. Fermeglia and S. Pricl, *Progress in Organic Coatings* 58 (2007) 187.

- [244] M. Fermeglia, M. Ferrone and S. Pricl, *Molecular Simulation* 30 (2004) 289.
- [245] M. Fermeglia, M. Ferrone and S. Pricl, *Fluid Phase Equilibria* 212 (2003) 315.
- [246] G. Tanaka and L. A. Goettler, *Polymer* 43 (2002) 541.
- [247] R. Toth, A. Coslanich, M. Ferrone, M. Fermeglia, S. Pricl, S. Miertus and E. Chiellini, *Polymer* 45 (2004) 8075.
- [248] R. Toth, M. Ferrone, S. Miertus, E. Chiellini, M. Fermeglia and S. Pricl, *Biomacromolecules* 7 (2006) 1714.
- [249] V. Kuppa, S. Menakanit, R. Krishnamoorti and E. Manias, *Journal of Polymer Science Part B-Polymer Physics* 41 (2003) 3285.
- [250] E. Hackett, E. Manias and E. P. Giannelis, *Chemistry of Materials* 12 (2000) 2161.
- [251] A. Maiti, J. Wescott and P. Kung, *Molecular Simulation* 31 (2005) 143.
- [252] J. S. Smith, D. Bedrov and G. D. Smith, *Composites Science and Technology* 63 (2003) 1599.
- [253] Q. H. Zeng, A. B. Yu and G. Q. Lu, *Progress in Polymer Science* 33 (2008) 191.
- [254] A. C. Fischer-Cripps, *Surface & Coatings Technology* 200 (2006) 4153.
- [255] S. J. Bull, *Journal of Physics D-Applied Physics* 38 (2005) R393.
- [256] C. A. Schuh, *Materials Today* 9 (2006) 32.
- [257] D. M. Ebenstein and L. A. Pruitt, *Nano Today* 1 (2006) 26.
- [258] B. Bhushan and X. D. Li, *International Materials Reviews* 48 (2003) 125.
- [259] A. C. Fischer-Cripps, *Vacuum* 58 (2000) 569.
- [260] M. R. VanLandingham, *Journal of Research of the National Institute of Standards and Technology* 108 (2003) 249.
- [261] B. J. Briscoe, L. Fiori and E. Pelillo, *Journal of Physics D - Applied Physics* 31 (1998) 2395.
- [262] A. C. Fischer-Cripps, *Surface and Coatings Technology* 200 (2006) 4153.
- [263] A. C. Fischer-Cripps, *Nanoindentation* (Springer, New York, 2004).
- [264] M. Nishibori and K. Kinoshita, *Thin Solid Films* 48 (1978) 325.
- [265] J. B. Pethica, in "Ion Implantation in Metals", edited by V. Ashworth, W. Grant and R. Proctor (Pergamon Press, Oxford, 1982) p. 147.
- [266] Y. Tsukamoto, H. Yamaguchi and M. Yanagisawa, *Thin Solid Films* 154 (1987) 171.

- [267] J. B. Pethica, R. Hutchings and W. C. Oliver, *Philosophical Magazine A - Physics of Condensed Matter Structure Defects and Mechanical Properties* 48 (1983) 593.
- [268] W. Weiler, *British Journal of Non-Destructive Testing* 31 (1989) 253.
- [269] T. J. Bell, A. Bendeli, J. S. Field, M. V. Swain and E. G. Thwaite, *Metrologia* 28 (1992) 463.
- [270] W. C. Oliver and G. M. Pharr, *Journal of Materials Research* 7 (1992) 1564.
- [271] B. J. Briscoe, K. S. Sebastian and M. J. Adams, *Journal of Physics D - Applied Physics* 27 (1994) 1156.
- [272] M. J. Mayo, R. W. Siegel, Y. X. Liao and W. D. Nix, *Journal of Materials Research* 7 (1992) 973.
- [273] R. Rodriguez and I. Gutierrez, *Materials Science and Engineering A - Structural Materials Properties Microstructure and Processing* 361 (2003) 377.
- [274] N. I. Tymiak, D. E. Kramer, D. F. Bahr, T. J. Wyrobek and W. W. Gerberich, *Acta Materialia* 49 (2001) 1021.
- [275] H. Li, A. Ghosh, Y. H. Han and R. C. Bradt, *Journal of Materials Research* 8 (1993) 1028.
- [276] H. Pelletier, J. Krier, A. Cornet and P. Mille, *Thin Solid Films* 379 (2000) 147.
- [277] M. Atkinson, *International Journal of Mechanical Sciences* 33 (1991) 843.
- [278] T. Chudoba and F. Richter, *Surface and Coatings Technology* 148 (2001) 191.
- [279] A. H. W. Ngan and B. Tang, *Journal of Materials Research* 17 (2002) 2604.
- [280] B. Tang, A. H. W. Ngan and W. W. Lu, *Journal of Materials Science-Materials in Medicine* 18 (2007) 1875.
- [281] B. Tang and A. H. W. Ngan, *Journal of Materials Research* 18 (2003) 1141.
- [282] M. L. Oyen and R. F. Cook, *Journal of Materials Research* 18 (2003) 139.
- [283] T. C. Ovaert, B. R. Kim and J. J. Wang, *Progress in Organic Coatings* 47 (2003) 312.
- [284] S. G. Bardenhagen, M. G. Stout and G. T. Gray, *Mechanics of Materials* 25 (1997) 235.
- [285] R. Seltzer and Y.-W. Mai, *Engineering Fracture Mechanics*, in press (2008).
- [286] X. D. Li and B. Bhushan, *Materials Characterization* 48 (2002) 11.
- [287] B. D. Beake, S. R. Goodes, J. F. Smith and F. Gao, *Journal of Materials Research* 19 (2004) 237.

- [288] D. Drechsler, A. Karbach and H. Fuchs, *Applied Physics A - Materials Science & Processing* 66 (1998) S825.
- [289] T. H. Fang and W. J. Chang, *Microelectronics Journal* 35 (2004) 595.
- [290] A. Flores and F. J. B. Calleja, *Philosophical Magazine A - Physics of Condensed Matter Structure Defects and Mechanical Properties* 78 (1998) 1283.
- [291] G. Hochstetter, A. Jimenez, J. P. Cano and E. Felder, *Tribology International* 36 (2003) 973.
- [292] K. Park, S. Mishra, G. Lewis, J. Losby, Z. F. Fan and J. B. Park, *Biomaterials* 25 (2004) 2427.
- [293] D. Penumadu, A. Dutta, G. M. Pharr and B. Files, *Journal of Materials Research* 18 (2003) 1849.
- [294] M. R. VanLandingham, J. S. Villarrubia, W. F. Guthrie and G. F. Meyers, *Macromolecular Symposia* 167 (2001) 15.
- [295] B. D. Beake, S. Chen, J. B. Hull and F. Gao, *Journal of Nanoscience and Nanotechnology* 2 (2002) 73.
- [296] L. Shen, I. Y. Phang, L. Chen, T. X. Liu and K. Y. Zeng, *Polymer* 45 (2004) 3341.
- [297] L. Shen, I. Y. Phang, T. X. Liu and K. Y. Zeng, *Polymer* 45 (2004) 8221.
- [298] I. Y. Phang, T. X. Liu, A. Mohamed, K. P. Pramoda, L. Chen, L. Shen, S. Y. Chow, C. B. He, X. H. Lu and X. Hu, *Polymer International* 54 (2005) 456.
- [299] X. D. Li, H. S. Gao, W. A. Scrivens, D. L. Fei, X. Y. Xu, M. A. Sutton, A. P. Reynolds and M. L. Myrick, *Nanotechnology* 15 (2004) 1416.
- [300] T. X. Liu, I. Y. Phang, L. Shen, S. Y. Chow and W. D. Zhang, *Macromolecules* 37 (2004) 7214.
- [301] M. H. Nai, C. T. Lim, K. Y. Zeng and V. B. C. Tan, *Journal of Metastable and Nanocrystalline Materials* 23 (2005) 363.
- [302] H. N. Dhakal, Z. Y. Zhang and M. O. W. Richardson, *Polymer Testing* 25 (2006) 846.
- [303] G. C. Xu, A. Y. Li, L. De Zhang, X. Y. Yu, T. Xie and G. S. Wu, *Journal of Reinforced Plastics and Composites* 23 (2004) 1365.
- [304] T. J. Pinnaraia and G. W. Beall, *Polymer-Clay Nanocomposites* (John Wiley & Sons Ltd., 2000).

- [305] J. L. Yang, Z. Zhang, K. Friedrich and A. K. Schlarb, *Macromolecular Rapid Communications* 28 (2007) 955.
- [306] Z. Zhang, J. L. Yang and K. Friedrich, *Polymer* 45 (2004) 3481.
- [307] J. L. Yang, Z. Zhang, A. K. Schlarb and K. Friedrich, *Polymer* 47 (2006) 2791.
- [308] J. L. Yang, Z. Zhang, K. Friedrich and A. K. Schlarb, *Applied Physics Letters* 91 (2007).
- [309] C. Xiang, H. J. Sue, J. Chu and B. Coleman, *Journal of Polymer Science Part B - Polymer Physics* 39 (2001) 47.
- [310] M. Wong, G. T. Lim, A. Moyse, J. N. Reddy and H. J. Sue, *Wear* 256 (2004) 1214.
- [311] B. J. Briscoe, A. Delfino and E. Pelillo, *Wear* 225-229 (1999) 319.
- [312] B. J. Briscoe, E. Pelillo, F. Ragazzi and S. K. Sinha, *Polymer* 39 (1998) 2161.
- [313] B. J. Briscoe and S. K. Sinha, *Materialwissenschaft Und Werkstofftechnik* 34 (2003) 989.
- [314] Y. N. Liang, S. Z. Li, D. F. Li and S. Li, *Wear* 199 (1996) 66.
- [315] B. Y. Ni and A. leFaou, *Journal of Materials Science* 31 (1996) 3955.
- [316] S. K. Sinha and D. B. J. Lim, *Wear* 260 (2006) 751.
- [317] H. X. Tang and D. C. Martin, *Journal of Materials Science* 38 (2003) 803.
- [318] O. Vingsbo and S. Hogmark, *Wear* 100 (1984) 489.
- [319] J. A. Williams, *Tribology International* 29 (1996) 675.
- [320] M. Wong, A. Moyse, F. Lee and H. J. Sue, *Journal of Materials Science* 39 (2004) 3293.
- [321] A. Dasari, J. Rohrmann and R. D. K. Misra, *Materials Science and Engineering A - Structural Materials Properties Microstructure and Processing* 364 (2004) 357.
- [322] A. Mudaliar, Q. Yuan and R. D. K. Misra, *Polymer Engineering and Science* 46 (2006) 1625.
- [323] W. Brostow, P. E. Cassidy, J. Macossay, D. Pietkiewicz and S. Venumbaka, *Polymer International* 52 (2003) 1498.
- [324] B. J. Briscoe, P. D. Evans, S. K. Biswas and S. K. Sinha, *Tribology International* 29 (1996) 93.
- [325] B. J. Briscoe, P. D. Evans, E. Pelillo and S. K. Sinha, *Wear* 200 (1996) 137.
- [326] B. J. Briscoe, E. Pelillo and S. K. Sinha, *Polymer Engineering and Science* 36 (1996) 2996.
- [327] R. S. Kody and D. C. Martin, *Polymer Engineering and Science* 36 (1996) 298.

- [328] I. M. Hutchings, P. Z. Wang and G. C. Parry, *Surface and Coatings Technology* 165 (2003) 186.
- [329] H. Nathani, A. Dasari and R. D. K. Misra, *Acta Materialia* 52 (2004) 3217.
- [330] P. Rangarajan, M. Sinha, V. Watkins, K. Harding and J. Sparks, *Polymer Engineering and Science* 43 (2003) 749.
- [331] E1392-96, Standard practice for angle resolved optical scatter measurements on specular or diffuse surfaces, (Annual Book of ASTM Standards, West Conshohocken, Pa, 1997).
- [332] B. J. Briscoe, E. Pelillo and S. K. Sinha, *Polymer International* 43 (1997) 359.
- [333] J. M. Cairney, R. Tsukano, M. J. Hoffman and M. Yang, *Acta Materialia* 52 (2004) 3229.
- [334] T. J. Steer, G. Mobus, O. Kraft, T. Wagner and B. J. Inkson, *Thin Solid Films* 413 (2002) 147.
- [335] Z. H. Xie, R. Singh, A. Bendavid, P. J. Martin, P. R. Munroe and M. Hoffman, *Thin Solid Films* 515 (2007) 3196.
- [336] H. Z. Wu, S. G. Roberts, G. Mobus and B. J. Inkson, *Acta Materialia* 51 (2003) 149.
- [337] B. J. Inkson, M. Mulvihill and G. Mobus, *Scripta Materialia* 45 (2001) 753.
- [338] B. J. Inkson, T. Steer, G. Mobus and T. Wagner, *Journal of Microscopy-Oxford* 201 (2001) 256.
- [339] J. L. Bucaille, E. Felder and G. Hochstetter, *Wear* 249 (2001) 422.
- [340] M. De Vathaire, F. Delamare and E. Felder, *Wear* 66 (1981) 55.
- [341] A. A. Torrance, *Wear* 123 (1988) 87.
- [342] C. Gauthier, S. Lafaye and R. Schirrer, *Tribology International* 34 (2001) 469.
- [343] G. M. Hamilton and L. E. Goodman, *Journal of Applied Mechanics* 33 (1966) 371.
- [344] G. T. Lim, M. H. Wong, J. N. Reddy and H. J. Sue, *JCT Research* 2 (2005) 361.
- [345] A. Dasari, Z.-Z. Yu, Y.-W. Mai and J.-K. Kim, *Nanotechnology* 19 (2008) 055708.
- [346] T. Li, Q. Chen, L. S. Schadler and R. W. Siegel, *Polymer Composites* 23 (2002) 1076.
- [347] E. Petrovicova, R. Knight, L. S. Schadler and T. E. Twardowski, *Journal of Applied Polymer Science* 78 (2000) 2272.
- [348] R. D. K. Misra, H. Nathani, A. Dasari, S. D. Wanjale and J. P. Jog, *Materials Science and Engineering A - Structural Materials Properties Microstructure and Processing* 386 (2004) 175.
- [349] Y. Wang and S. Lim, *Wear* 262 (2007) 1097.

- [350] S. Zokaei, R. L. Khosh and R. Bagheri, *Materials Science and Engineering A - Structural Materials Properties Microstructure and Processing* 445 (2007) 526.
- [351] A. Dasari, R. D. K. Misra and J. Rohrmann, *Polymer Engineering and Science* 44 (2004) 1738.
- [352] Y. C. Han, S. Schmitt and K. Friedrich, *Applied Composite Materials* 6 (1999) 1.
- [353] J. K. Kim and A. Hodzic, *Journal of Adhesion* 79 (2003) 383.
- [354] R. M. Overney, *Trends in Polymer Science* 3 (1995) 359.
- [355] J. S. S. Wong, H. J. Sue, K. Y. Zeng, R. K. Y. Li and Y.-W. Mai, *Acta Materialia* 52 (2004) 431.
- [356] A. Hodzic, Z. H. Stachurski and J. K. Kim, *Polymer* 41 (2000) 6895.
- [357] J. K. Kim, M. L. Sham and J. S. Wu, *Composites Part A - Applied Science and Manufacturing* 32 (2001) 607.
- [358] A. R. C. Baljon and M. O. Robbins, *MRS Bulletin* 22 (1997) 22.
- [359] P. A. Steinmann, Y. Tardy and H. E. Hintermann, *Thin Solid Films* 154 (1987) 333.
- [360] H. F. Wang, J. C. Nelson, W. W. Gerberich and H. E. Deve, *Acta Metallurgica et Materialia* 42 (1994) 695.
- [361] A. Dasari, Z.-Z. Yu and Y.-W. Mai, *Acta Materialia* 55 (2007) 635.
- [362] H. Ni, X. D. Li, H. S. Gao and T. P. Nguyen, *Nanotechnology* 16 (2005) 1746.
- [363] Z. Elkaakour, J. P. Aime, T. Bouhacina, C. Odin and T. Masuda, *Physical Review Letters* 73 (1994) 3231.
- [364] G. Haugstad, W. L. Gladfelter and R. R. Jones, *Journal of Vacuum Science and Technology A - Vacuum Surfaces and Films* 14 (1996) 1864.
- [365] Q. Yuan, N. Ramisetti and R. D. K. Misra, *Acta Materialia* 59 (2008) 2089.
- [366] A. Mudaliar, Q. Yuan and R. D. K. Misra, *Polymer Engineering & Science* 46 (2006) 1625.
- [367] R. R. Thridandapani, A. Mudaliar, Q. Yuan and R. D. K. Misra, *Materials Science and Engineering A - Structural Materials Properties Microstructure and Processing* 418 (2006) 292.
- [368] T. D. Fornes, D. L. Hunter and D. R. Paul, *Macromolecules* 37 (2004) 1793.
- [369] D. C. Lee and L. W. Jang, *Journal of Applied Polymer Science* 61 (1996) 1117.

Table 1. The identified compositions along with binding energies in the XPS spectra of the transfer films of CuO-, TiO₂-, and ZnO-filled PPS (adapted from Ref. 41).

2 vol.% CuO-filled PPS					
Compositions	C(1s)	O(1s)	S(2p)	Fe(2p)	Cu(2p)
Contaminated C	284.8				
C in PPS	284.8				
S in PPS			163.7		
Fe				707.0	
FeSO ₄		532.4	168.8	712.1	
Fe ₂ O ₃		530.2		710.9	
Cu, Cu ₂ O		529.8			929.8
CuO		526.8			932.3
Cu(OH) ₂		528.6			933.3
2 vol.% TiO₂-filled PPS					
Compositions	C(1s)	O(1s)	S(2p)	Fe(2p)	Ti(2p)
Contaminated C	284.8				
C in PPS	284.8				
S in PPS			163.7		
Fe ₂ O ₃		530.2		710.9	
FeSO ₄		532.4	168.8	712.1	
Ti					454.1
2 vol.% ZnO-filled PPS					
Compositions	C(1s)	O(1s)	S(2p)	Fe(2p)	Zn
Contaminated C	284.8				
C in PPS	284.8				
S in PPS			163.7		
Fe				707.0	
Fe ₂ O ₃		530.2		710.9	
ZnO		530.4			1021.8

Table 2. Coefficient of friction and wear volume loss in nanometer ZnO/PTFE composites sliding against stainless steel ring at a velocity of 0.431 m/s and load ~ 200 N for 30 min (adapted from Ref. 115).

Materials	Coefficient of Friction	Wear Volume (mm ³)
PTFE	0.202	174.60
PTFE + 2.5 vol.% ZnO	0.208	17.79
PTFE + 5.0 vol.% ZnO	0.212	12.88
PTFE + 7.5 vol.% ZnO	0.222	5.32
PTFE + 10.0 vol.% ZnO	0.201	3.07
PTFE + 12.5 vol.% ZnO	0.193	2.45
PTFE + 15.0 vol.% ZnO	0.209	2.02
PTFE + 17.5 vol.% ZnO	0.194	2.30
PTFE + 20.0 vol.% ZnO	0.209	2.91
PTFE + 22.5 vol.% ZnO	0.198	2.95
PTFE + 25.0 vol.% ZnO	0.203	4.03
PTFE + 27.5 vol.% ZnO	0.213	4.66
PTFE + 30.0 vol.% ZnO	0.207	5.64

Table 3. The identified compositions along with binding/kinetic energies in the XPS spectra of the transfer films of ZnO- and $\text{Zn}(\text{C}_{18}\text{H}_{35}\text{O}_2)_2$ -filled polyester (PES) composites (adapted from Ref. 117).

ZnO/polyester composite					
Compositions	C(1s)	O(1s)	Zn(2p)	Zn(A)	Fe(2p)
Contaminated C	284.5				
Alkyl C in PES	284.5				
C in phenyl	285.0				
PES –CO–	286.4	532.5			
PES –COO–	288.7	531.6			
ZnO		530.4	1021.8	987.7	
Fe_2O_4		529.8			710.8
Fe					706.8
$\text{Zn}(\text{C}_{18}\text{H}_{35}\text{O}_2)_2$/polyester composite					
Compositions		O(1s)	Zn(2p)	Zn(A)	
PES –CO–		532.5			
Zinc stearate		531.6	1021.5	988.6	
PES –COO–		531.6			
Fe_2O_3		530.0			
Fe					
Zn			1021.8	991.9	

Table 4. Mechanical properties and wear rates of some polymer nanocomposite systems. The sliding conditions are not listed here for reasons of redundancy.

Material Systems	Wear Rate	Modulus	Toughness	Hardness	Reference
Epoxy	40	2.85	33 [#]	-	95
Epoxy/4 vol% TiO ₂	15	3.20	46 [#]	-	
Epoxy/4 vol% TiO ₂ /9 vol% CaSiO ₃	4	4.30	32 [#]	-	
Epoxy	38	2.95	9.3 [#]	19 ^{##}	107
Epoxy/0.9 vol% nano-Si ₃ N ₄	7	3.08	13.2 [#]	20 ^{##}	
Polyimide	60	-	-	310 ^{##}	128
Polyimide/10 wt% Nano-horn	0.05	-	-	360 ^{##}	
Polyimide/10 wt% CNT	0.1	-	-	380 ^{##}	
Polyimide/10 wt% graphite	0.7	-	-	300 ^{##}	
Nylon 6	107	2.16	-	80 ^{**}	75
Nylon 6/5 wt% organoclay	76	2.77	-	90 ^{**}	
Nylon 6/5 wt% clay (water assist)	119	3.32	-	120 ^{**}	
Nylon 6/5 wt% clay	196	2.55	-	80 ^{**}	
Epoxy	84	2.8	0.2 ⁺	190 ^{**}	72
Epoxy/6 wt% nano-silica	281	3.0	0.4 ⁺	210 ^{**}	

Wear rate: 10⁻⁶ mm³/Nm

Modulus: GPa

[#]Charpy impact energy: kJ/m²

^{##}Vicker's hardness, MPa

⁺G_c – fracture energy, kJ/m²

^{**}from nanoindentation results, MPa

Table 5. Gibbs free energy (ΔG) in chemical reactions between different fillers and the counterface (Fe) (adapted from Ref. 3).

Polymer	Filler	Wear	ΔG (kJ/mol)	Chemical Reaction Equation	XPS Result
PPS	Ag ₂ S	Reduced	-59.7	$\text{Ag}_2\text{S} + \text{Fe} = \text{FeS} + 2\text{Ag}$	Ag, FeS, Fe ₂ O ₃
			-780.1	$\text{Ag}_2\text{S} + \text{Fe} + 2\text{O}_2 = \text{FeSO}_4 + 2\text{Ag}$	FeSO ₄
PPS	NiS	Reduced	-20.9	$\text{NiS} + \text{Fe} = \text{FeS} + \text{Ni}$	Ni, FeS, Fe ₂ O ₃
			-741.3	$\text{NiS} + \text{Fe} + 2\text{O}_2 = \text{FeSO}_4 + \text{Ni}$	FeSO ₄
PPS	PbSe	Increased	+26.4	$\text{PbSe} + \text{Fe} = \text{FeSe} + \text{Pb}$	Fe ₂ O ₃
PPS	PbTe	Increased	+6.7	$\text{PbTe} + \text{Fe} = \text{FeTe} + \text{Pb}$	Fe ₂ O ₃
PEEK	CuO	Reduced	-353.1	$3\text{CuO} + 2\text{Fe} = \text{Fe}_2\text{O}_3 + 3\text{Cu}$	Cu, Fe ₂ O ₃
			-212.7	$\text{CuO} + \text{H}_2\text{O} = \text{Cu(OH)}_2$	Cu(HO) ₂
Nylon 11	CuO	Reduced	-402.0	$6\text{CuO} + 2\text{Fe} = 3\text{Cu}_2\text{O} + \text{Fe}_2\text{O}_3$	Cu, Cu ₂ O
			-212.7	$\text{CuO} + \text{H}_2\text{O} = \text{Cu(OH)}_2$	Cu(HO) ₂ , Fe ₂ O ₃
Nylon 11	CuS	Reduced	-767.2	$\text{CuS} + \text{Fe} + 2\text{O}_2 = \text{FeSO}_4 + \text{Cu}$	Cu, Fe ₂ O ₃
PEEK	CuS	Reduced	-46.8	$\text{CuS} + \text{Fe} = \text{FeS} + \text{Cu}$	FeSO ₄
			-1141.6	$2\text{FeS} + 3.5\text{O}_2 = 2\text{SO}_2 + \text{Fe}_2\text{O}_3$	
Nylon 11	CuF ₂	Reduced	-168.6	$\text{CuF}_2 + \text{Fe} = \text{FeF}_2 + \text{Cu}$	Cu, FeF ₂ , Fe ₂ O ₃
Nylon 11	ZnS	Increased	+100.9	$\text{ZnS} + \text{Fe} = \text{FeS} + \text{Zn}$	FeO, Fe ₂ O ₃
			-272.0	$\text{Fe} + 0.5\text{O}_2 = \text{FeO}$	
Polyester	ZnO	Increased	+219.3	$3\text{ZnO} + 2\text{Fe} = \text{Fe}_2\text{O}_3 + 3\text{Zn}$	Fe ₂ O ₃
Polyester	CaF ₂	Increased	+507.0	$\text{CaF}_2 + \text{Fe} = \text{FeF}_2 + \text{Ca}$	Fe ₂ O ₃

Table 6. Nano-mechanical properties obtained for polystyrene and polystyrene/clay nanocomposite micro-beams using the normal beam bending test (adapted from Ref. 179).

Micro-Beam Materials	Elastic Modulus, MPa	Hardness, MPa	Yield Strength, MPa	Breaking Strength, MPa
Polystyrene	1900	290	66	271
Polystyrene/clay	4600	390	95	128

Table 7. Scratch hardness and elastic modulus data for some selectively chosen polymer composite systems.

Materials	Elastic Modulus, GPa	Scratch Hardness, MPa	Reference
Neat polyamide 6, A0	2.45	45	
Polyamide 6/organoclay, A1	4.53	98	345
Polyamide 6/organoclay, A1	4.12	47	
Neat polypropylene homopolymer	1.73	55.8	
Polypropylene homopolymer/talc (80/20)	2.73	59.4	320
Polypropylene copolymer	1.07	27.4	
Polypropylene copolymer/talc (80/20)	1.55	29.6	
Neat polyethylene	0.61	20.1	
Polyethylene/organoclay (98/2)	0.77	22.0	322
Polyethylene/organoclay (96/4)	0.92	33.4	
Neat polypropylene	1.50	88.2	
Polypropylene/wollastonite (80/20)	2.28	186.3	321
Polypropylene/talc (80/20)	2.01	78.4	

Table 8. Variation of nanoscratch penetration depth with normal loads for Si(100), porous silicon, PPV- and MEHPPV-filled porous silicon (adapted from Ref. 362).

Sample	Normal Load (μN)				Elastic Modulus, GPa	Hardness, GPa	Fracture Toughness, $\text{MPa m}^{1/2}$
	20	27	34	41			
	Nanoscratch Depth (nm)						
Si(100)	3.2 ± 0.3	5.5 ± 0.3	9.1 ± 0.4	12.0 ± 0.3	142.5 ± 2.4	12.14 ± 0.23	0.61 ± 0.02
Porous Silicon	49.7 ± 1.6	61.3 ± 1.1	64.6 ± 1.4	74.0 ± 1.2	20.65 ± 0.5	1.57 ± 0.07	1.92 ± 0.04
PPV-filled	35.5 ± 2.8	42.3 ± 2.1	44.4 ± 4.3	47.9 ± 3.8	1.55 ± 0.1	0.05 ± 0.01	3.2 ± 0.3
MEHPPV-filled	37.9 ± 2.8	42.9 ± 2.1	50.0 ± 3.0	56.5 ± 2.6	9.20 ± 0.4	0.15 ± 0.01	4.14 ± 0.2

Table 9. Correlation of % crystallinity, elastic modulus and yield strength data for polypropylene- and polyethylene-based systems with their respective average scratch residual depths (adapted from Ref. 365-367).

Materials	Crystallinity, % (Ref. 366, 367)	Elastic Modulus, MPa (Ref. 365)	Yield Strength, MPa (Ref. 365)	Average Residual Scratch Depth*, nm (Ref. 365)
Neat polypropylene	46	1450	33	112
Polypropylene with 4 wt% of clay	46	1825	38	93
Neat polyethylene	40	235	24	156
Polyethylene with 4 wt% of clay	56	494	29	130

* at 1 mN load

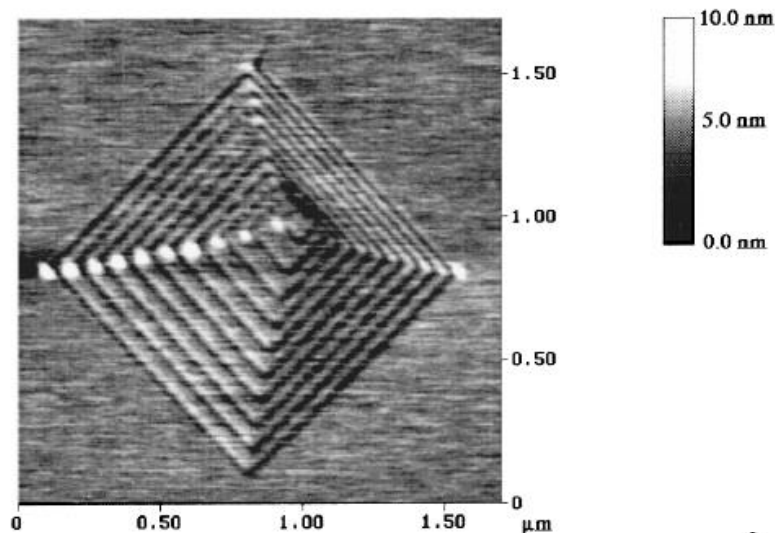


Figure 1. Trim pattern generated by scratching a Si(100) surface using an AFM with a three-sided pyramidal single-crystal natural diamond tip having an apex angle of 80° and a radius of about 100 nm mounted on a stainless steel cantilever beam with normal stiffness of about 25 N/m. A normal load of 15 μN and writing speed $\sim 0.5 \mu\text{m/s}$ were used (reprinted with permission from Ref. 1; Copyright (2001) Elsevier).

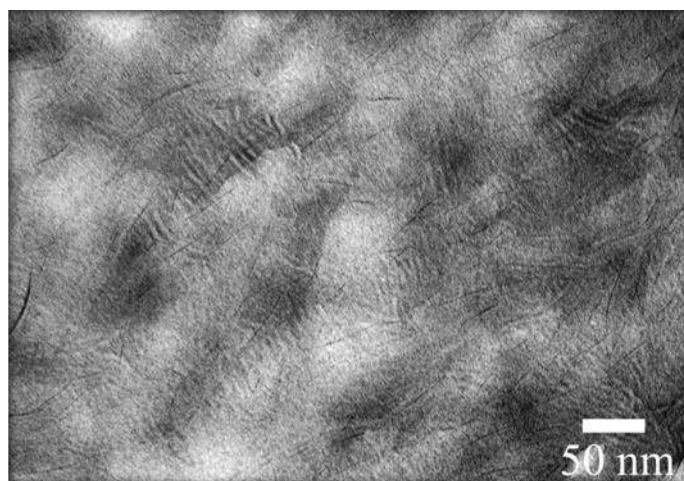


Figure 2. TEM micrograph taken in the core region of injection-molded polyamide 6/organoclay nanocomposite (90/10) along a plane normal to the flow direction showing the preferential organization of lamellae in the vicinity of clay layers (reprinted with permission from Ref. 10; Copyright (2008) American Chemical Society).

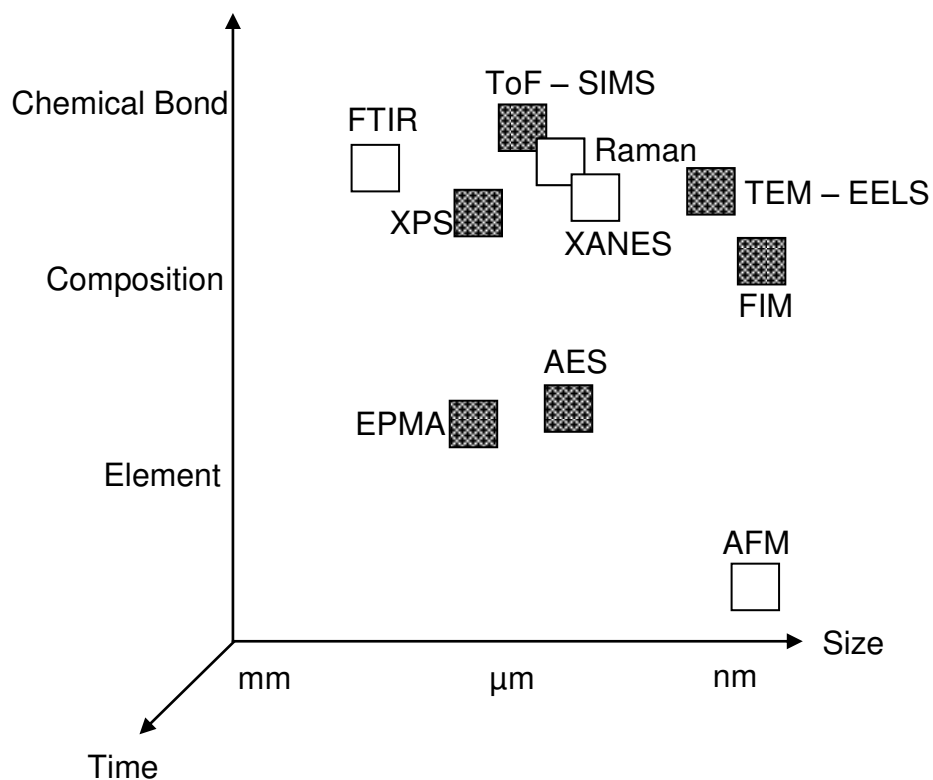


Figure 3. Schematic illustration of the resolution of surface analytical tools as viewed from time, size, and resolving power (solid squares require high vacuum, while open squares can be used in air) (adapted from Ref. 42).

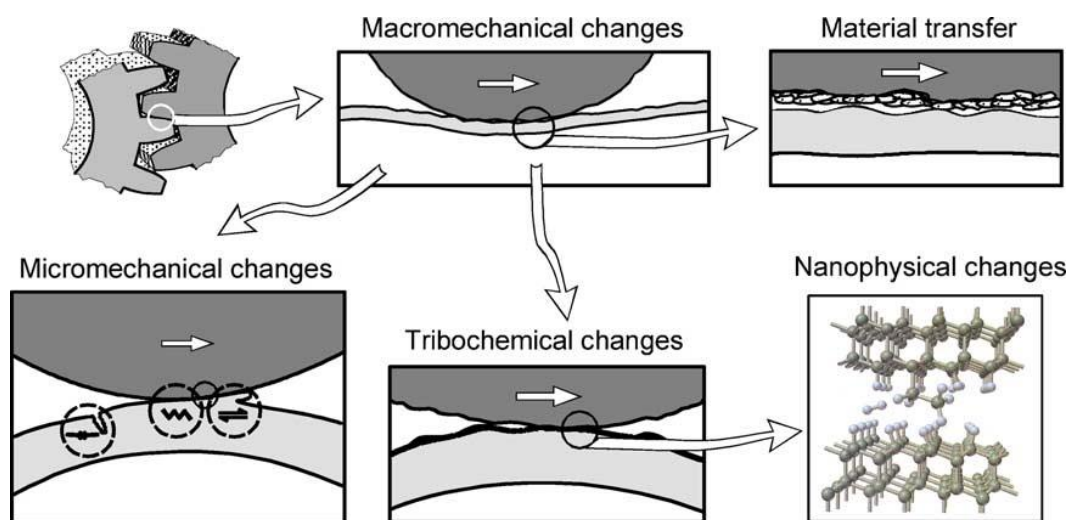


Figure 4. Schematics of tribological contact mechanisms: macromechanical changes, material transfer, micromechanical, tribochemical and nanophysical changes in the contact (reprinted with permission from Ref. 69; Copyright (2005) Elsevier).

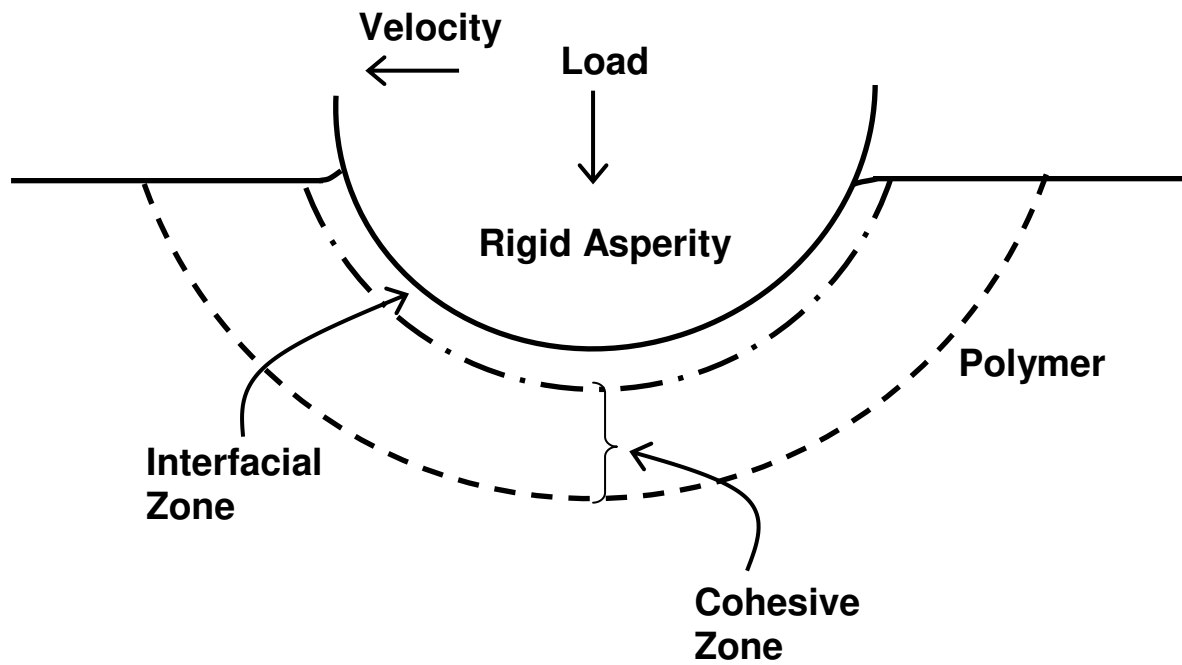
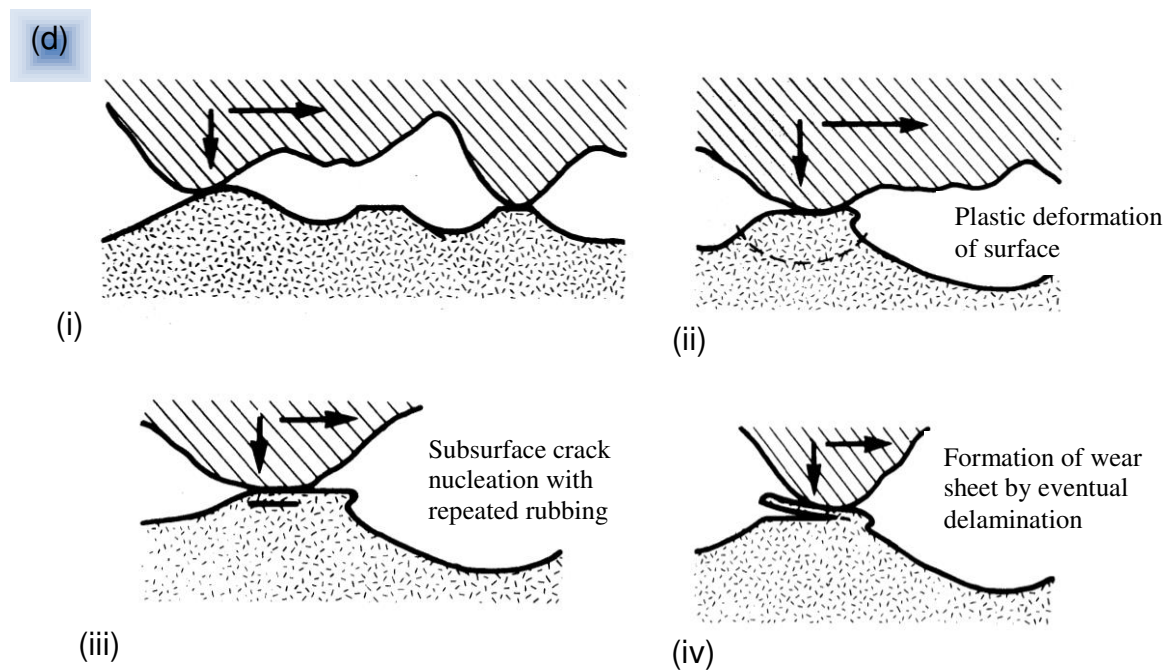
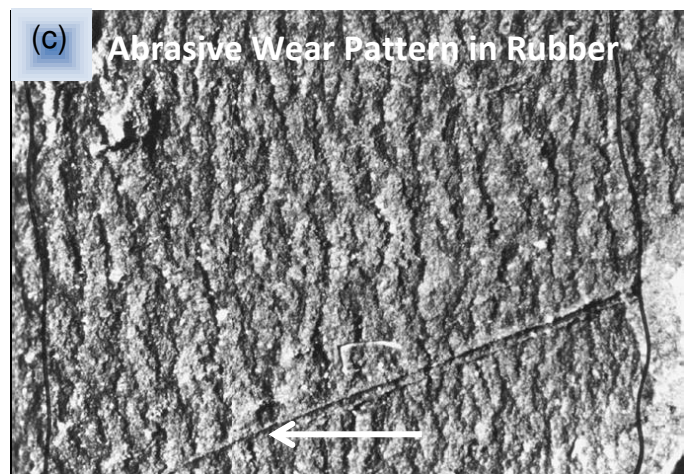


Figure 5. Schematic representation of the grouping of different wear mechanisms under cohesive wear and interfacial wear processes (adapted from Ref. 45).



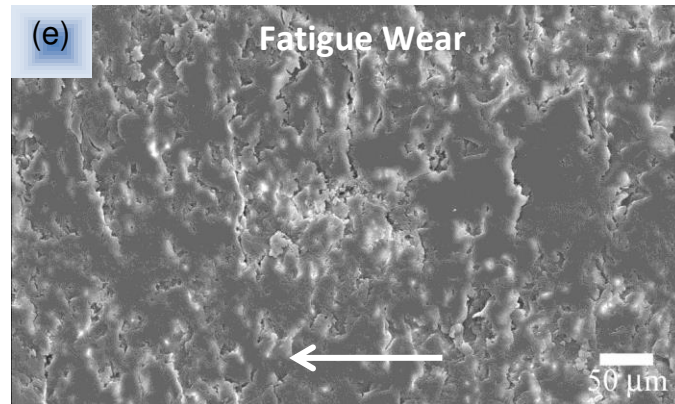


Figure 6. (a-c, e) Typical appearances of the most common wear patterns: (a) adhesive wear damage (from Ref. 72); (b) abrasive mode of wear damage (reprinted with permission from Ref. 75; Copyright (2005) Elsevier); (c) abrasive wear pattern in rubber (reprinted with permission from Ref. 78; Copyright (2001) CRC Press); (e) fatigue wear (from Ref. 72); (d) Schematic of the various stages involved in the formation of delaminated wear sheets (adapted from Ref. 61). The black arrows in (a) point to the adhesive patched formed on the surface of the worn track; while white arrows in (a-c, e) indicate the direction of rotation of the polymer block with respect to the slider.

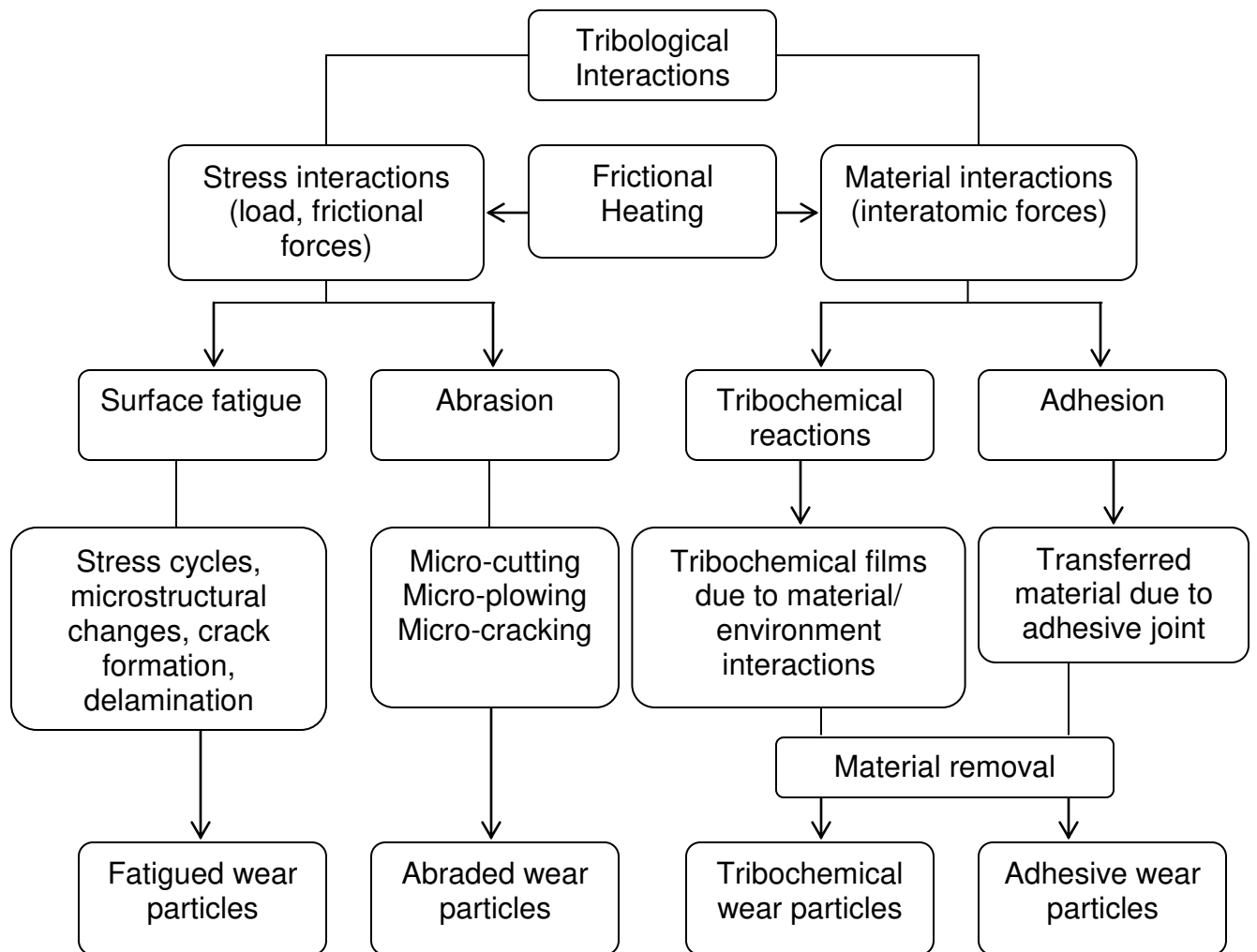


Figure 7. Basic tribological interactions leading to wear particle generation (adapted from Ref. 59).

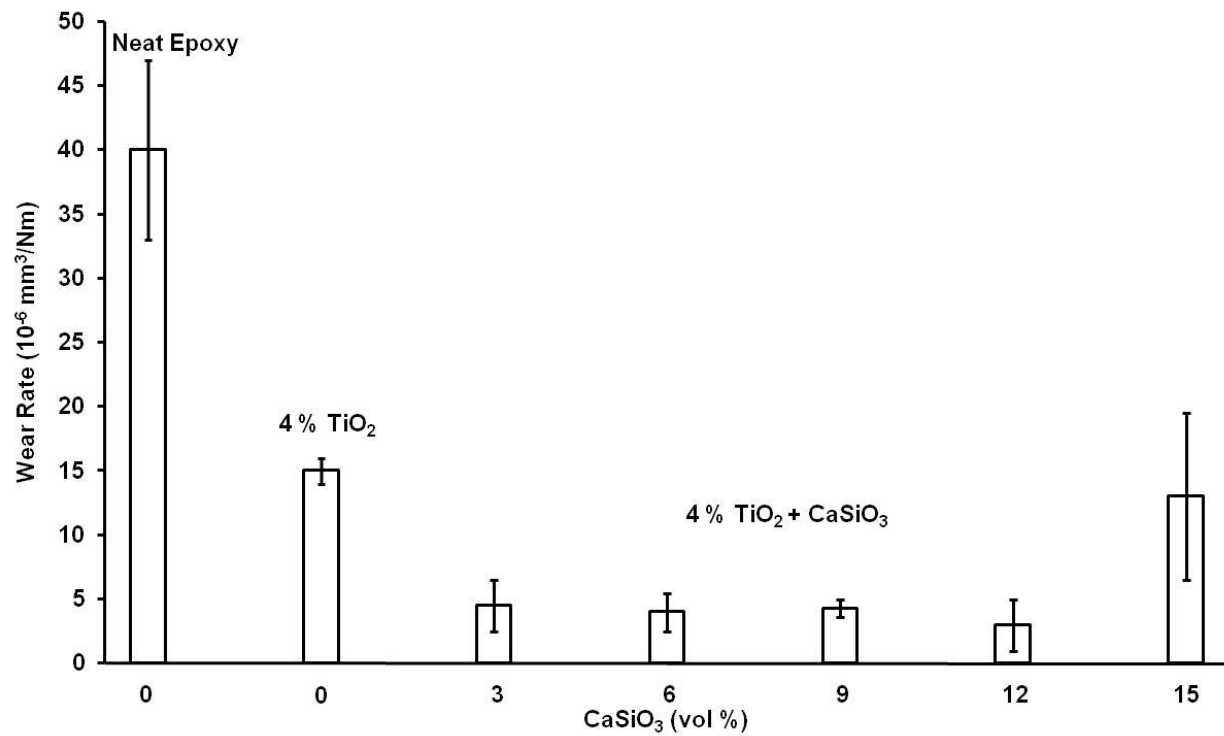


Figure 8. Specific wear rates of neat epoxy and epoxy with 4 vol % TiO_2 composites at varying content of CaSiO_3 (adapted from Ref. 95).

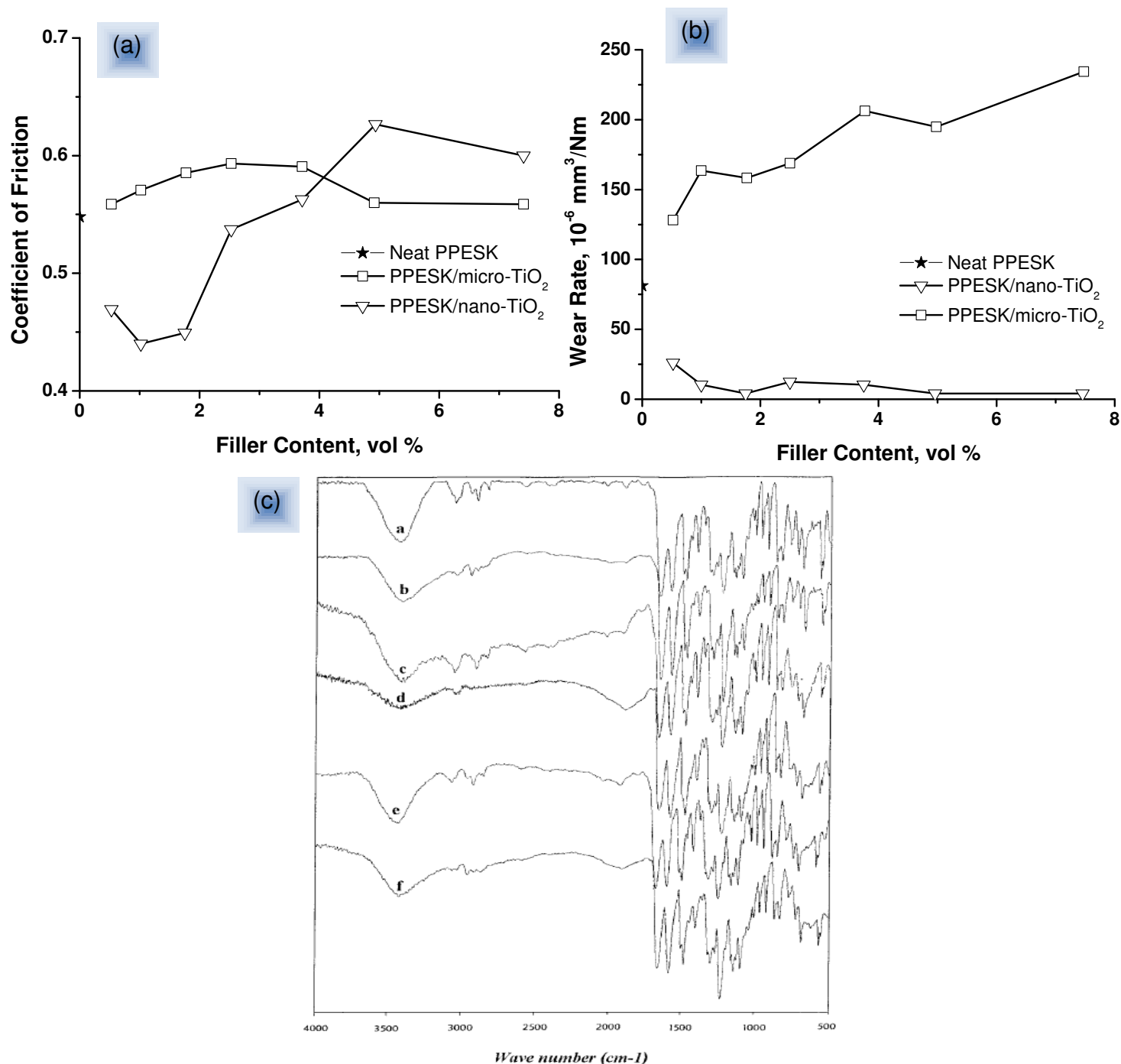


Figure 9. Variation of (a) coefficient of friction and (b) wear rate of nano- and micro-TiO₂ reinforced PPESK with different filler volume proportions (adapted from Ref. 98). (c) FTIR spectra of PPESK composites and their corresponding wear debris - *a* unfilled PPESK; *b* debris of *a*; *c* 7.5 vol % micrometer TiO₂ filled PPESK; *d* debris of *c*; *e* 7.5 vol % nanometer TiO₂ filled PPESK; *f* debris of *e* (reprinted with permission from Ref. 98; Copyright (2004) Wiley InterScience).

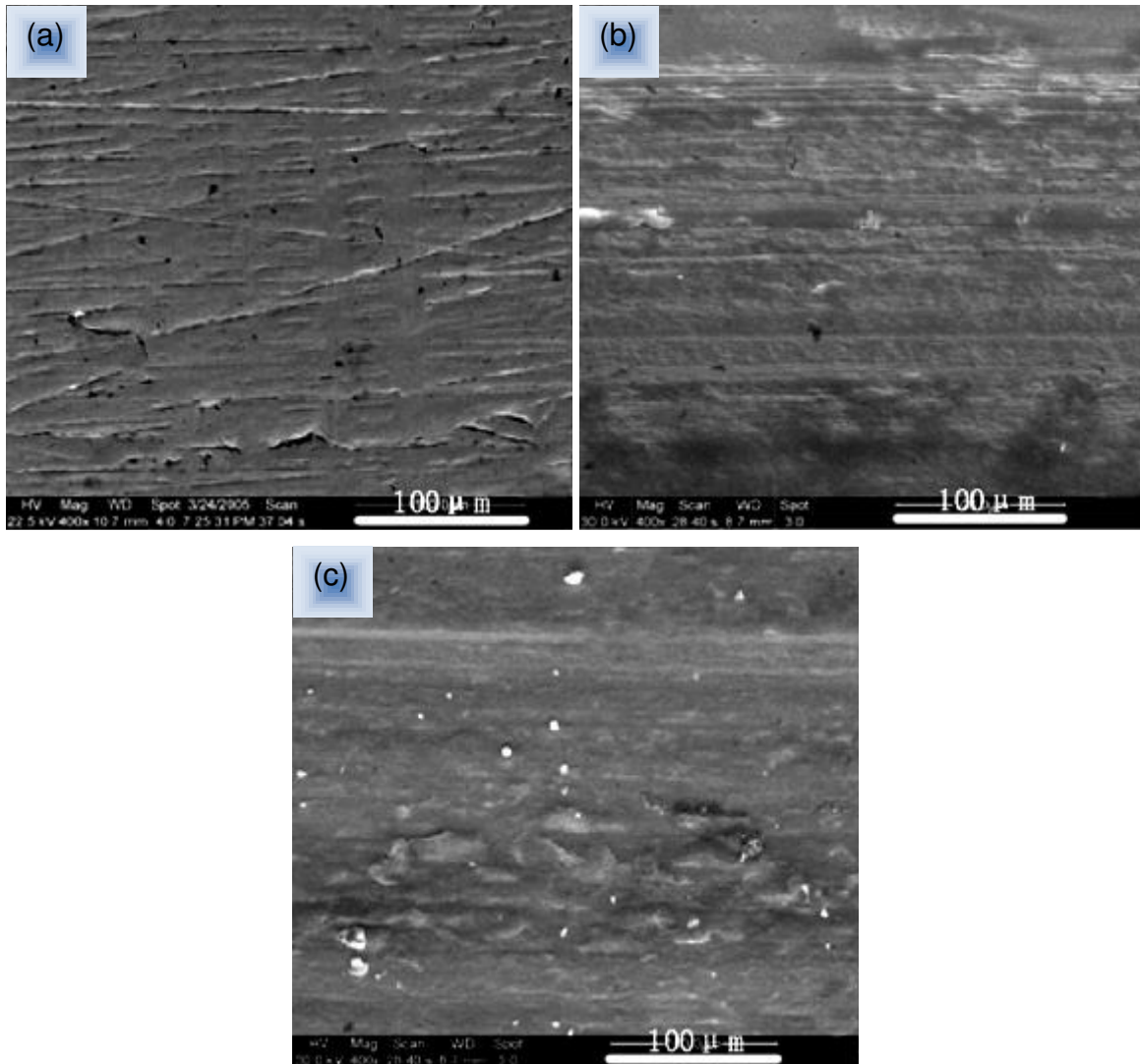


Figure 10. SEM micrographs of transfer films in (a) PTFE, (b) 17wt % TiO_2 particles filled PTFE, and (c) 17 wt % TiO_2 whiskers filled PTFE (sliding conditions: load ~ 200 N; sliding velocity ~ 1.39 m/s; time ~ 30 min; sliding distance ~ 2.5 km; against a steel ring) (reprinted with permission from Ref. 102; Copyright (2007) Elsevier).

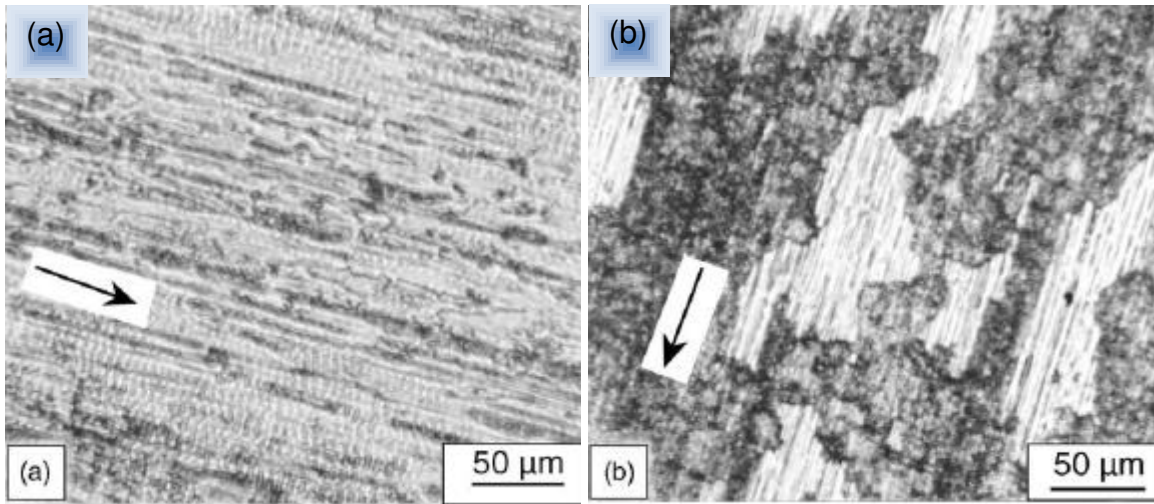


Figure 11. Optical micrographs of transfer films formed during sliding on steel counterface for PPS filled with (a) 2 vol % TiO_2 and (b) 5 vol % TiO_2 . Arrow shows sliding direction (reprinted with permission from Ref. 41; Copyright (2005) Elsevier).

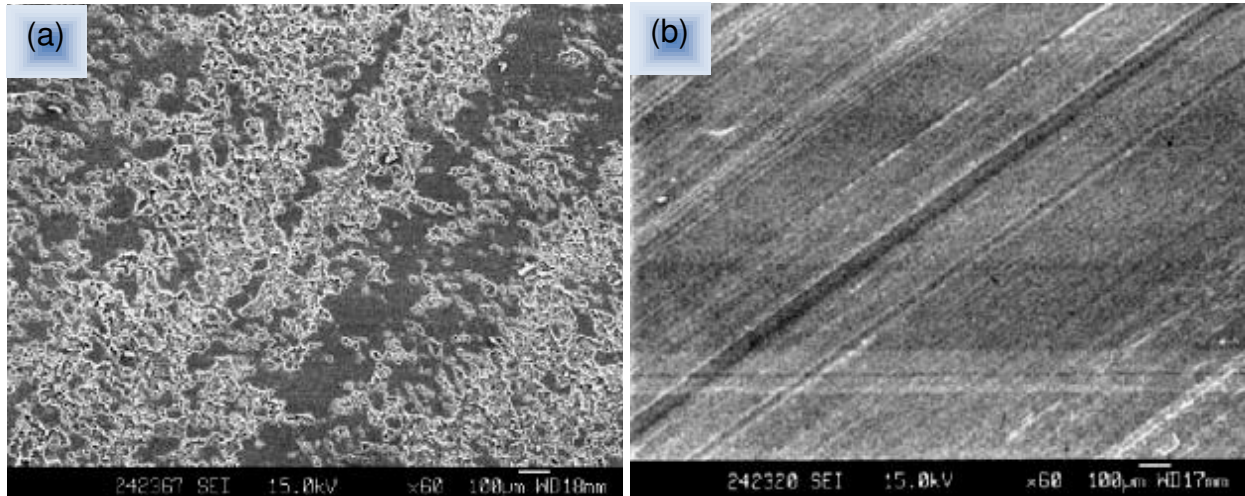


Figure 12. SEM micrographs of the worn surfaces of (a) epoxy and (b) nano- Si_3N_4 /epoxy composite (0.83 vol %) showing the differences in the wear damage when slid against a steel disk for 3 h at a sliding velocity of 0.4 m/s and pressure of 3 MPa (reprinted with permission from Ref. 107; Copyright (2003) Elsevier).

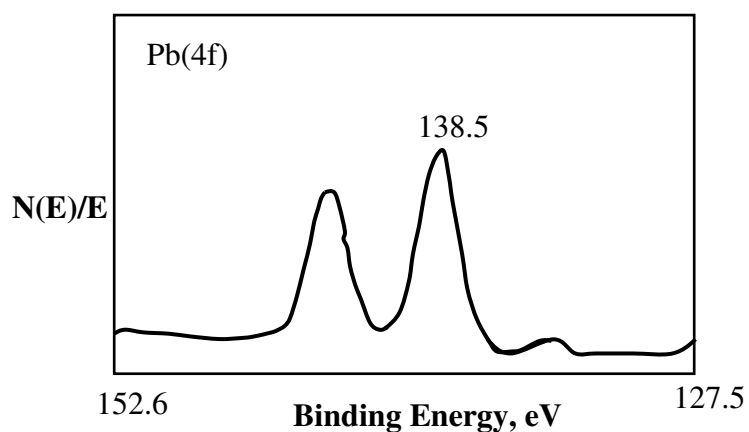


Figure 13. Pb(4f) x-ray photoelectron spectra of transfer film of 35 % PbS-nylon composite formed on a steel surface after sliding wear test (adapted from Ref. 116).

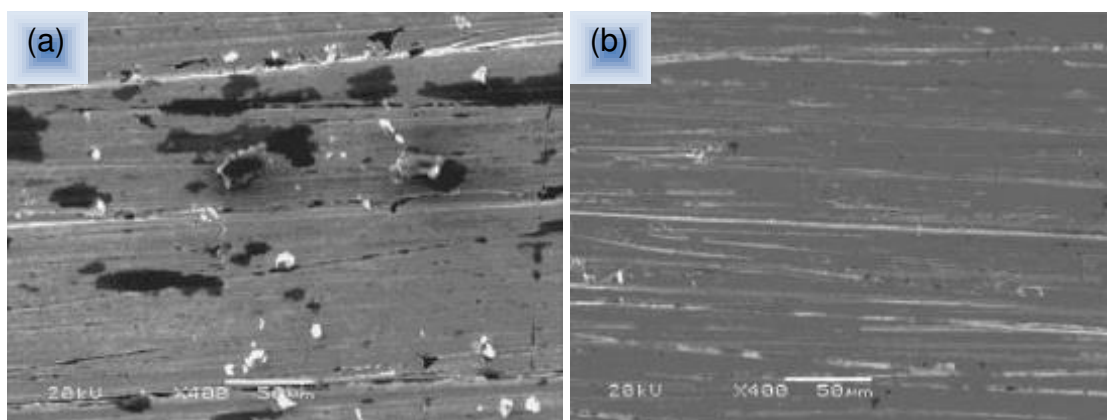


Figure 14. SEM micrographs of transfer films formed on the steel ring surface in *a* neat polyimide and *b* polyimide/CNT nanocomposite with 8 wt % of CNT (sliding conditions: load ~200 N; velocity ~0.431 m/s; test duration ~90 min) (reprinted with permission from Ref. 127; Copyright (2004) Elsevier).

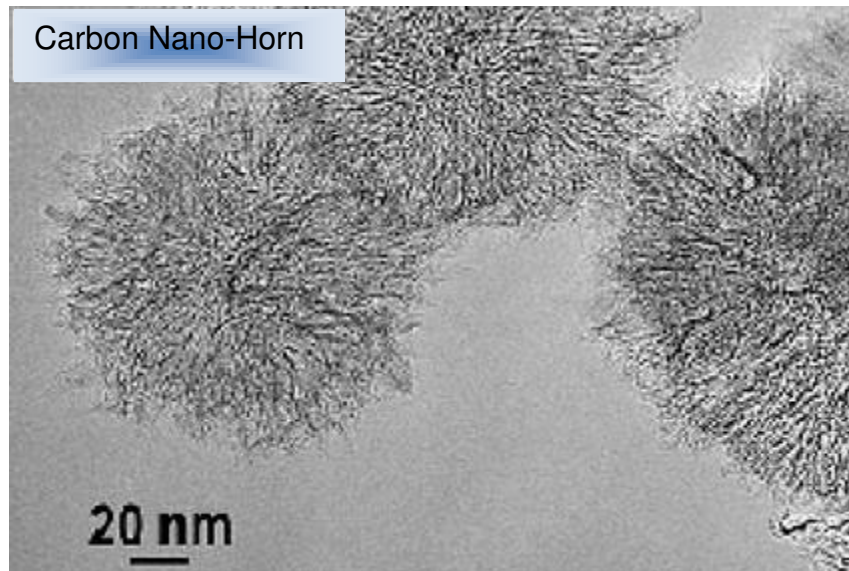
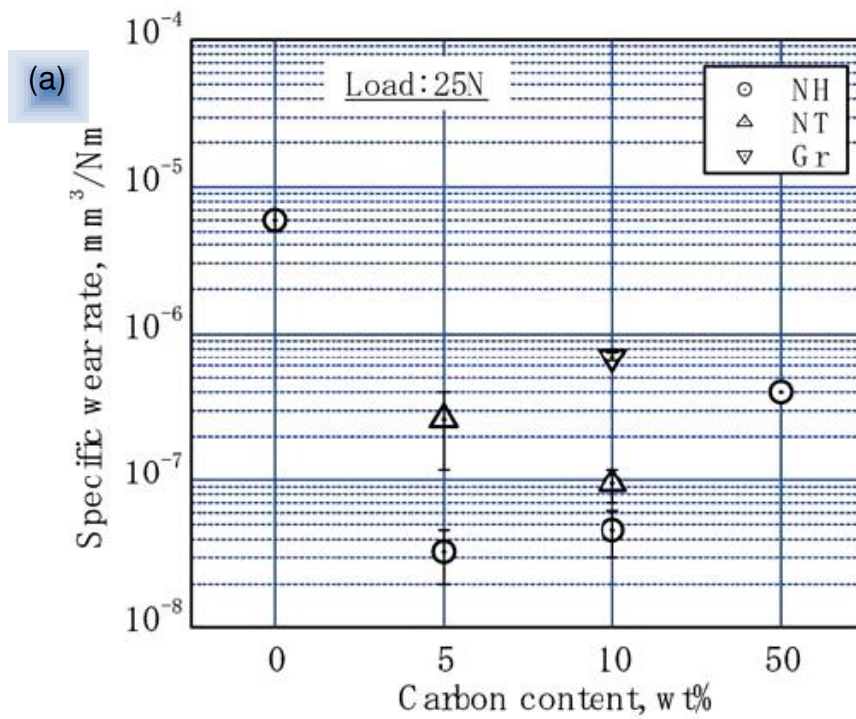


Figure 15. TEM micrograph showing the spherical single wall carbon nanohorn (SWNH) particle (reprinted with permission from Ref. 128; Copyright (2005) Springer).



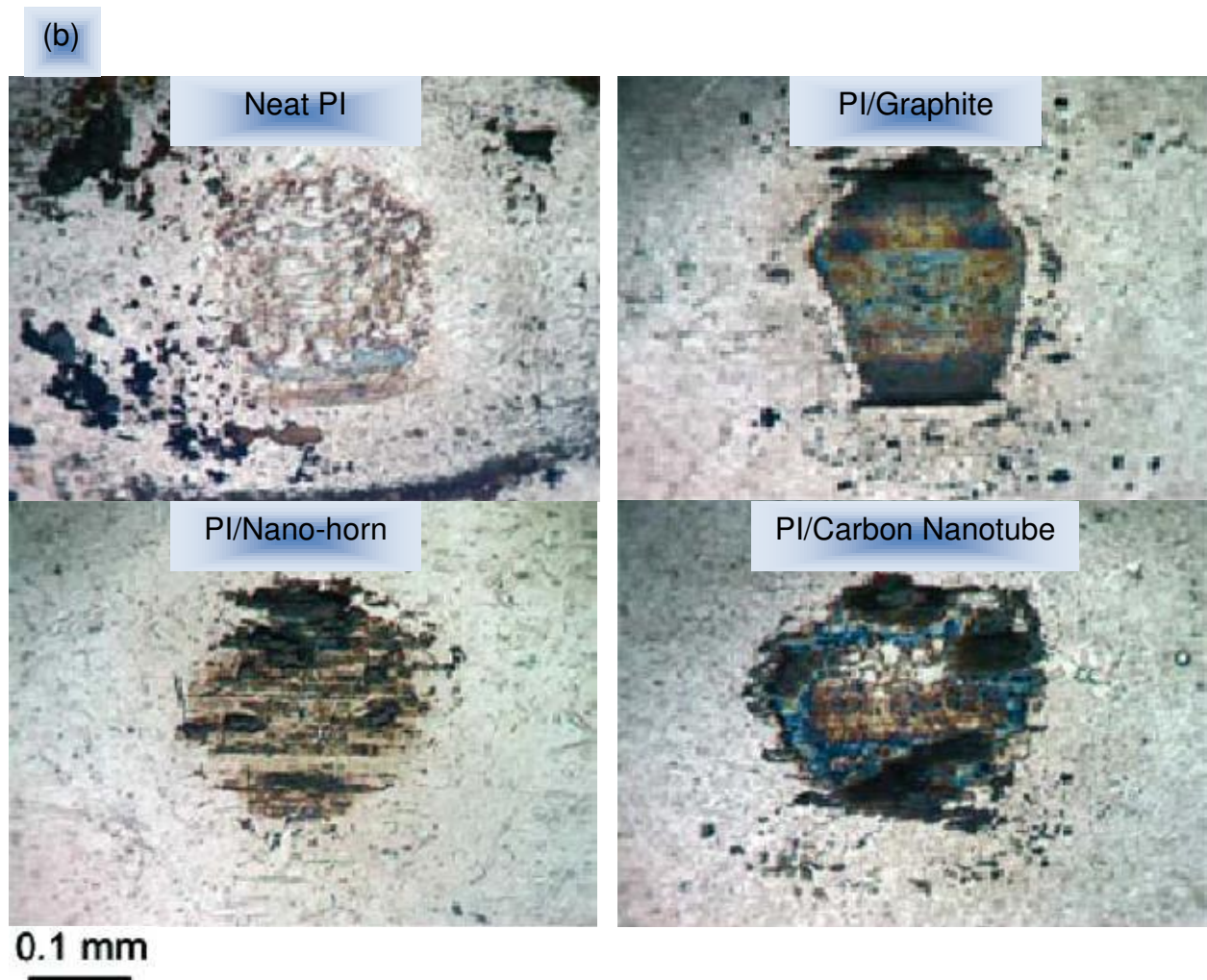


Figure 16. (a) Specific wear rates of neat PI along with PI nanocomposites at a load of 25 N; (b) optical photographs of the slider surfaces after sliding against composites with different carbon fillers (10 wt %) at a load of 25 N (reprinted with permission from Ref. 128; Copyright (2005) Springer).

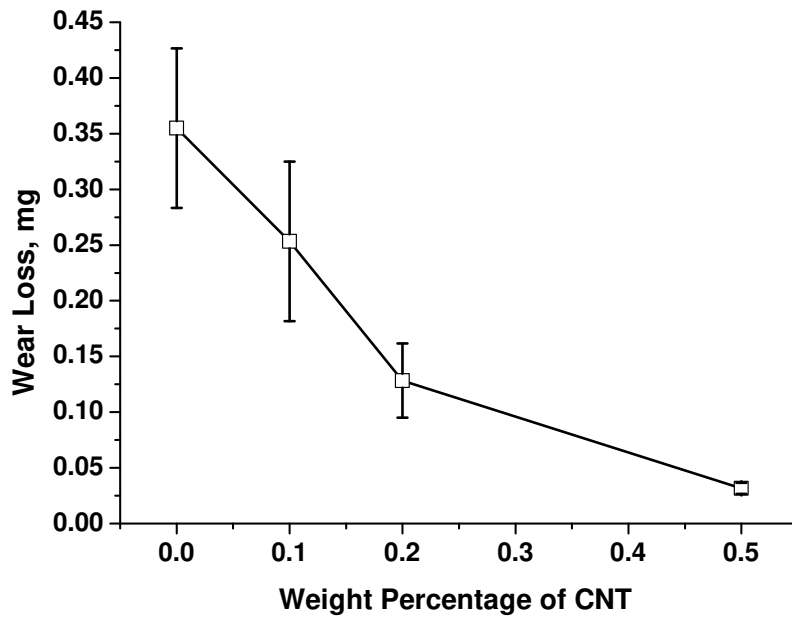


Figure 17. Variations of weight loss as a function of CNT content in UHMWPE (adapted from Ref. 133).

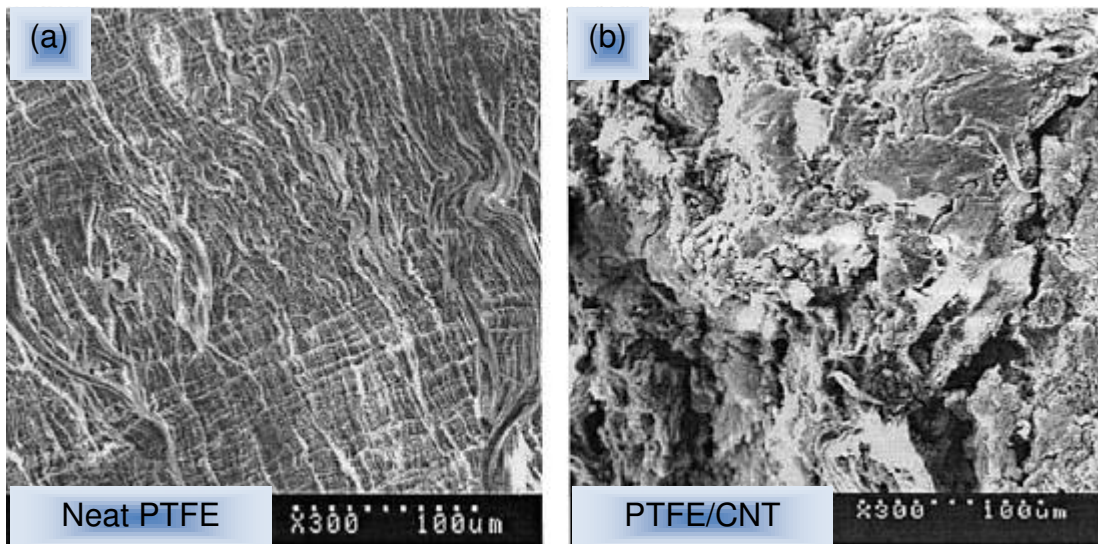


Figure 18. SEM micrographs of worn surfaces (slid against stainless steel counterface at a rate of ~200 rpm, normal load ~200 N, and test duration of 2 h) of *a* PTFE and *b* PTFE/CNT composite with 20 vol % CNTs showing the fibrous structure observed in neat PTFE being absent in PTFE/CNT composite (reprinted with permission from Ref. 122; Copyright (2003) Springer).

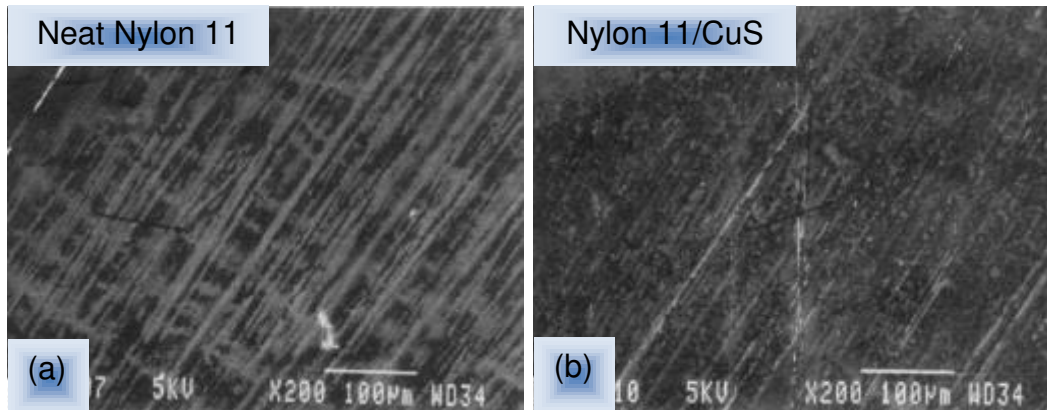


Figure 19. SEM micrographs showing the differences in quality of the transfer films formed on tool steel counterfaces in sliding for 2 h by (a) nylon 11 and (b) CuS/nylon composite (reprinted with permission from Ref. 137; Copyright (1993) Elsevier).

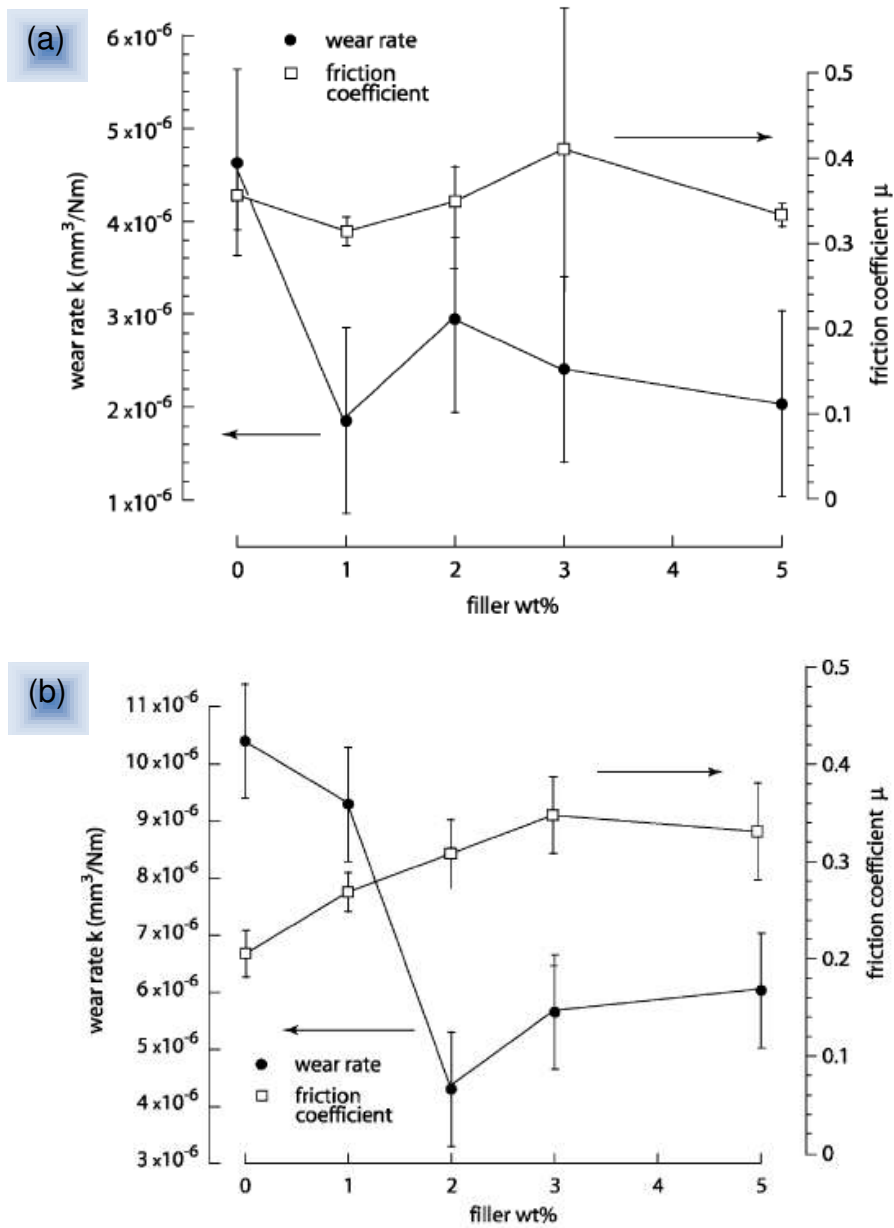


Figure 20. Effect of alumina nanoparticles on wear and friction of PET matrix of (a) 20±2% crystallinity and (b) 40±2% crystallinity (reprinted with permission from Ref. 142; Copyright (2005) Elsevier).

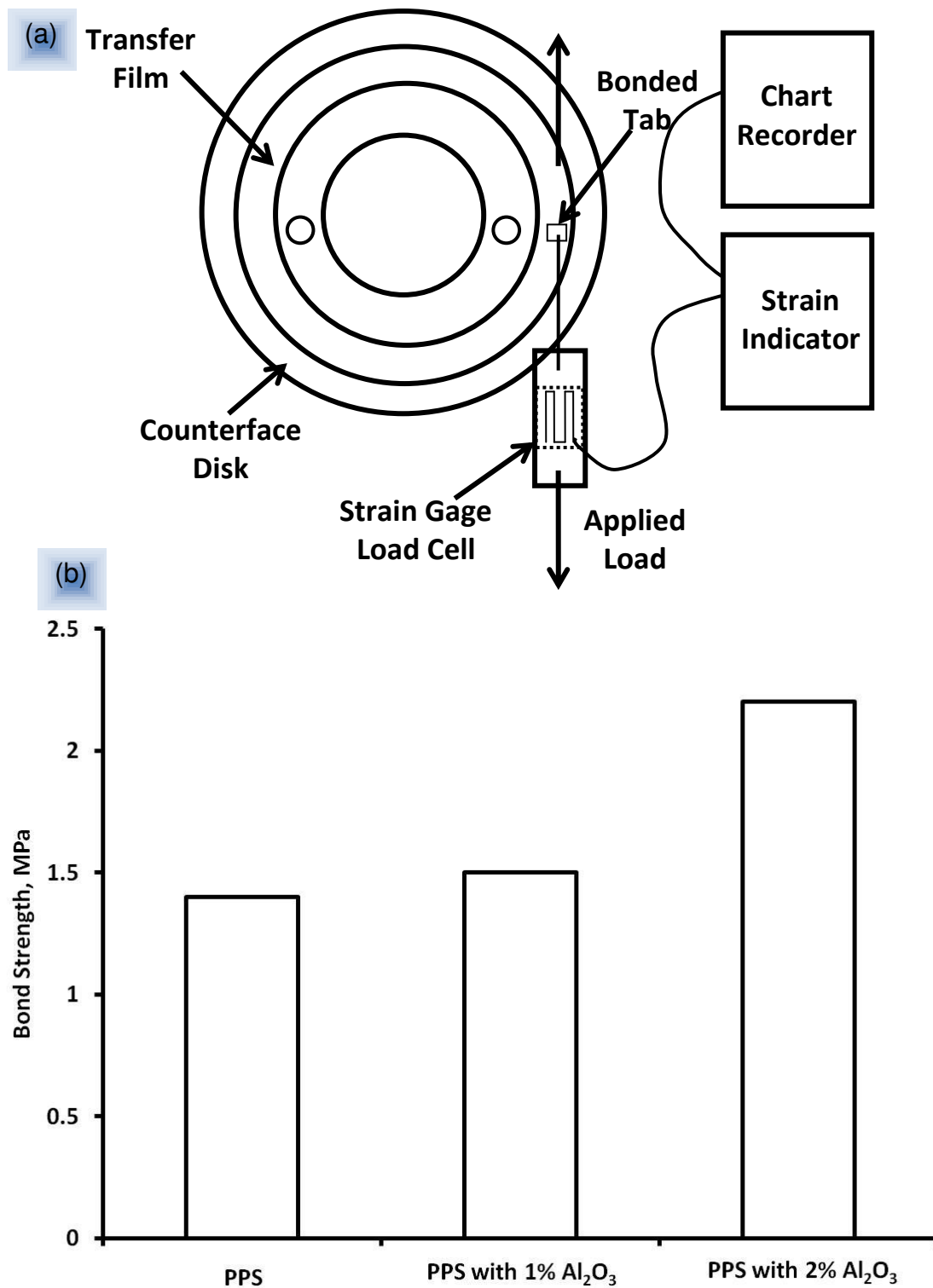


Figure 21. (a) Schematic of the apparatus used to test the transfer film bond strength to the counterface and (b) comparison of transfer film bond strength as a function of alumina content in PPS (adapted from Ref. 140).

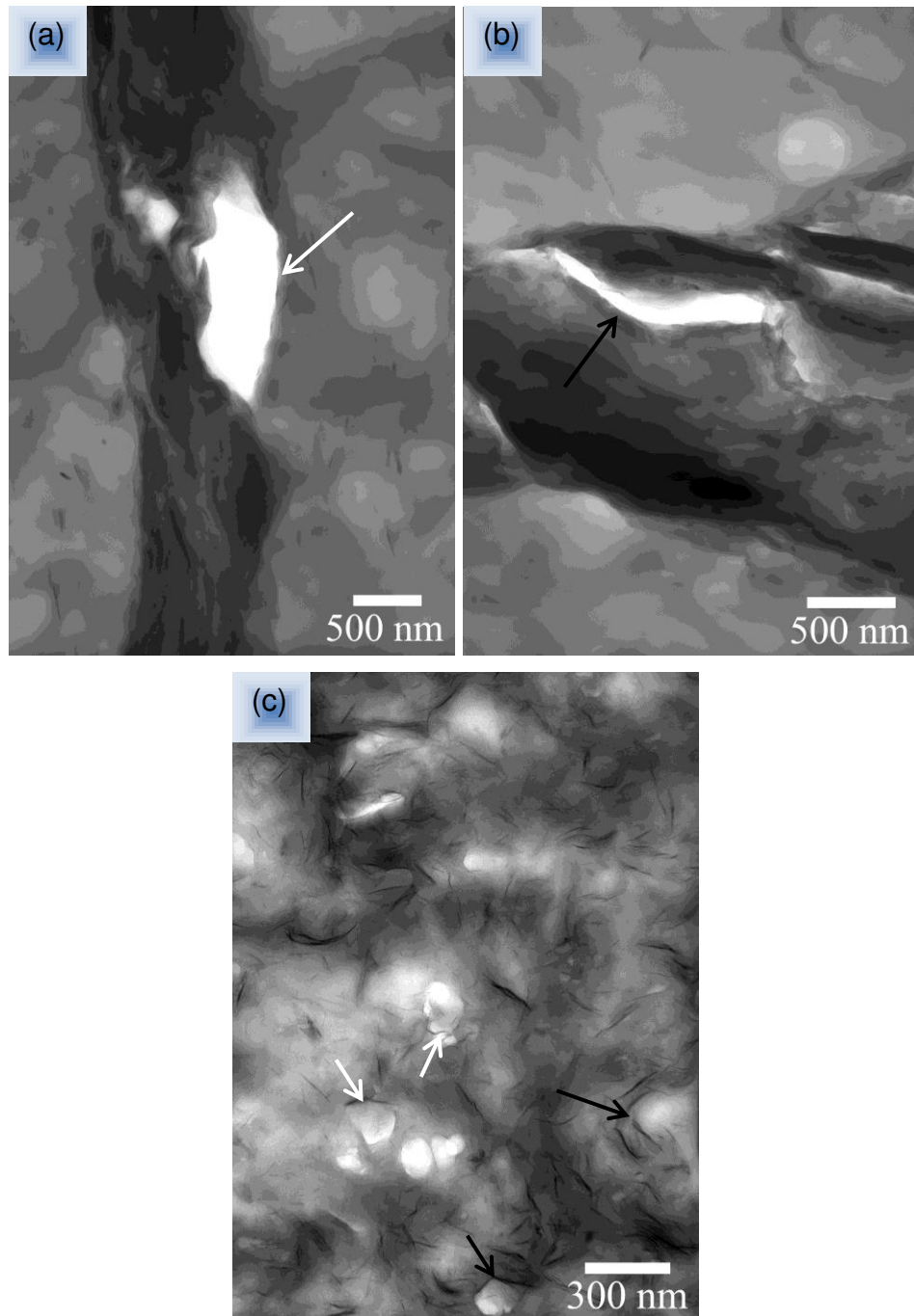


Figure 22. Subsurface cross-sectional TEM micrographs of wear tracks showing interlaminar delamination and interfacial debonding of clay layers in *a-b* poorly dispersed clay/nylon 6 nanocomposite and *c* finely dispersed clay/nylon 6 nanocomposite (Testing conditions: sliding speed ~ 0.08 m/s; normal load ~ 5 N; slider 6.3 mm Si_3N_4 ball). Black arrows indicate intra-gallery separation of clay layers and white arrows show debonding at clay-matrix interfaces (reprinted with permission from Ref. 75; Copyright (2005) Elsevier).

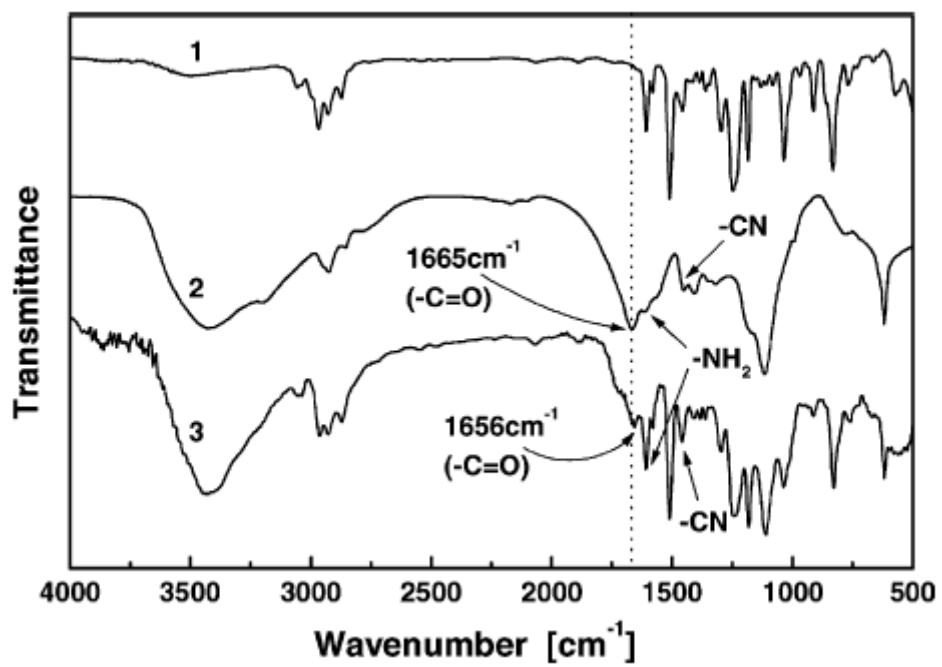


Figure 23. FTIR spectra (1) epoxy without any curing agent, (2) PAAM, and (3) cured blends of PAAM and epoxy (1/2 w/w) (reprinted with permission from Ref. 39; Copyright (2002) Elsevier).

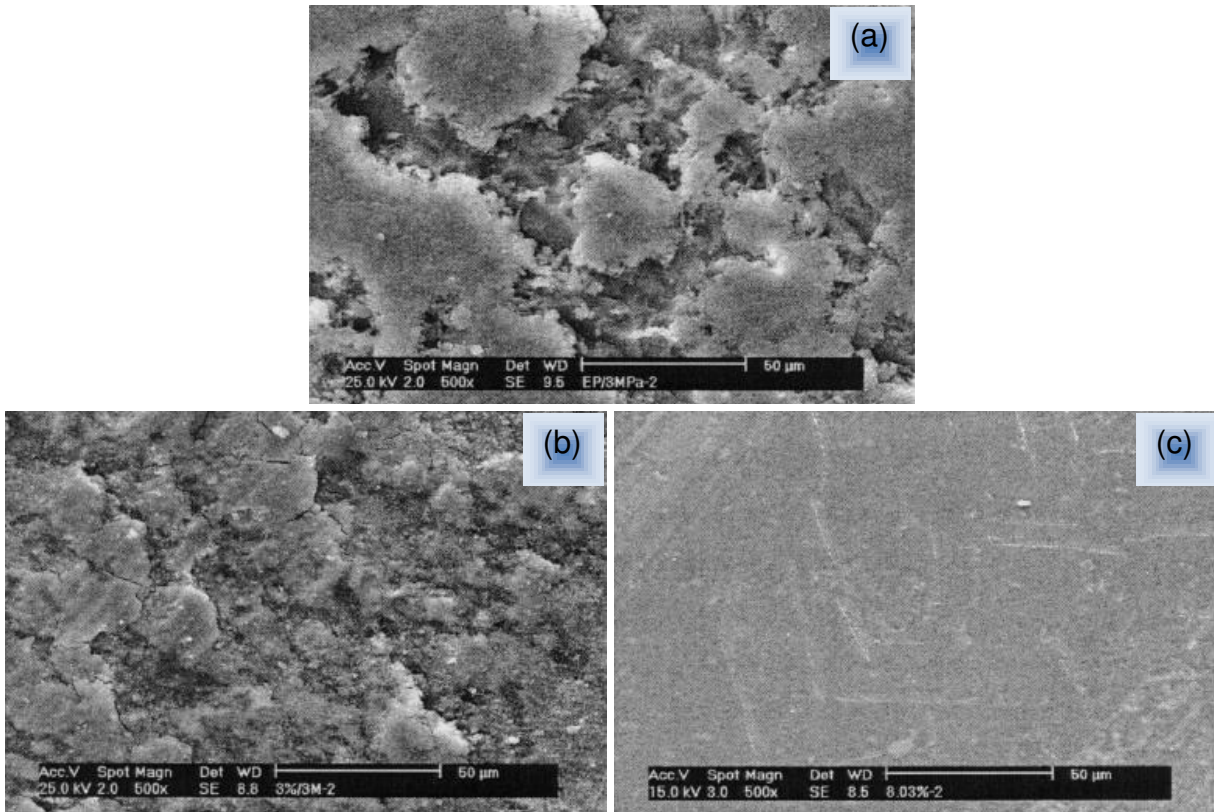


Figure 24. SEM micrographs of worn surfaces (slid against a steel ring under a pressure of 3 MPa, speed 0.4 m/s, and test period ~3 h) of (a) neat epoxy, (b) untreated nano-SiC/epoxy composite, and (c) SiC-g-PGMA/epoxy composite. Nano-SiC content is 1.2 vol % in all the filled systems (reprinted with permission from Ref. 154; Copyright (2005) Rapra Technology Limited).

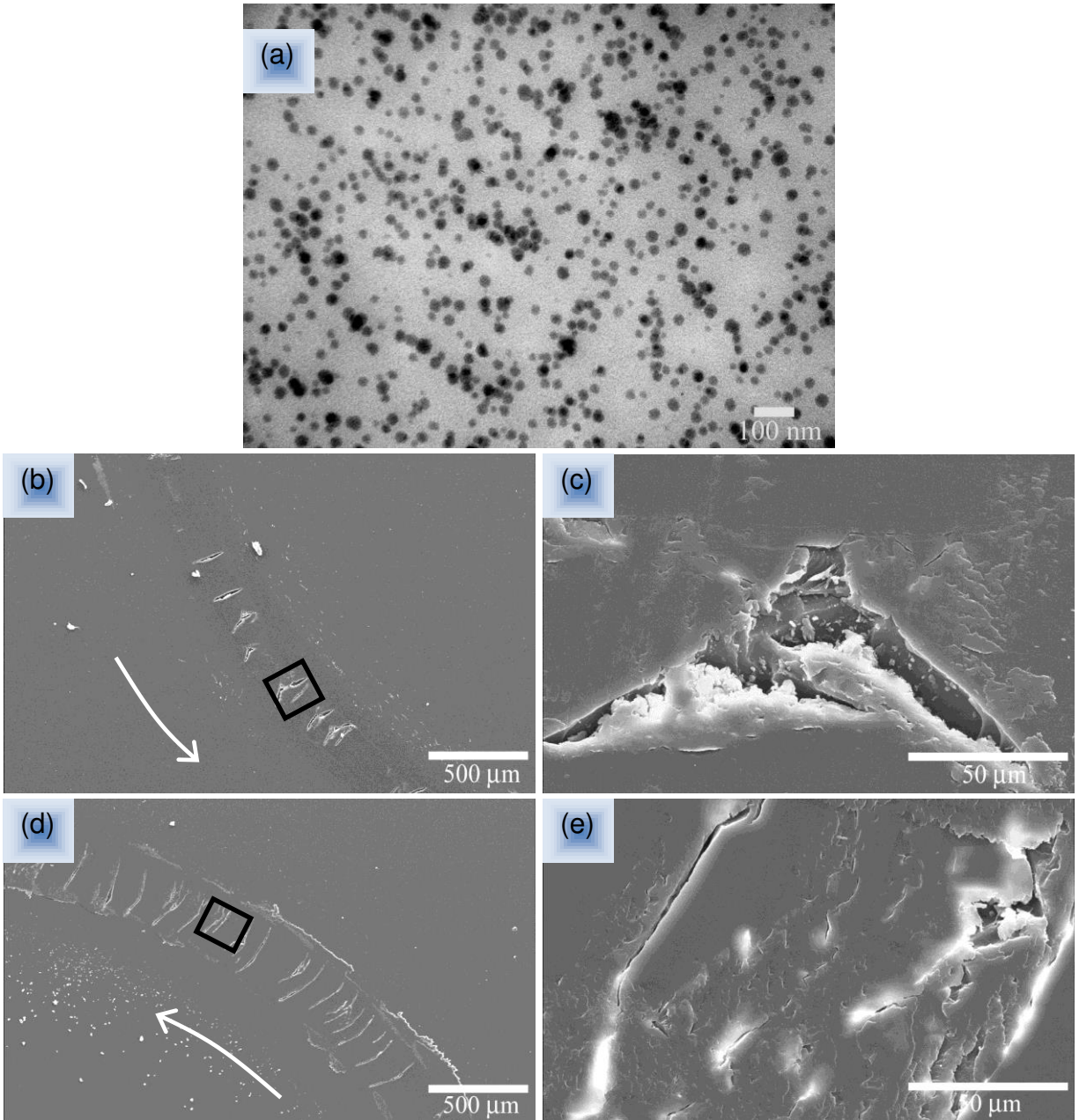


Figure 25. (a) TEM micrograph showing homogeneous dispersion of silica nanoparticles in epoxy matrix at 6 wt %; (b-f) SEM micrographs of worn surfaces of (b and c) neat epoxy and (d and e) silica/epoxy at 6 wt % silica slid against a silicon nitride ball at a sliding speed of 0.1 m/s, sliding distance of 500 m and load of 1 N. White arrows indicate the direction of rotation of the polymer block with respect to the slider; black squares identify the approximate locations where the corresponding high magnification micrographs are taken (from Ref. 72).

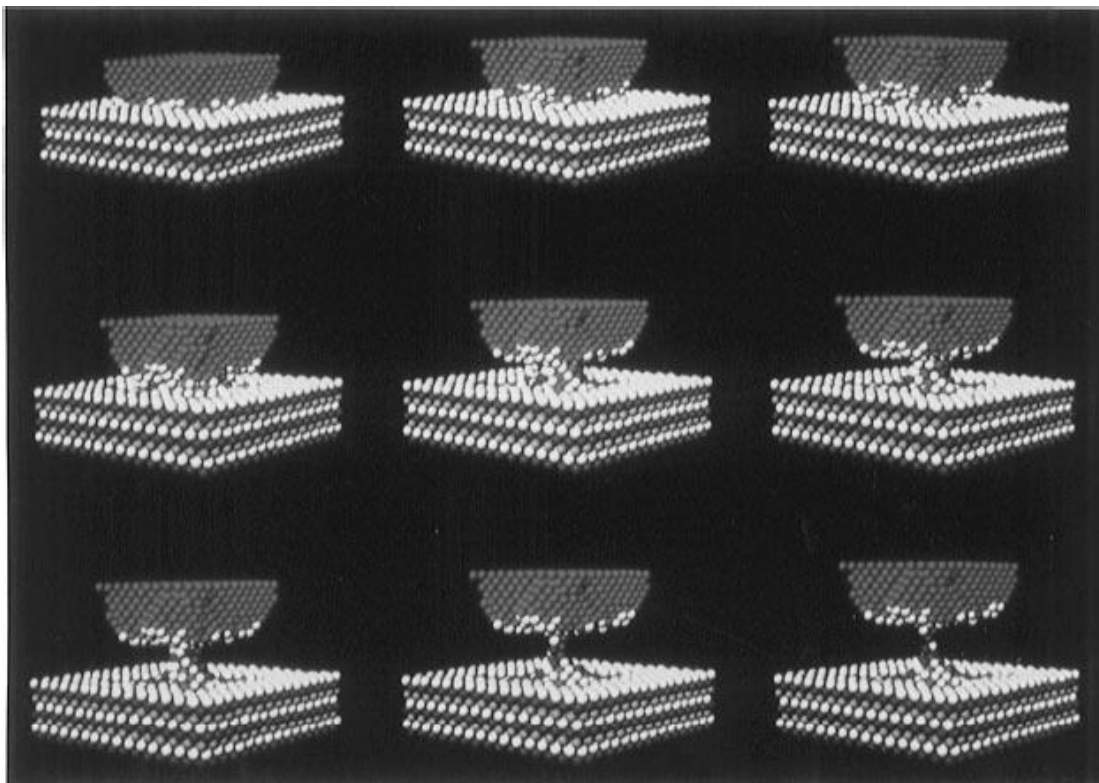


Figure 26. The sequence of atomic configurations starting from a Ni tip indented in a Au(001) substrate (top left) and during the process of retraction of the tip (from left to right) accompanied by formation of a connective solid gold junction, and culminating in a junction of atomic dimensions (bottom right). The MD simulations were performed at 300 K. Dark balls represent tip nickel atoms (reprinted with permission from Ref. 159; Copyright (1990) American Association for the Advancement of Science).

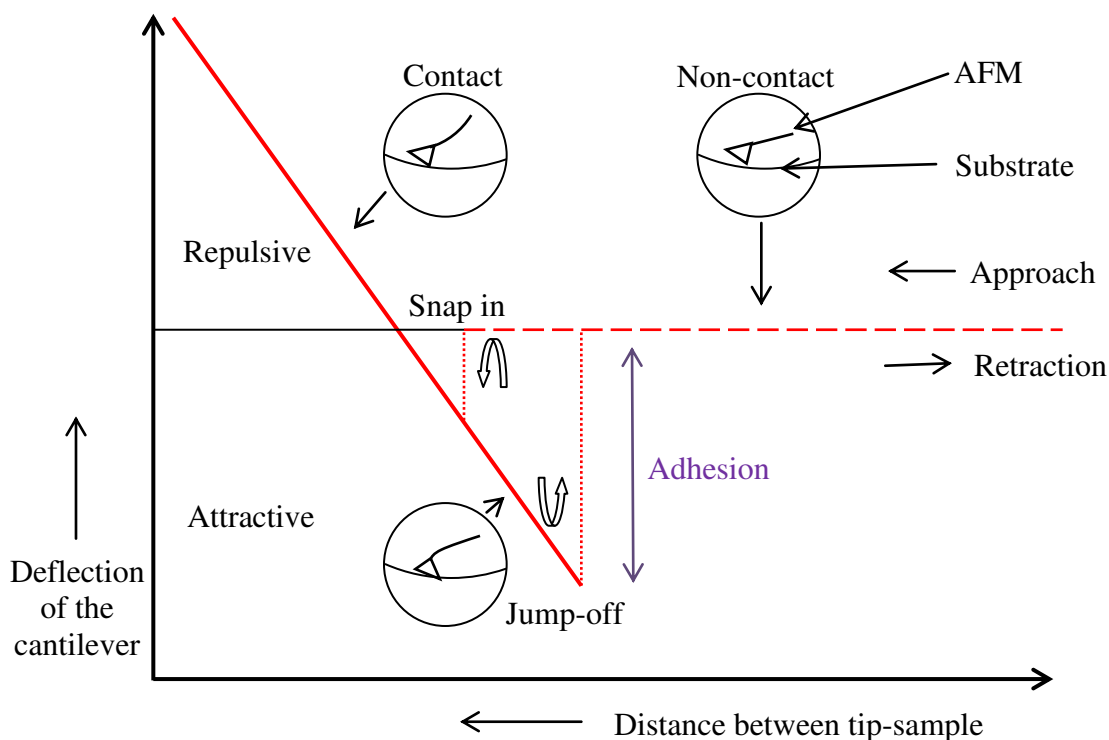


Figure 27. Schematic of a force contact curve generated by an AFM, that is, deflection of the cantilever is shown as a function of the tip-sample surface distance. In the beginning of the approach cycle, AFM tip is not in contact with the surface. As the tip is pushed into the surface, deflection of the cantilever occurs. In the retraction cycle as the tip is withdrawn from the surface, the tip adheres to the sample surface and, after the jump-off contact from the surface, the tip is brought to the non-contact position again. A variety of forces can be sensed between the AFM tip and surface depending on the interatomic distance, which include van der Waals, electrostatic, magnetic, capillary, or ionic repulsion forces (adapted from Ref. 181).

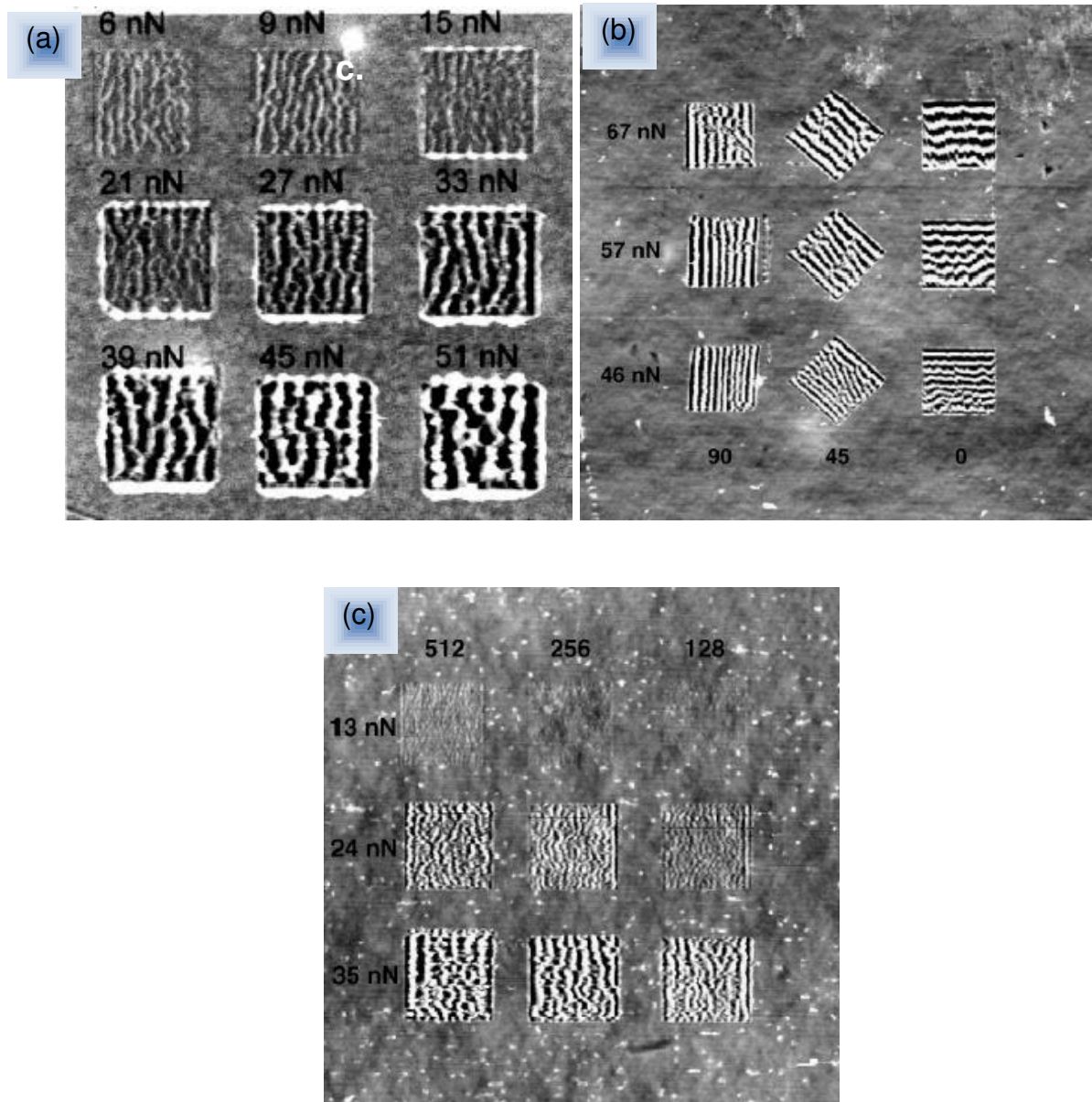


Figure 28. AFM topographic images after repeat scanning nine $1 \times 1 \mu\text{m}$ areas on (a) biaxially oriented PET film (field-of-view: $5.5 \times 5.5 \mu\text{m}$) showing the effect of applied load (reprinted with permission from Ref. 185; Copyright (2001) Elsevier); (b) uniaxially oriented PET film (field-of-view: $8 \times 8 \mu\text{m}$) showing the effect of scan angle and applied load (reprinted with permission from Ref. 184; Copyright (2004) Elsevier) and (c) uniaxially oriented PET film (field-of-view: 6×6

μm) showing the effect of scan line density at different applied loads (reprinted with permission from Ref. 184; Copyright (2004) Elsevier).

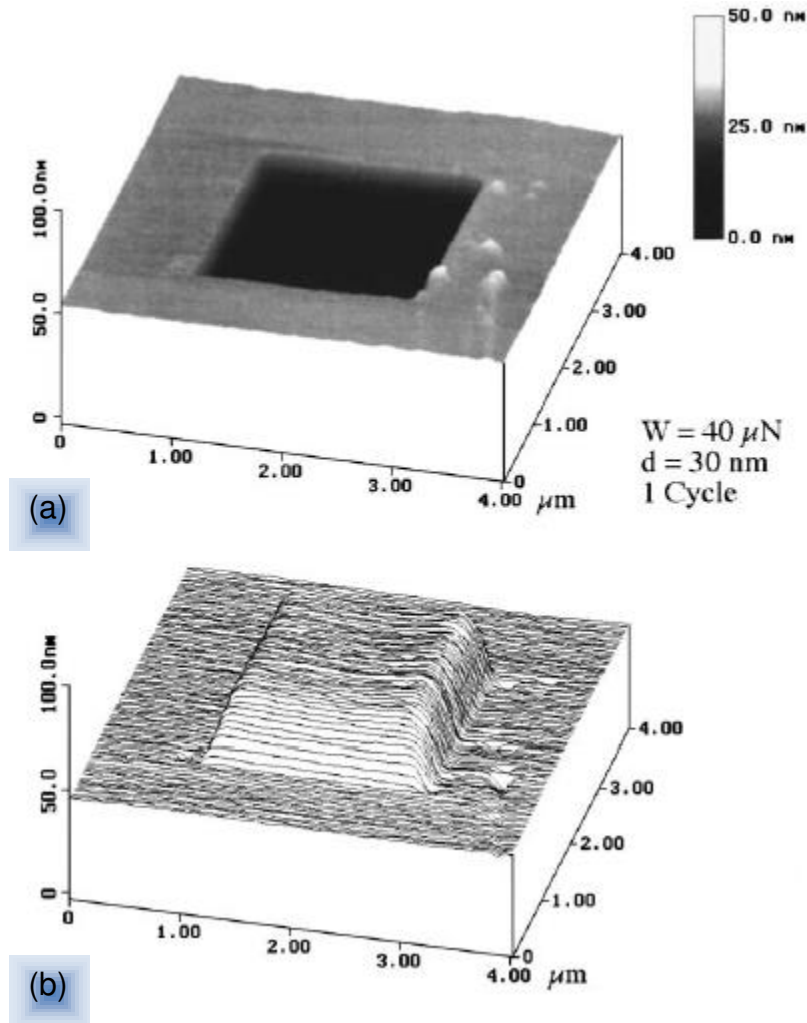


Figure 29. (a) Typical gray scale and (b) inverted AFM images of wear mark created using a diamond tip at a normal load of $40 \mu\text{N}$ and one scan cycle on Si (1 0 0) surface (reprinted with permission from Ref. 162; Copyright (1998) Elsevier).

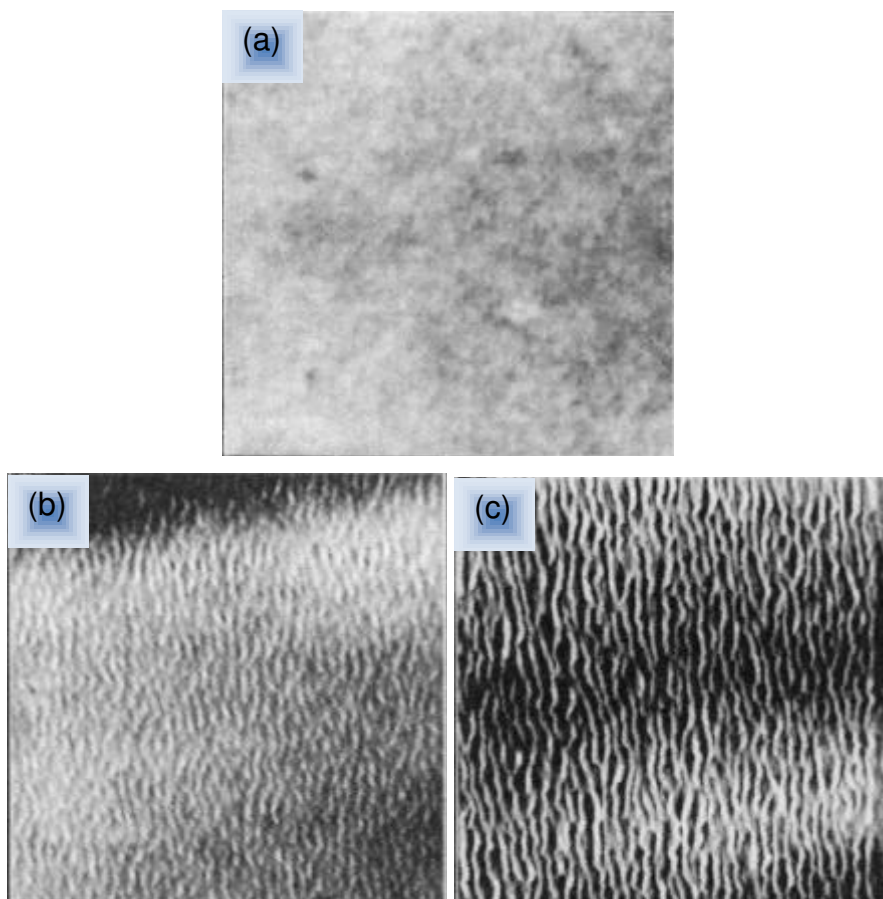


Figure 30. Time evolution of the polystyrene surface created by continuously scanning by an AFM: (a) initial surface; (b) for 2 minutes; and (c) for 5 minutes. Scanning direction is horizontal (reprinted with permission from Ref. 182; Copyright (1992) American Association for the Advancement of Science).

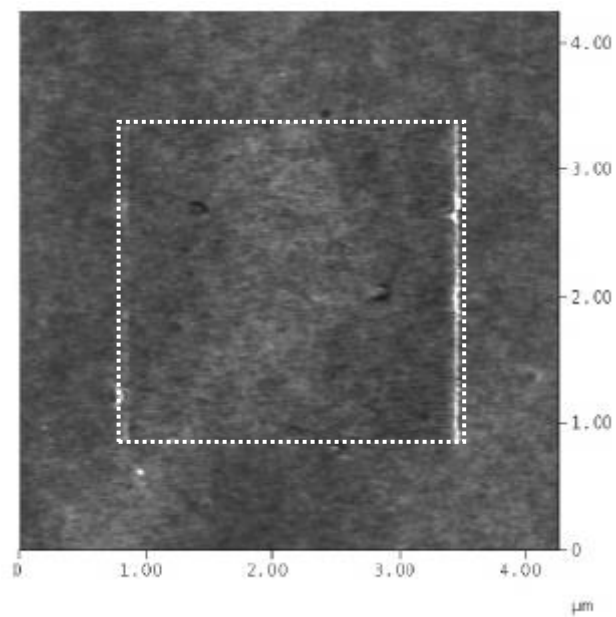


Figure 31. AFM image of a cross-linked polycarbonate film after scanning the central $2.5 \times 2.5 \mu\text{m}^2$ (dotted lines) 100 times with a load of 50 nN at a speed $\sim 25 \mu\text{m/s}$ (reprinted with permission from Ref. 190; Copyright (1993) Elsevier).

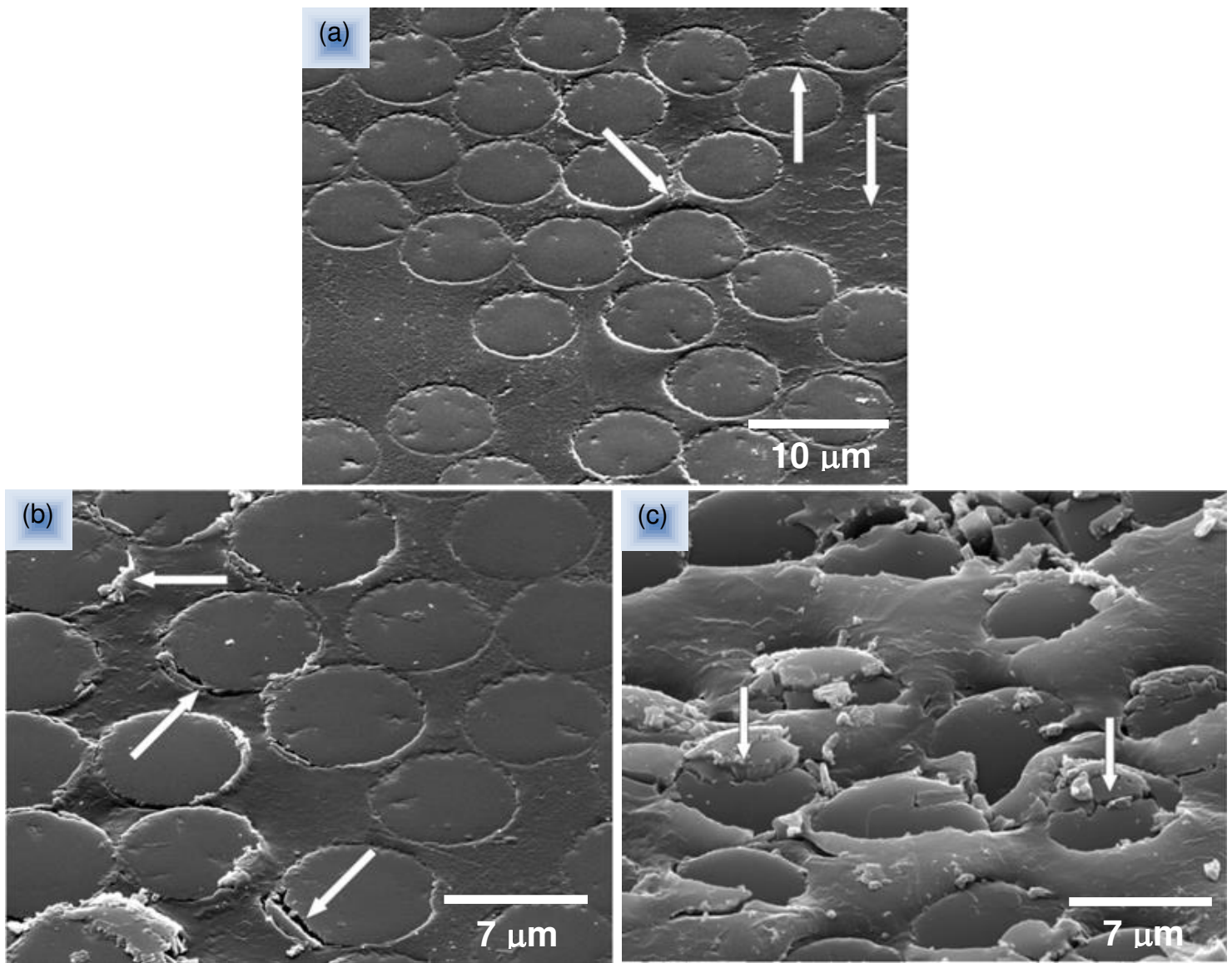


Figure 32. SEM micrographs of single pass scratched polymer/fiber composite with a diamond Rockwell indenter having a tip angle of 120° and a tip radius of $100\ \mu\text{m}$ at different applied loads: (a) 1 N - showing a transition between unscratched composite surface region (left side of figure) and scratched region (right side) having sheared features (indicated with arrows); (b) 2 N - showing the fiber/matrix delamination and fiber edge cracking (indicated with arrows) (scratched region is on the left side of figure); and (c) 3 N - showing severe cracking of fibers (pointed with arrows) and enhanced push-up of matrix between the fibers. The scratch direction

is from top to bottom in all the cases (reprinted with permission from Ref. 197; Copyright (2002) Springer).

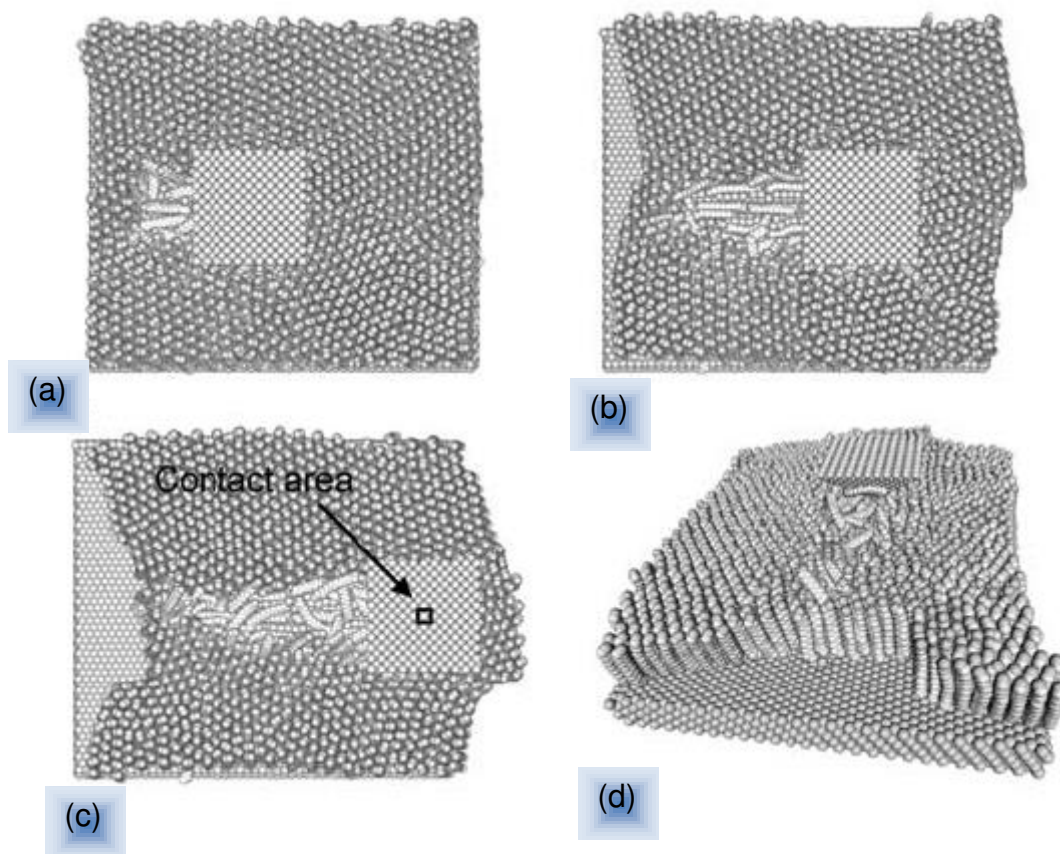


Figure 33. Snapshots of the scribed organothiol surface at the times t of (a) $t = 20$ ps, (b) $t = 40$ ps, (c) $t = 60$ ps; and (d) a perspective view. The tip-surface contact area is indicated by a rectangular mark (reprinted with permission from Ref. 215; Copyright (2005) Springer).

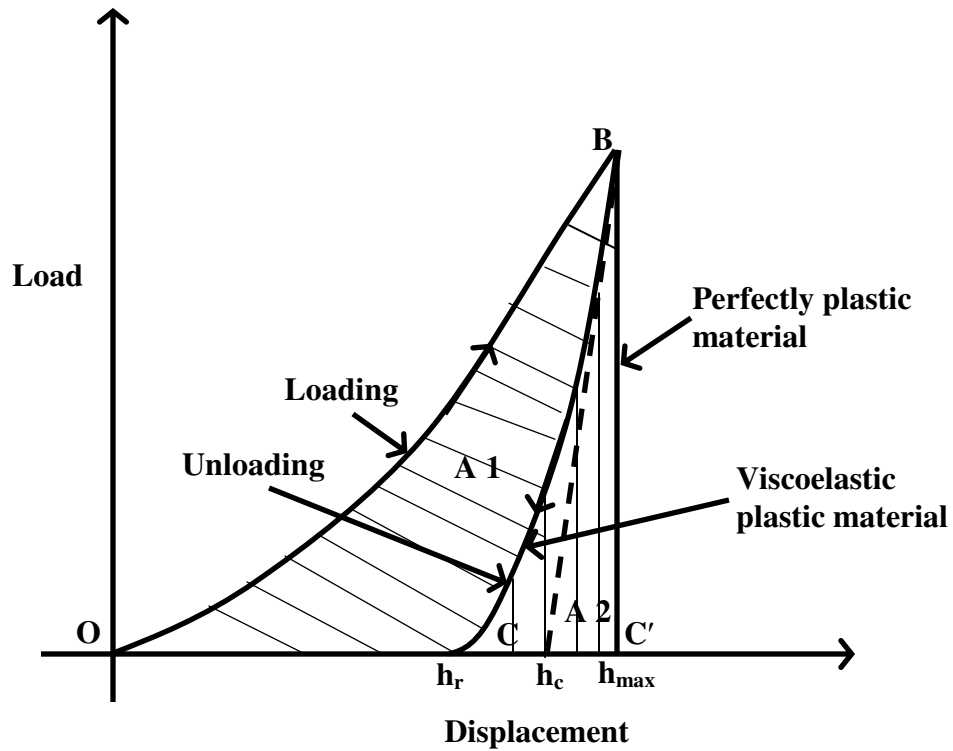


Figure 34. Schematic diagram of indentation load–displacement data for a viscoelastic-plastic material (loading, OB, and unloading, BC, segments). The plastic work done in the viscoelastic-plastic case is represented by the area A1 (OBC). The area A2 (CBC') corresponds to the elastic work recovered during the unloading segment (adapted from Ref. 261).

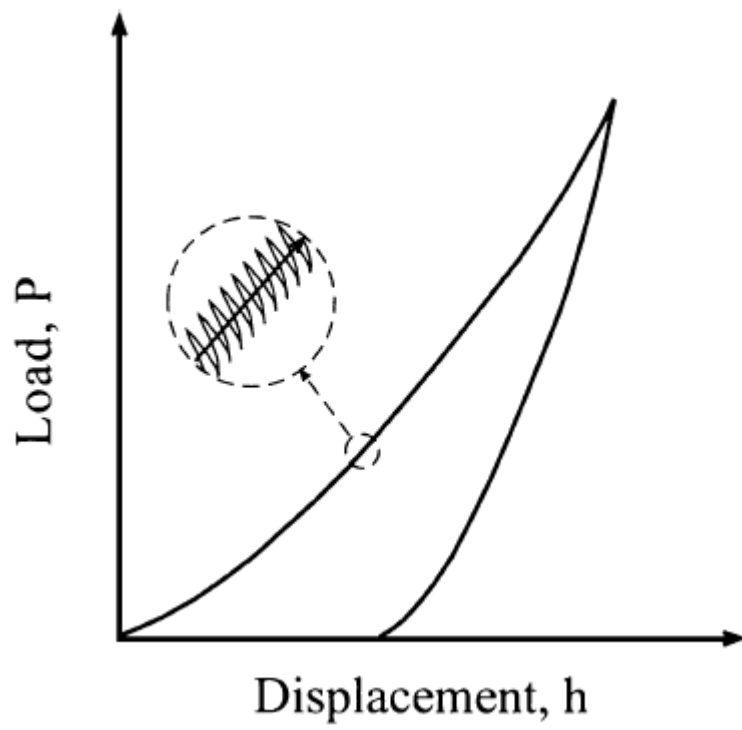


Figure 35. Schematic of the CSM loading cycle (reprinted with permission from Ref. 286; Copyright (2002) Elsevier).

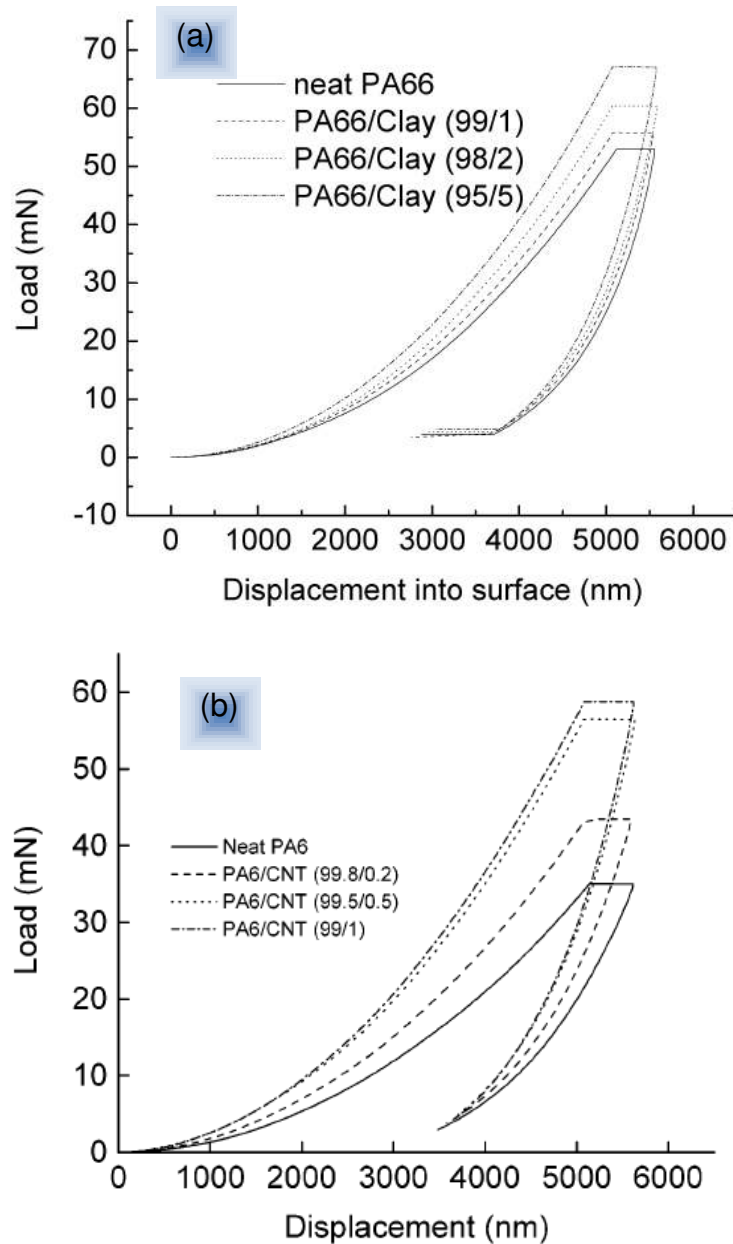


Figure 36. Examples indicating the polymer nanocomposites' resistance to indentation with increase in filler content: (a) nylon 66/clay nanocomposites (reprinted with permission from Ref. 296; Copyright (2004) Elsevier) and (b) nylon 6/CNT nanocomposites (reprinted with permission from Ref. 300; Copyright (2004) American Chemical Society).

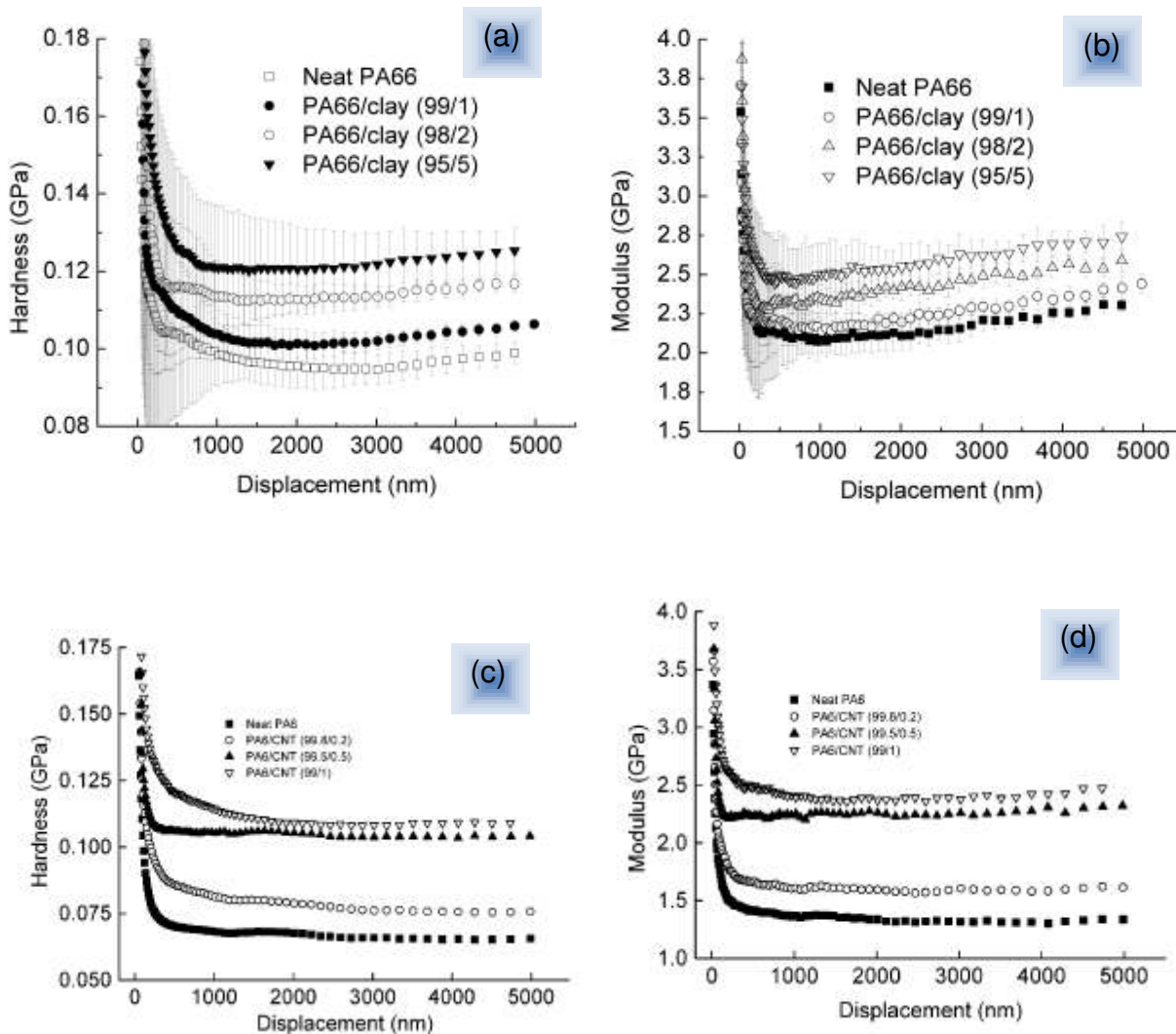


Figure 37. Examples showing the improvement in polymer nanocomposites' hardness and modulus (with increasing filler content) with regards to indentation depth: (a) nylon 66/clay nanocomposites (reprinted with permission from Ref. 296; Copyright (2004) Elsevier); and (b) nylon 6/CNT nanocomposites (reprinted with permission from Ref. 300; Copyright (2004) American Chemical Society).

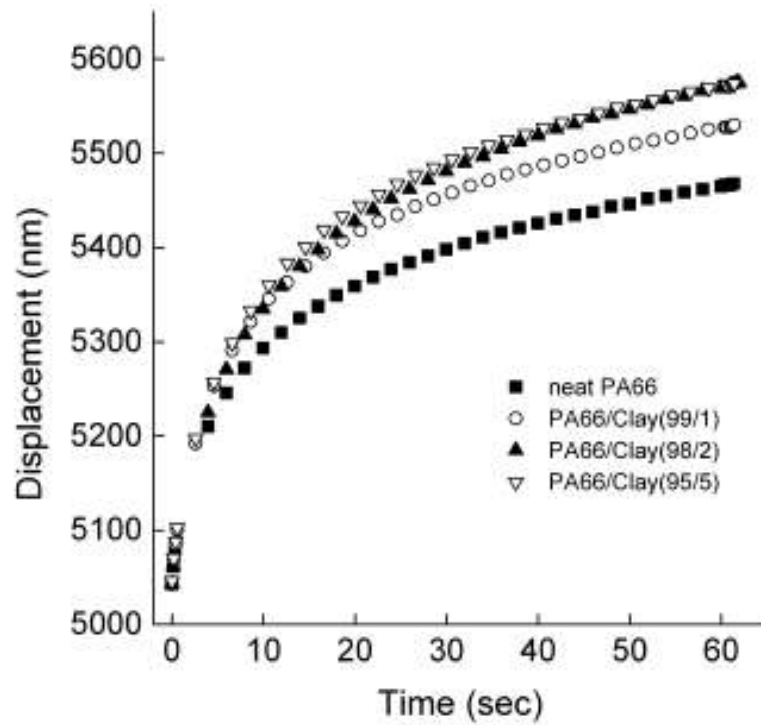


Figure 38. Plots of creep displacement versus holding time of polyamide 66 and its nanocomposites with different clay loadings (reprinted with permission from Ref. 296; Copyright (2004) Elsevier).

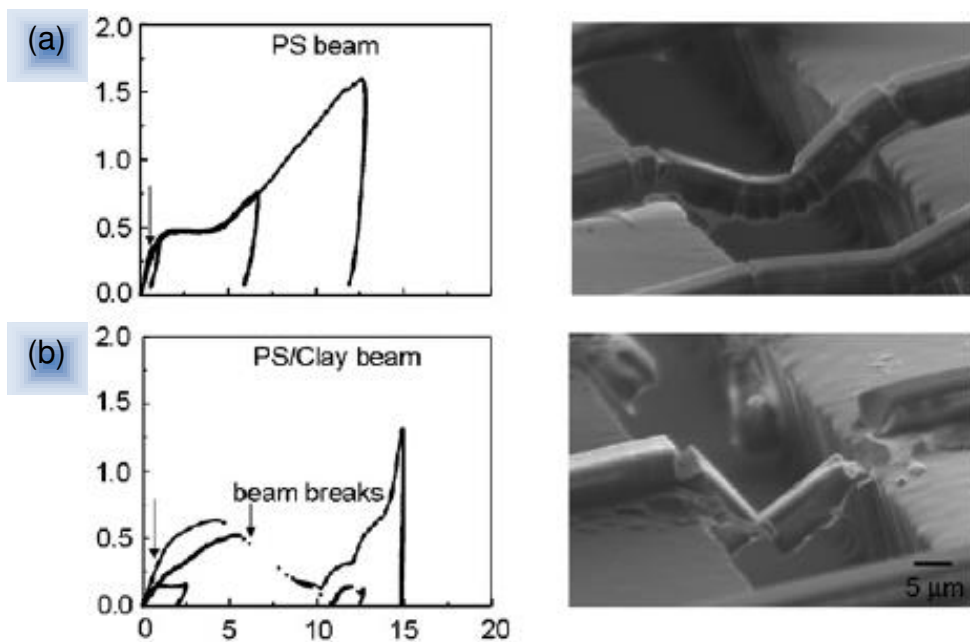
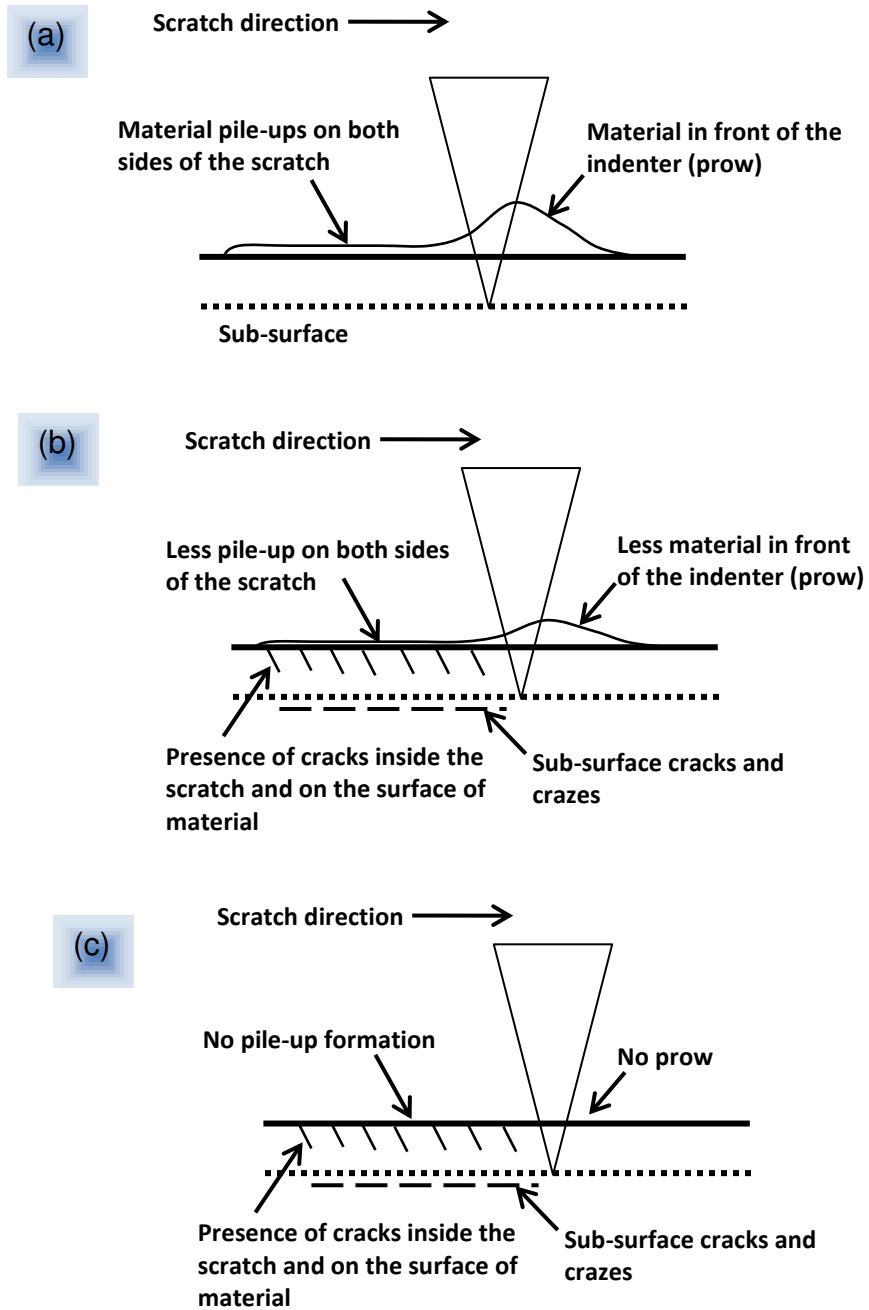


Figure 39. Normal load-displacement profiles at loads of 0.5, 1.5 and 3.0 mN for (a) neat polystyrene and (b) polystyrene/clay beams, where arrows indicate the onset of yield and breaking of the beams. After breaking the polystyrene/clay beam, the load continued to increase as a result of a pre-defined load imposed by the nanoindenter. Corresponding SEM micrographs of the beams are taken when subjected to a maximum load of 3.0 mN (reprinted with permission from Ref. 179; Copyright (2007) Elsevier).



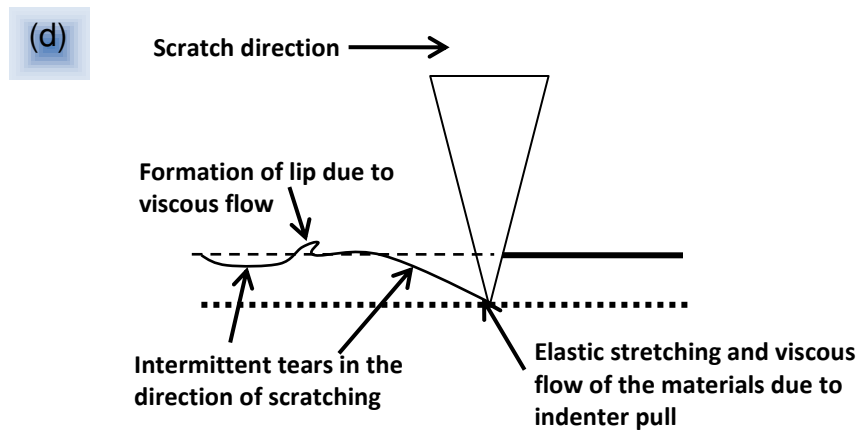


Figure 40. Schematic representations of the main polymeric material responses to scratching: (a) ductile response; (b) ductile and brittle response; (c) brittle response; and (d) elastomeric response (adapted from Ref. 313).

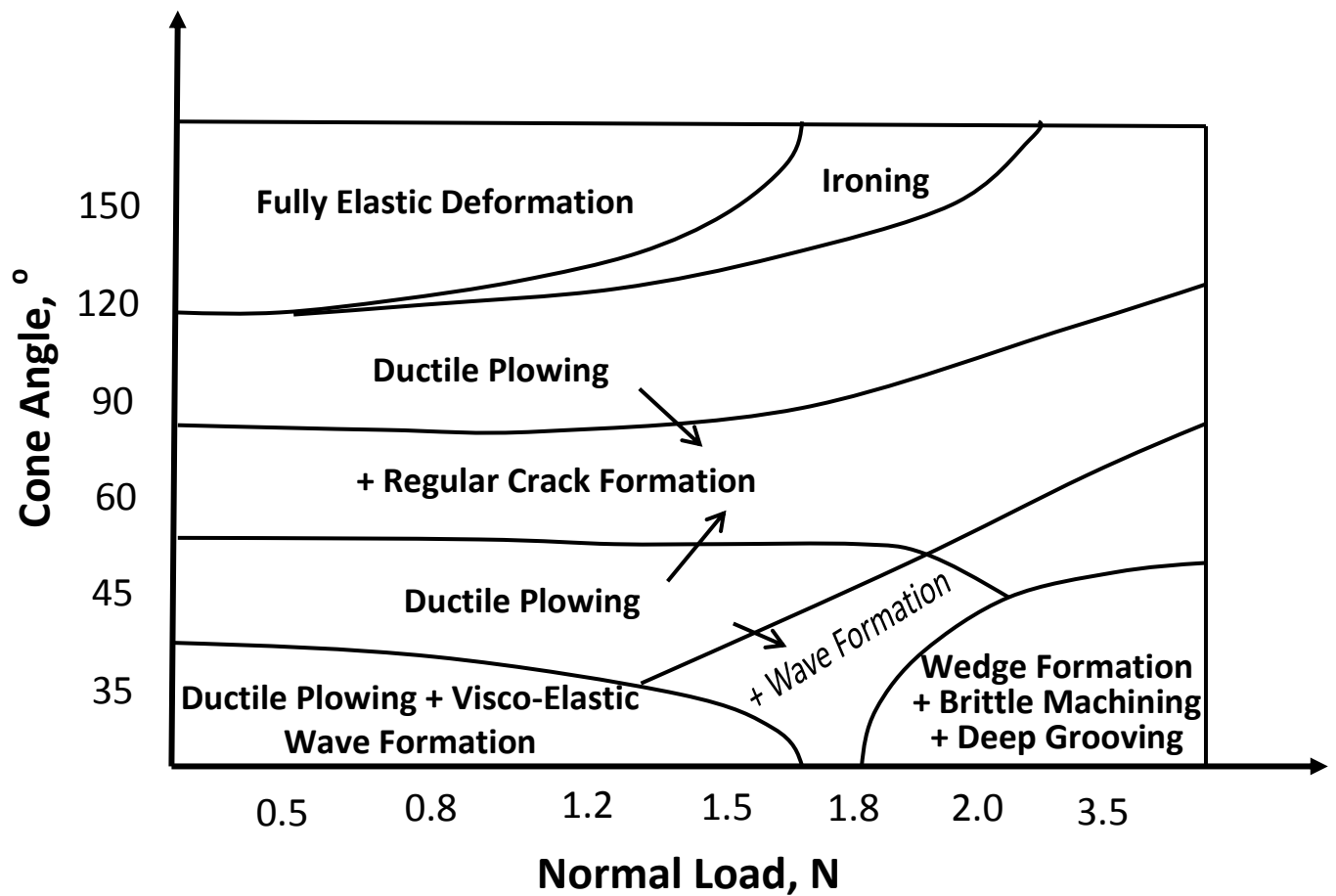


Figure 41. Scratch deformation map for polyethylene. Scratch tests were performed at room temperature for a range of cone angles and normal loads at a constant scratching velocity of 0.0026 mm/s (adapted from Ref. 326).

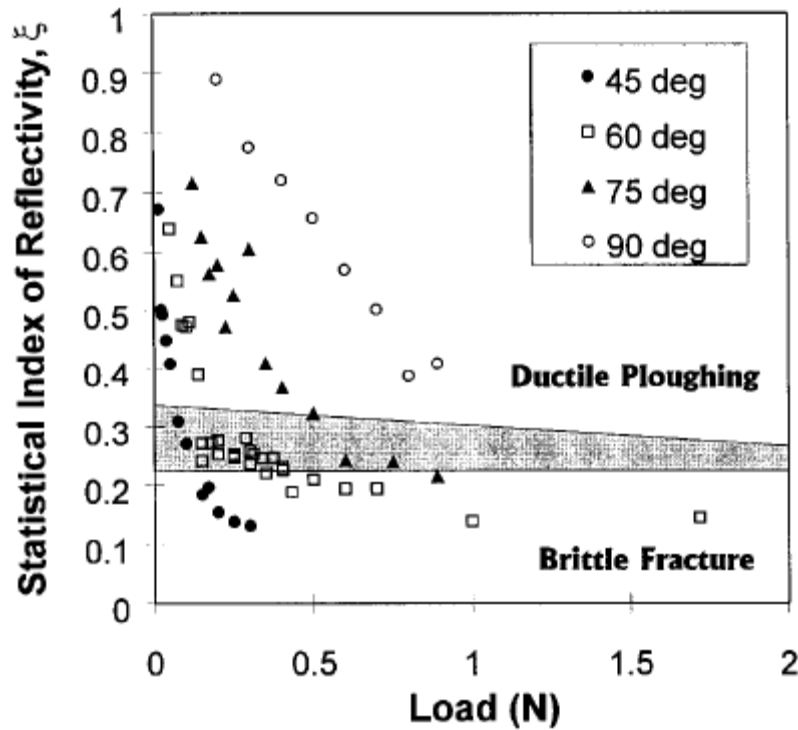


Figure 42. Statistical index of reflectivity, ξ , as a function of normal load for the scratches produced on PMMA using cones of various included angles. The map shows regions of brittle, ductile scratch deformations, and a transitional zone (shaded area). The areas were constructed from the SEM analyses of the scratch damaged regions. As evident, the reflectivity measurement may be used to determine the ductile to brittle transition. The parameter ξ varies between 0 and 1. For $\xi = 1$, 100% reflectivity for all the data analysed. For $\xi = 0$, the material surface does not reflect specularly any fraction of the laser beam (reprinted with permission from Ref. 332; Copyright (1997) Wiley InterScience).

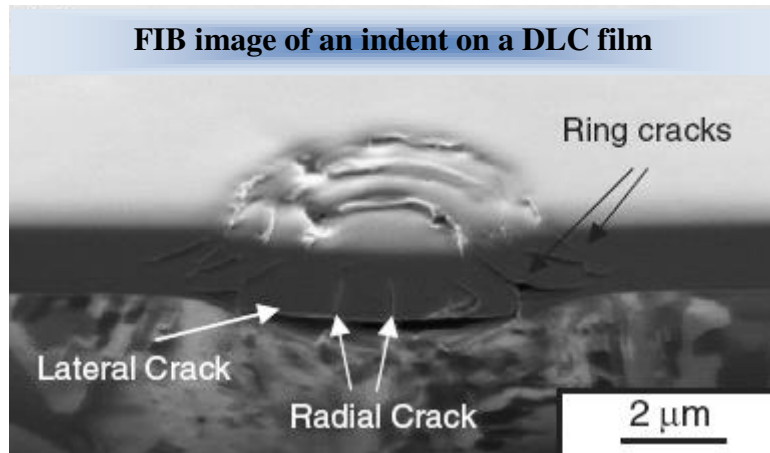


Figure 43. FIB micrograph showing the indented surface and cross-sectional views in a DLC coating and stainless steel substrate clearly revealing the nature of damage (reprinted with permission from Ref. 335; Copyright (2007) Elsevier).

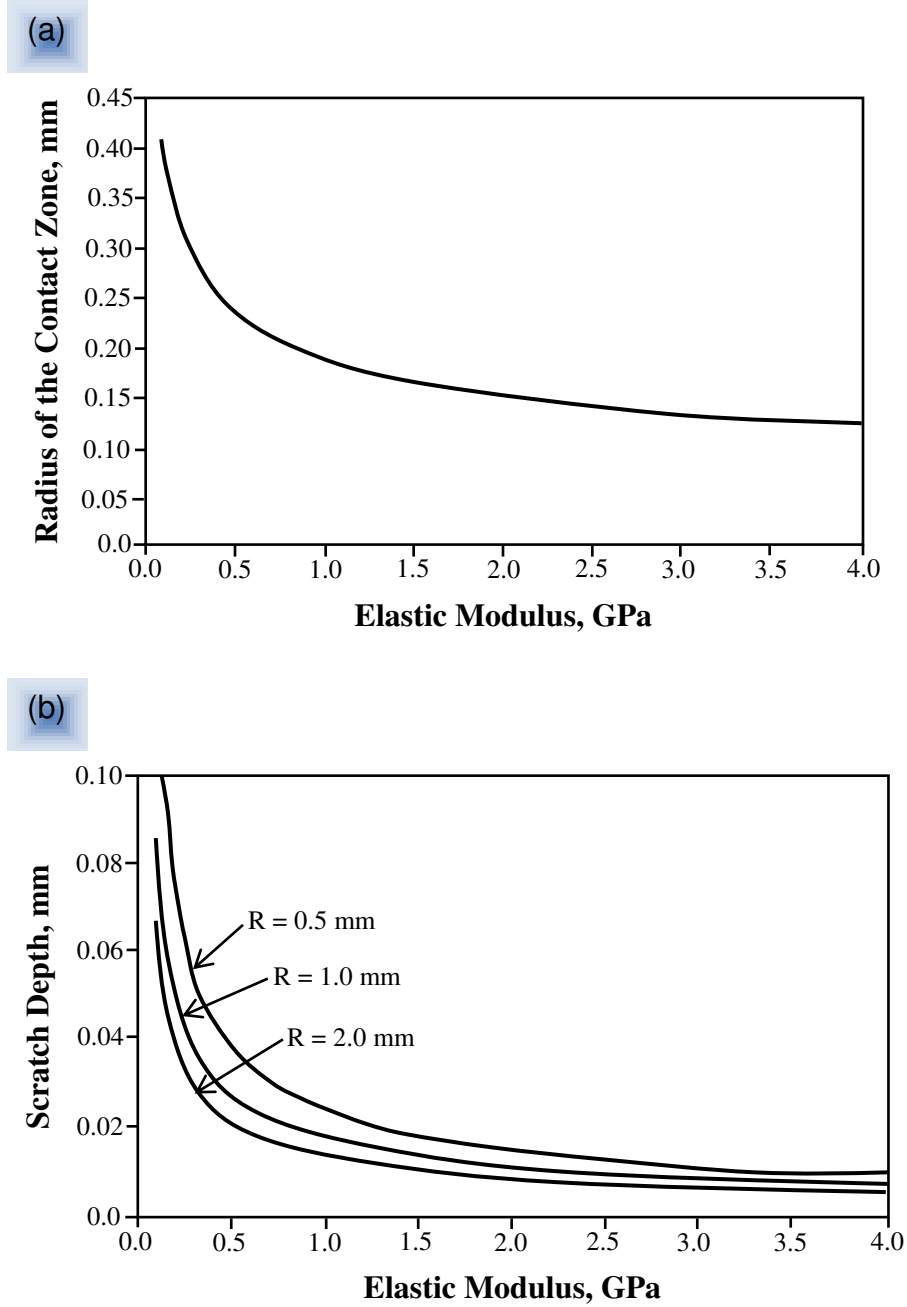
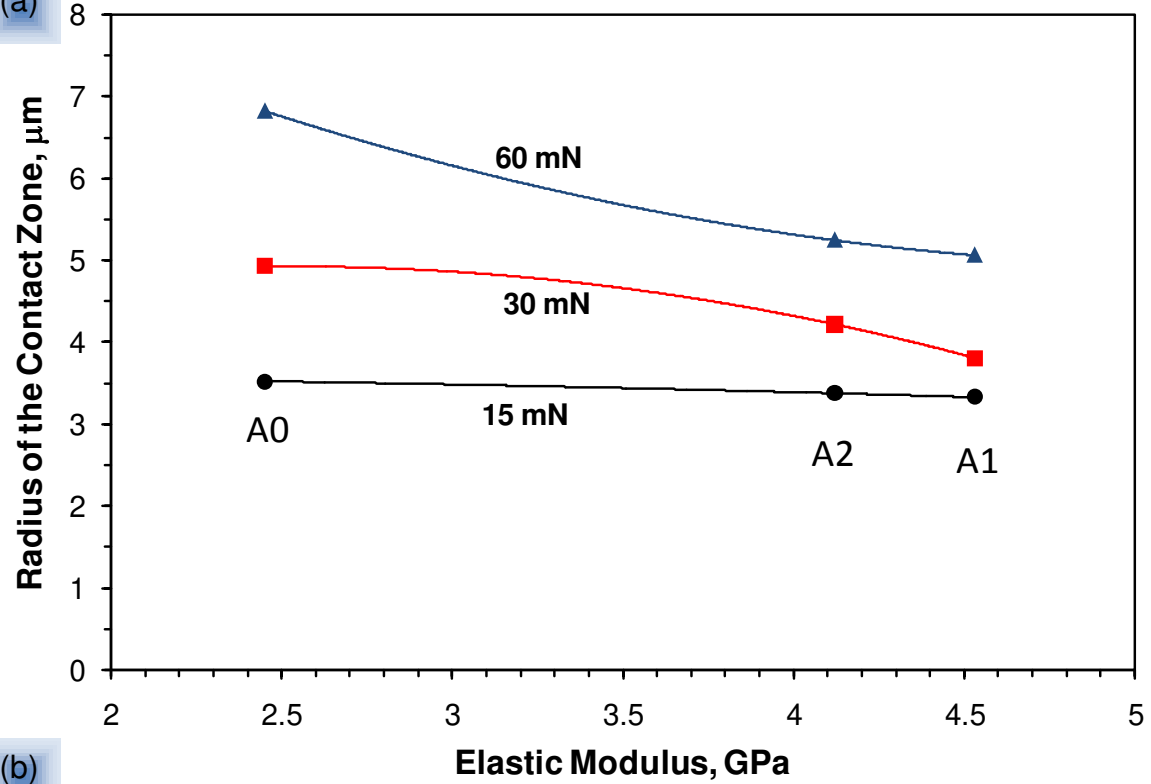
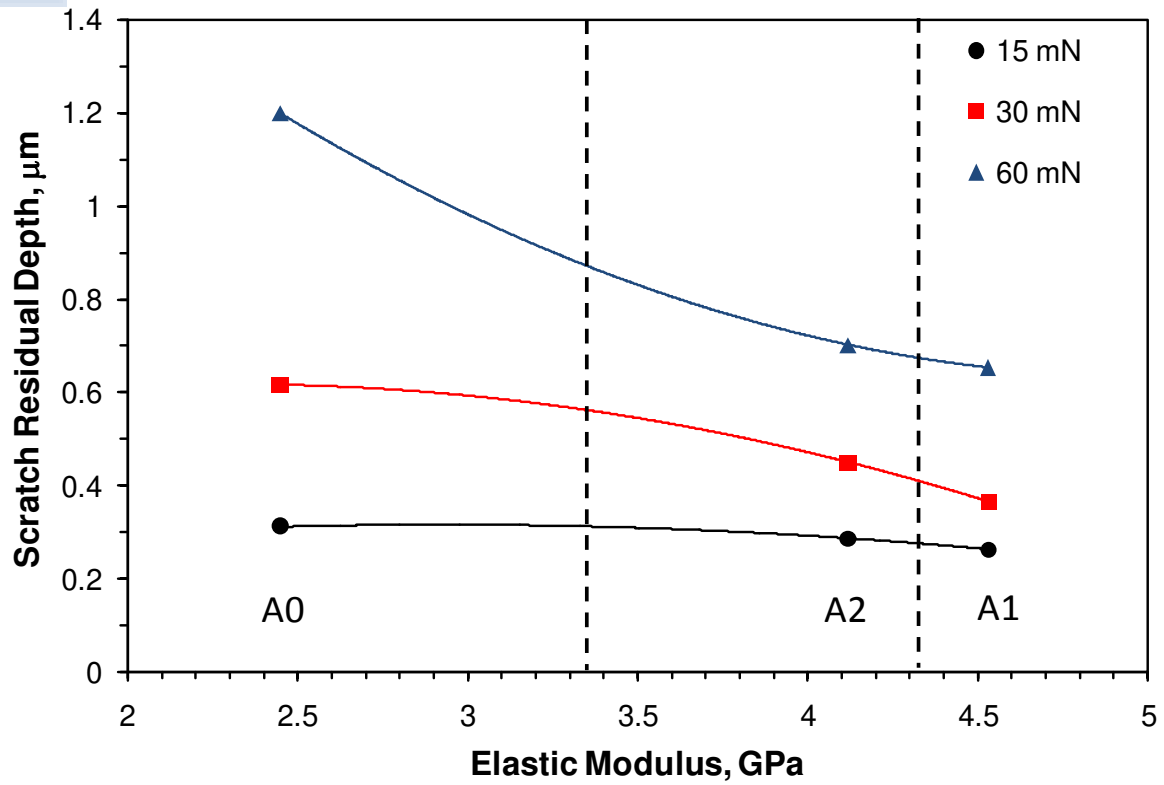


Figure 44. (a) The variation of contact zone size and (b) scratch depth with the elastic modulus of a specimen loaded under a spherical scratcher with a tip diameter(s) of (a) 1 mm and (b) 0.5, 1, and 2 mm at applied normal load of 30 N (adapted from Ref. 309).

(a)



(b)



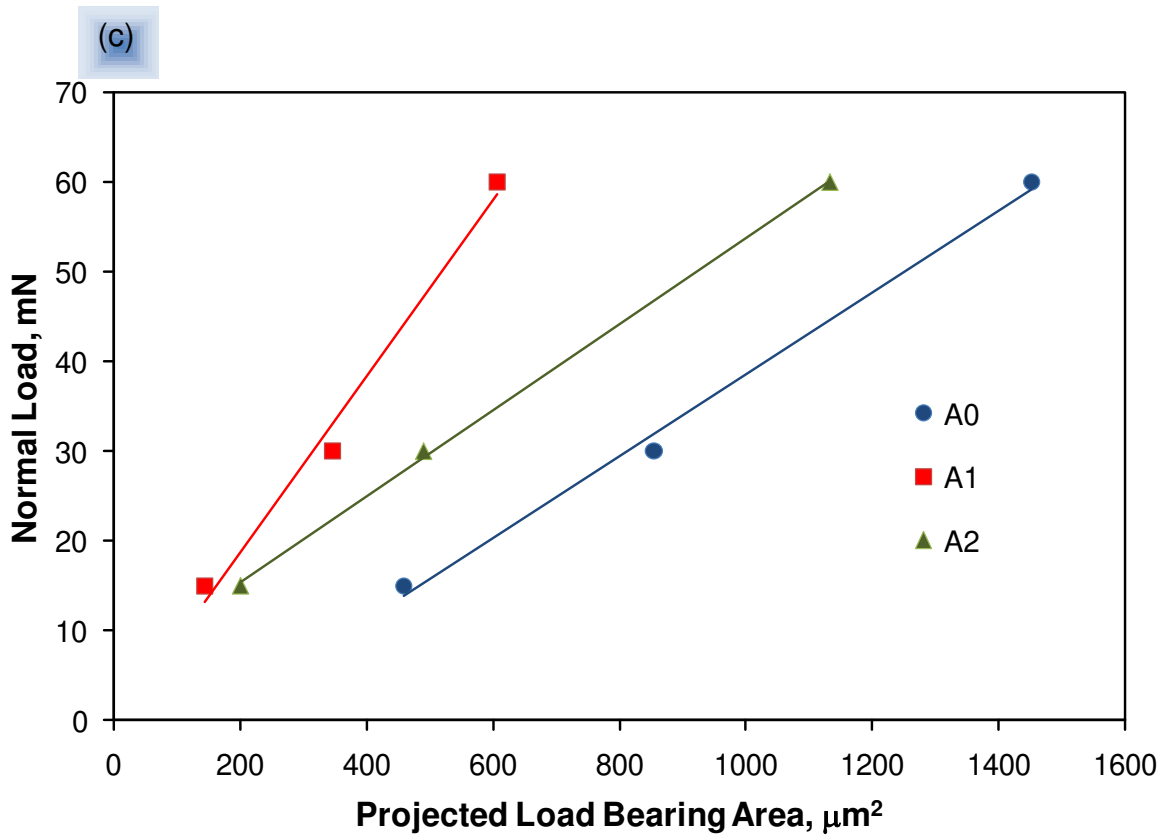


Figure 45. (a-b) The effect of Young's modulus of neat polyamide 6 (A0), polyamide 6 with well dispersed 10 wt % of organoclay (A1) and polyamide 6 with intercalated 10 wt % of organoclay (A2) on their (a) contact zone size calculated from equation 8 and (b) scratch residual depths when scratched with a 20 μm spherical indenter and at different loads; (c) plots of normal load *versus* projected load bearing area for the spherical indenter for A0, A1 and A2 (adapted from Ref. 345).

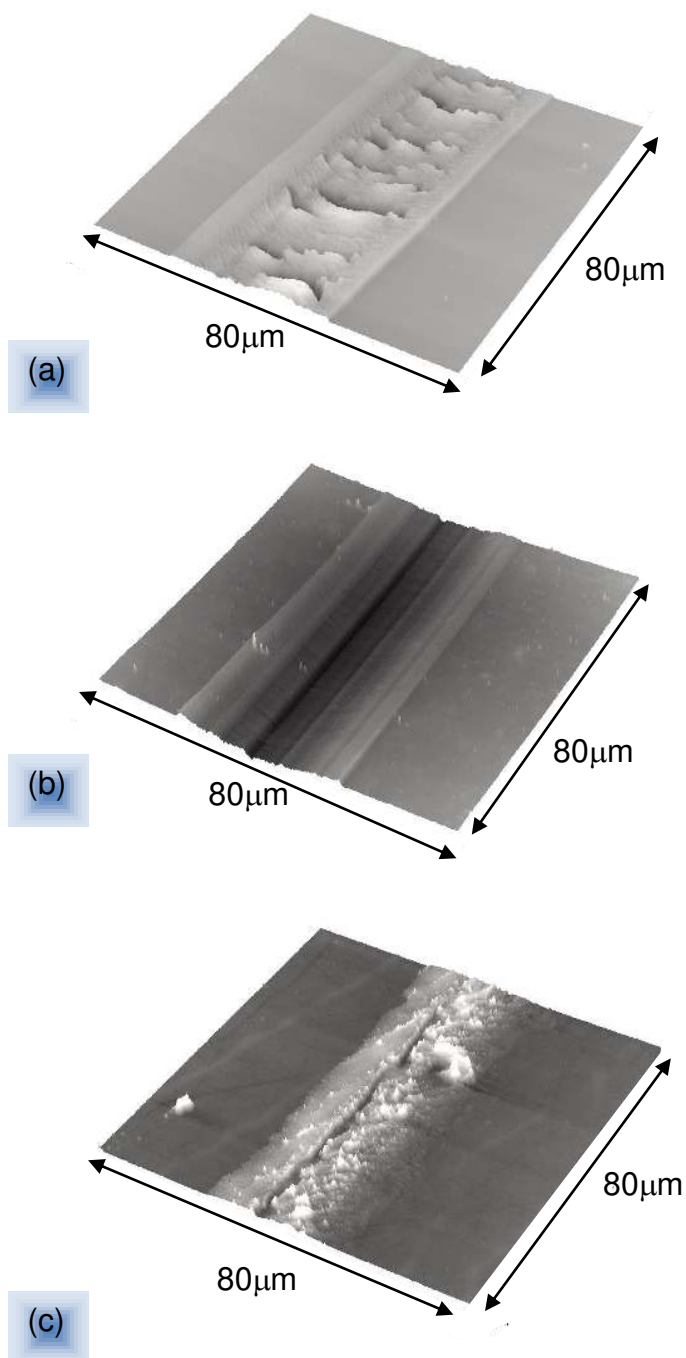


Figure 46. AFM topography showing scratch morphology of (a) neat gelatin film; (b) 1 wt % as-received nano-Al₂O₃ filled gelatin film; and (c) 1 wt % refined nano-Al₂O₃ filled gelatin (reprinted with permission from Ref. 346; Copyright (2002) Wiley InterScience).

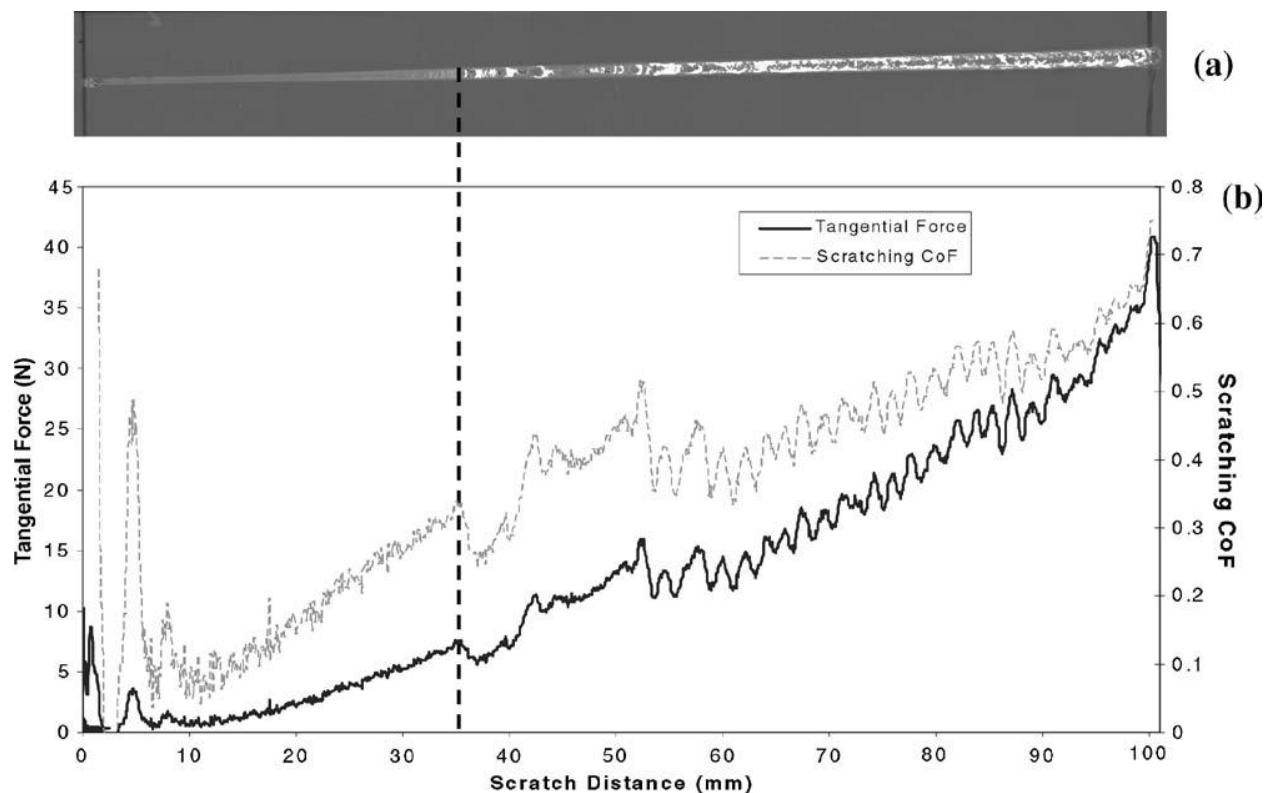


Figure 47. Scanned image of scratch track on a talc-filled copolymer sample and the corresponding friction force profile. Scratching conditions: constant scratch speed of 100 mm/s, linearly increasing normal load ranging from 5 to 50 N, scratch length ~100 mm, slider is a stainless steel spherical ball with a diameter of 1 mm, and tests were conducted at room temperature. The black dashed line marks the onset of stress whitening in (a) and the corresponding change in friction profile in (b) (reprinted with permission from Ref. 320; Copyright (2004) Springer).

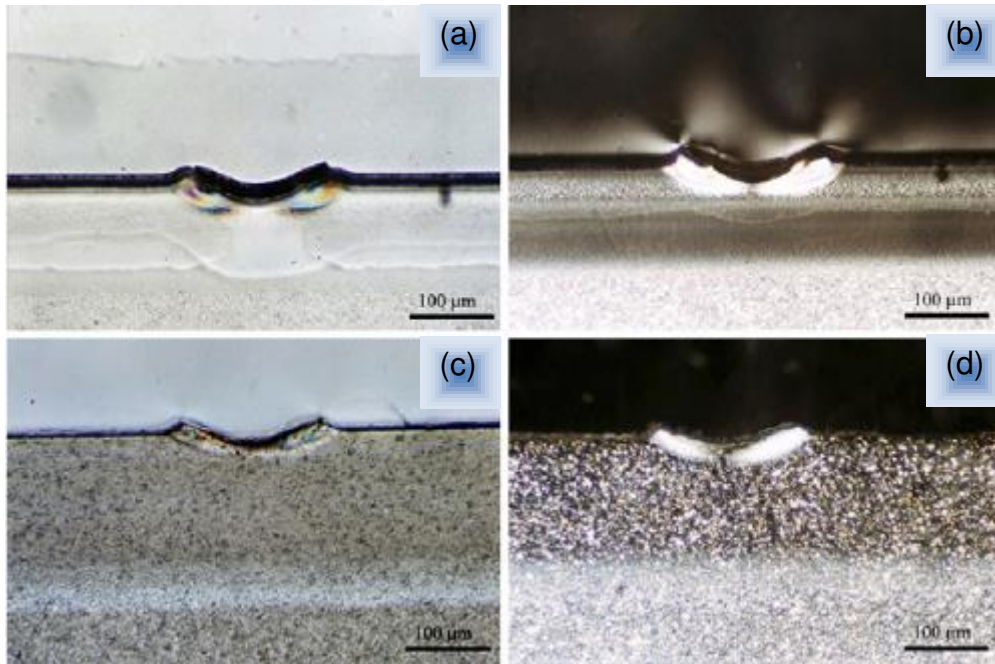


Figure 48. TOM micrographs of neat polypropylene (a-b) and polypropylene/calcium carbonate (90/10) nanocomposites (c-d) taken from the cross-sections of scratched specimens under (a, c) bright field and (b, d) cross-polarized light (reprinted with permission from Ref. 350; Copyright (2007) Elsevier).

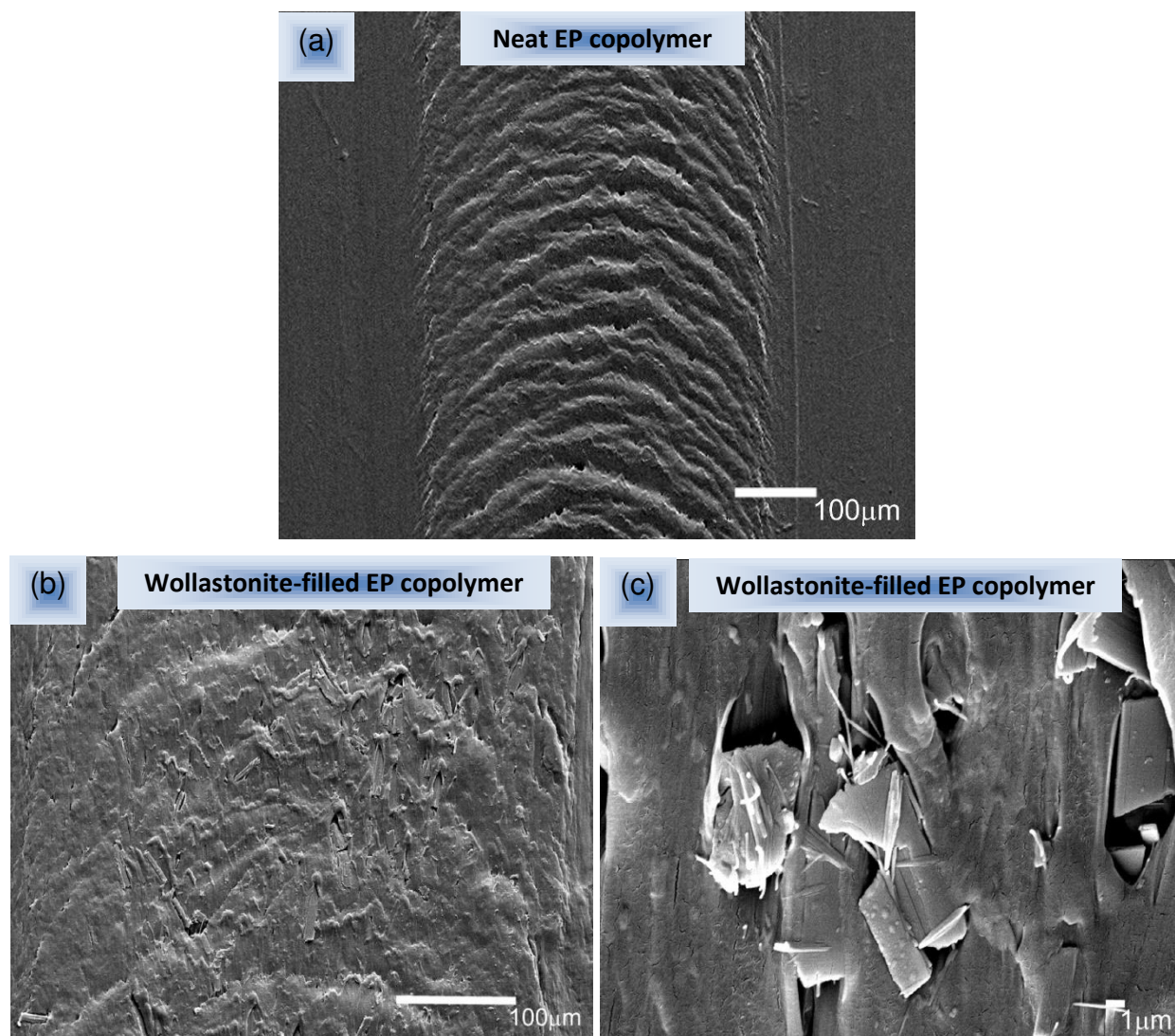


Figure 49. SEM micrographs for scratch damage regions of (a) neat ethylene-propylene copolymer; and (b-c) wollastonite-containing ethylene-propylene copolymer scratched at identical conditions (diamond conical indenter tip radius $\sim 5\text{ }\mu\text{m}$ with 120° included angle, load 7 N, and velocity $\sim 2\text{ mm/s}$) (reprinted with permission from Ref. 351; Copyright (2004) Wiley InterScience).

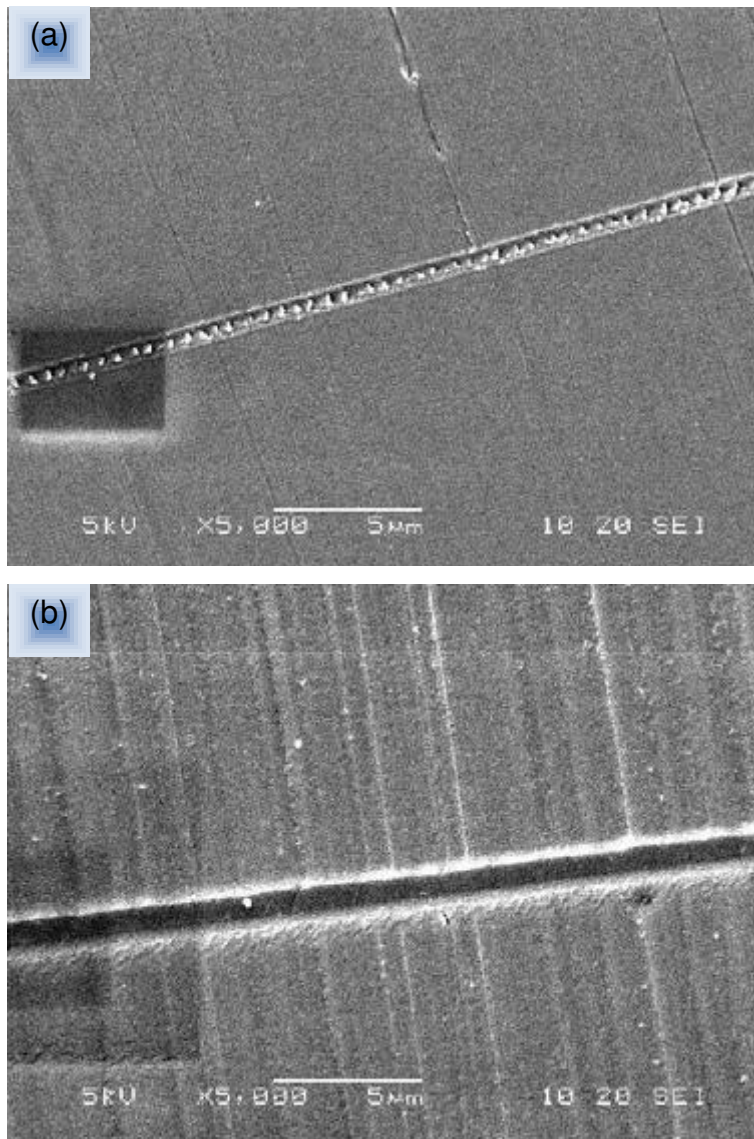


Figure 50. SEM micrographs of scratched (a) PMMA and (b) PC surfaces using an indenter with radius ~ 80 nm. A constant load of $100\ \mu\text{N}$ and constant scratch rate of $1\ \mu\text{m/s}$ were applied (reprinted with permission from Ref. 355; Copyright (2004) Elsevier).

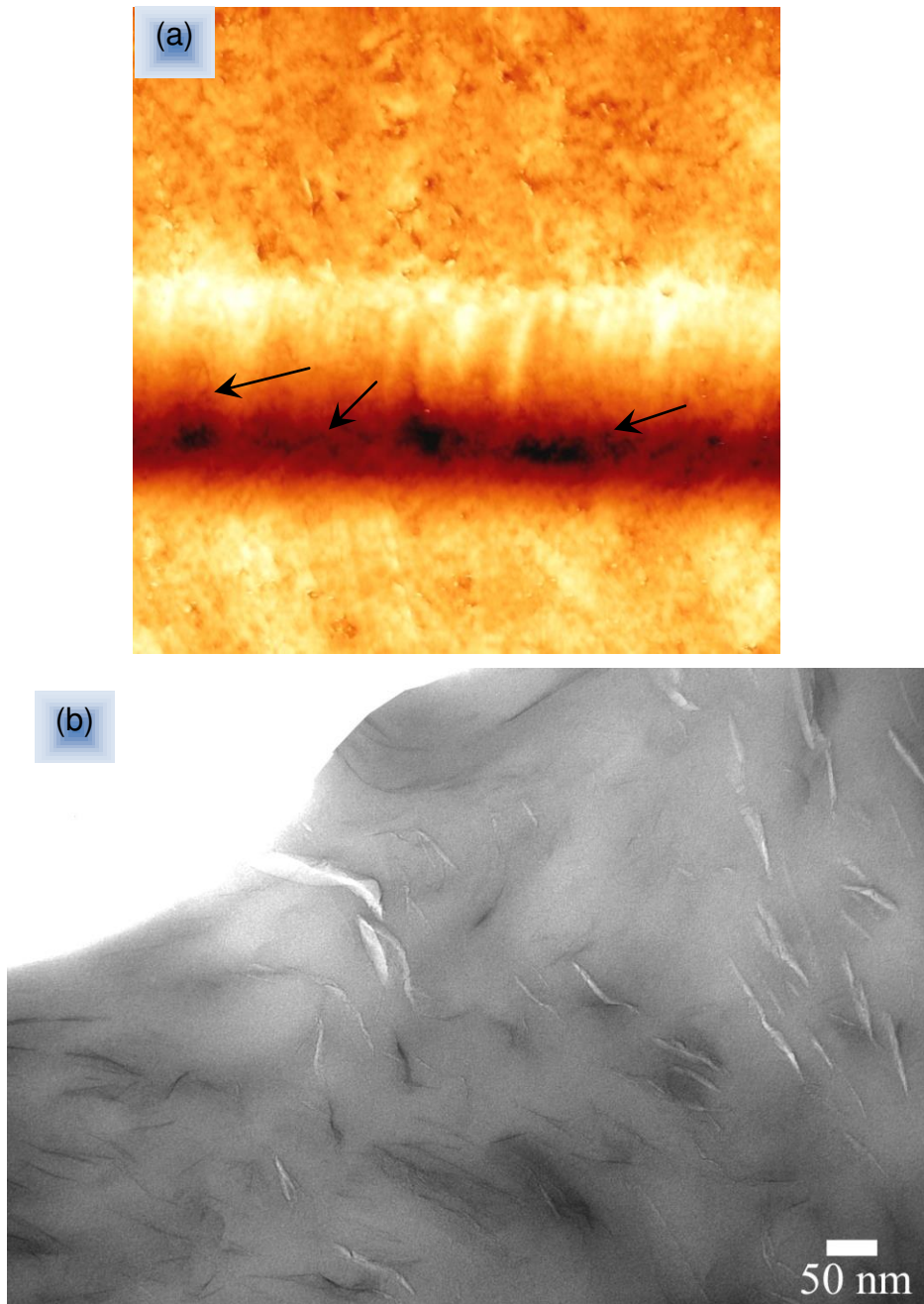


Figure 51. (a) 2-D AFM micrograph at a field-of-view of $20\ \mu\text{m} \times 20\ \mu\text{m}$ showing the presence of brittle cracks (pointed with arrows) after nanoscratching the nylon/clay nanocomposite; and (b) TEM micrograph showing the subsurface damage beneath the scratch track. Nanocracks are formed, which are associated with delaminations between the clay layers (reprinted with permission from Ref. 361; Copyright (2007) Elsevier).

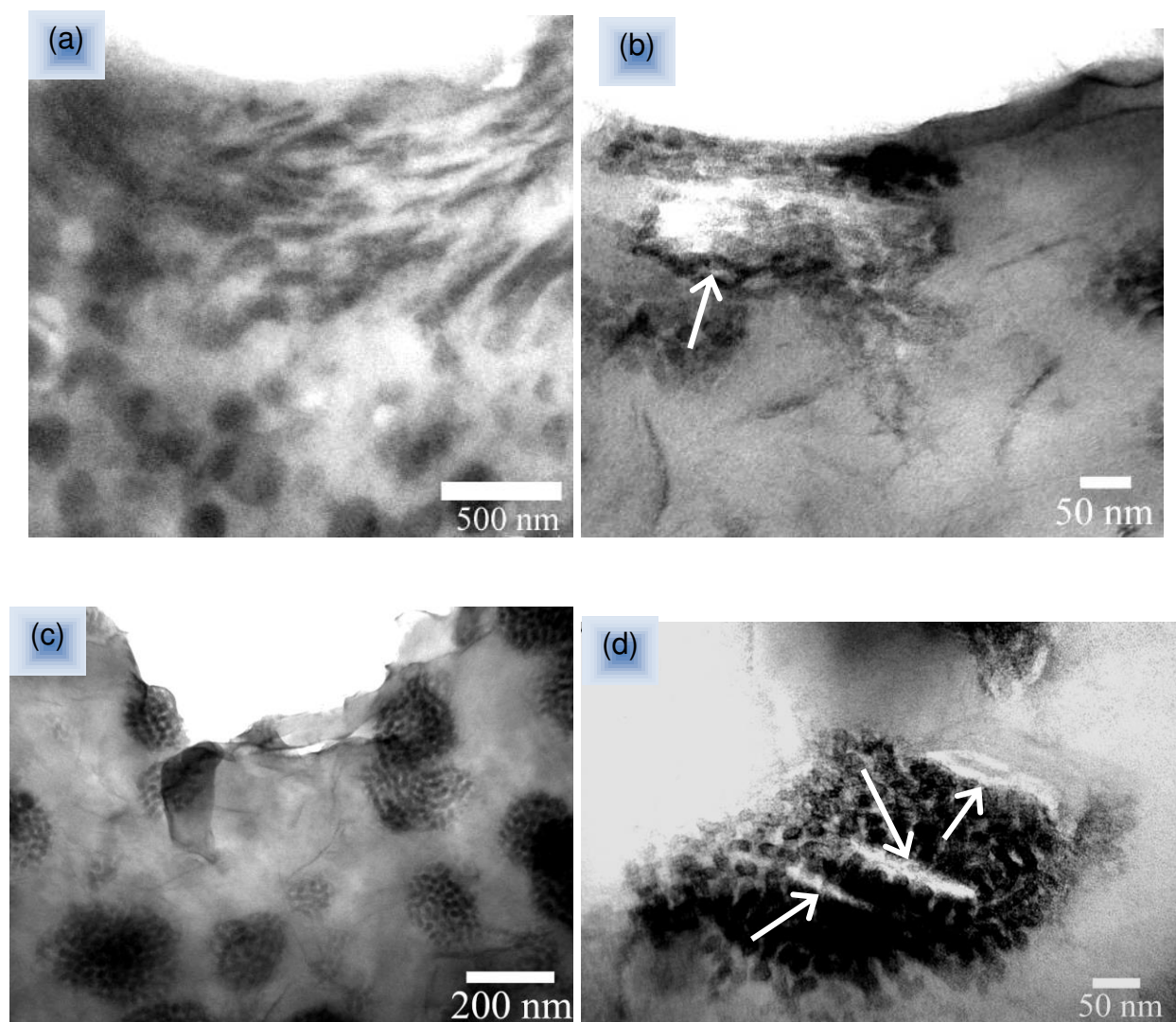


Figure 52. TEM micrographs at two magnifications of subsurface damage beneath the scratch track tested at an applied load of 1 mN and a scratch velocity of 1 $\mu\text{m/s}$ in (a-b) S1 and (c-d) S2. Arrow in (b) indicates cavitation of an SEBS-g-MA particle; while debonding of intercalated clay in matrix, particle-matrix interface and within the particles are indicated by arrows in (d). The scratch tracks extend into the paper from the top in (a) and (c) (reprinted with permission from Ref. 361; Copyright (2007) Elsevier).

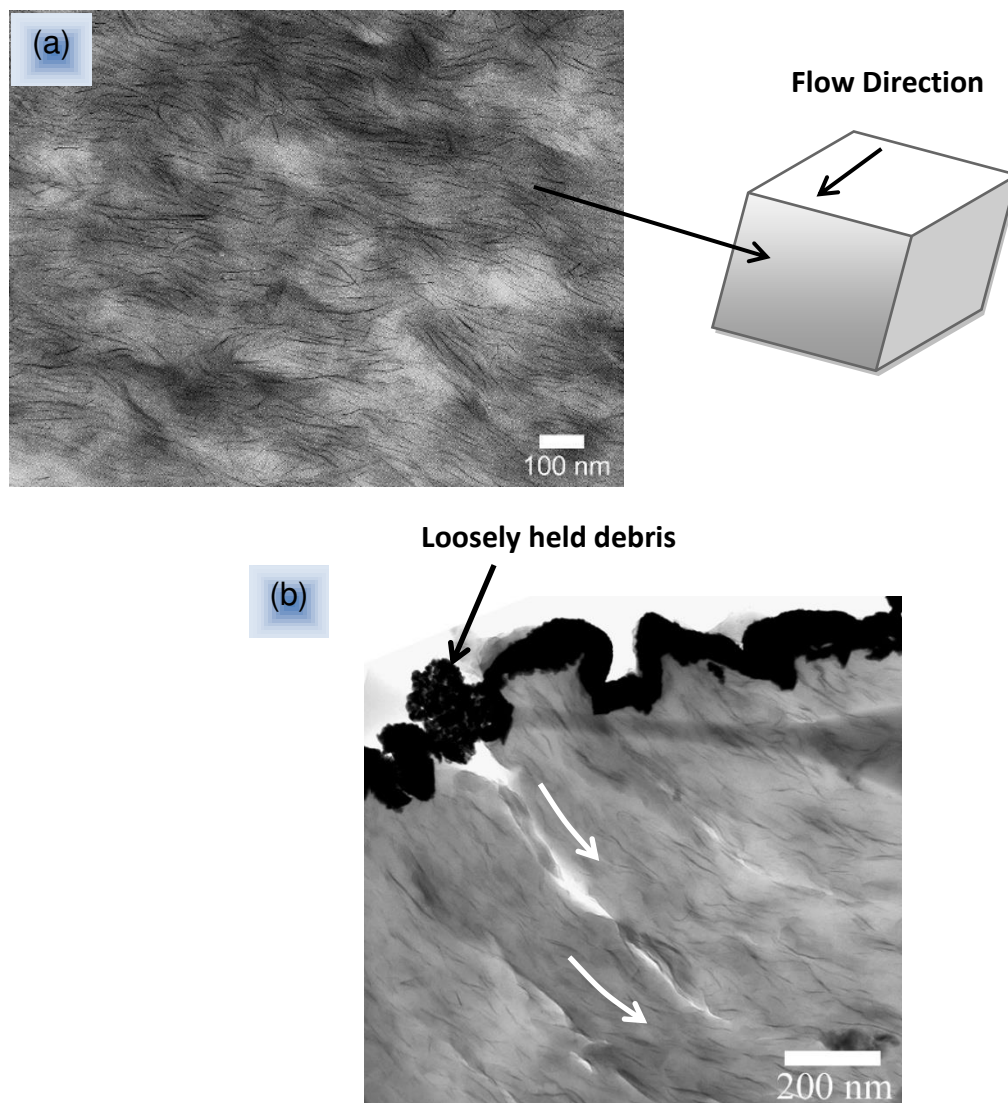


Figure 53. (a) TEM micrograph showing the original silicate layer orientation in the sample; and (b) micrograph taken after the scratch test showing subsurface damage beneath scratch track. White arrows points to the rotation of clay layers under the applied stress field. Scratch test conditions: normal load ~ 60 mN, scratch velocity ~ 5 $\mu\text{m/s}$, spherical indenter and parallel to flow direction (reprinted with permission from Ref. 345; Copyright (2008) Institute of Physics).